Metal Complexes Responding to External Stimuli by Using π-Radical Ligands with Photo-Sensitive Anthracene Derivatives

（光感応部位としてアントラセン骨格を有するπラジカル配位子を用いた外場応答性金属錯体）

理学研究科

物質分子系専攻

平成 27 年度

片山　晃一

(Koichi Katayama)

Abstract

In this thesis, the author focuses on π-spin systems consisting of the bistable complexes and a π-radical ligand containing anthracene as the photo-sensitive moiety. This thesis is arranged into four chapters. Chapter 1 describes the history and expectations of bistable compounds, and the aim of this study.

In Chapter 2, a π-radical ligand with a photo-excited high-spin quartet state (S = 3/2), $\mathbf{L^1}$, is constructed from 2,2'-bipyridine as a coordination moiety, anthracene as a photo-sensitive moiety, and a verdazyl radical. An iron(II) complex of $\mathbf{L^1}$ (**1**) was synthesized as a candidate for a new strategy for spin crossover compounds exhibiting light-induced excited spin state trapping (LIESST), which is via the photo-excited high-spin state of the π-conjugated aromatic system. Control compounds, ligand $\mathbf{L^2}$ and its iron complex (**2**), in which the verdazyl radical moiety in $\mathbf{L^1}$ was removed, were also synthesized. The photo-excited quartet state of the π-radical ligand $\mathbf{L^1}$ was confirmed by the time-resolved ESR technique. Temperature dependence of the magnetic behaviors of **1** and **2** were investigated from 5 K to 350 K, showing spin-crossover transition at T_c = 222 K and at T_c = 162 K for complexes **1** and **2**, respectively. The transition enthalpies and entropies were determined to be ΔH = 8.09 kJ mol^{-1} and ΔS = 36.4 J K^{-1} mol^{-1} for **1** and to be ΔH = 22.39 kJ mol^{-1} and ΔS = 138 J K^{-1} mol^{-1} for **2**. LIESST phenomena were also observed below ca. 50 K for both complexes.

Chapters 3 and 4 describe design of a fluorescence switching system by using valence tautomeric cobalt complexes with dioxolene ligand containing an anthracene moiety and BODIPY as a fluorescence moiety. In Chapter 3, as building blocks for the fluorescence switching system by valence tautomerism, the anthracene-functionalized cobalt complexes **3**–**6** were synthesized by the combination of 9-(3,4-dihydroxyphenyl)anthracene ($\mathbf{H_2L^3}$) and tris-(2-pyridylmethyl)amine (TPA) or its derivatives (Me$_n$TPA, n = 1, 2, 3) Characterization of

complexes **3**–**6** was performed by UV-vis absorption, IR, ^{1}H NMR, and magnetic susceptibility measurements. In the solid state, the variable-temperature magnetic susceptibility data showed that complex **3** is low-spin cobalt(III) catecholate (Co^{III}(LS)-Cat), while complex **6** is high-spin cobalt(II) semiquinonate (Co^{II}(HS)-SQ) in the range 4.5–400 K. The susceptibility data of complexes **4** and **5** suggested valence tautomerism between the Co^{III}(LS)-Cat and Co^{II}(HS)-SQ forms. Light-induced valence tautomerism was observed in complexes **4** and **5** at 5 K by photo-irradiation. In solution, the temperature dependence of ^{1}H NMR spectra of **3** and **4** showed an equilibrium between their geometrical isomers.

In Chapter 4, $\mathbf{H_2L^4}$ composed of a catechol and an anthracene-BODIPY unit was used for the synthesis of cobalt complexes **7**–**9**. The characterization of complexes **7**–**9** was carried out by UV-vis absorption, IR, and ^{1}H NMR measurements. The spectroscopic data indicate that the introduction of BODIPY moiety would not affect the spin states of the cobalt center at room temperature. To investigate the effect of the spin states of the cobalt center, fluorescence spectra of $\mathbf{H_2L^4}$, complexes **7**, and **9**, and the control compounds, $\mathbf{H_2L^3}$ and complex **3** were measured in CH_3CN solution at room temperature. Compared with the fluorescence behavior of $\mathbf{H_2L^4}$, complexes **7** and **9** showed the decrease of the emission, and the clear difference of the emission between **7** and **9** was observed. Complex **7** shows the lowest fluorescence intensity due to the enhanced non-radiative processes, because the catecholate form strongly coordinate the cobalt center compared with semiquinonate form. As the possibility of the fluorescence quenching mechanism of BODIPY, the electrochemical data are indicative of ET process.

List of Compounds

Abbreviation	Compounds
L^1	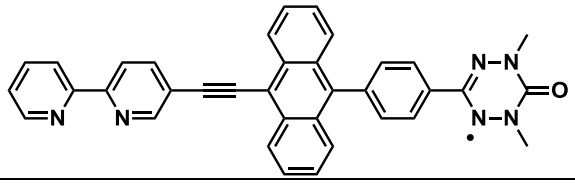
L^2	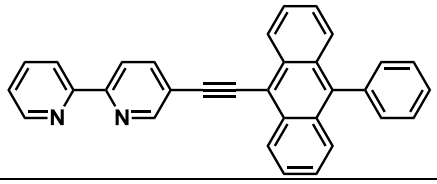
1	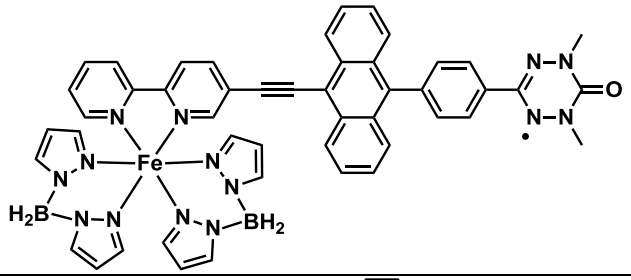
2	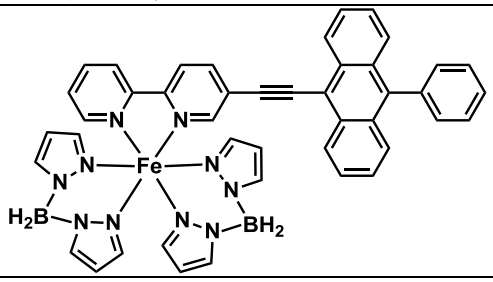

H_2L^3	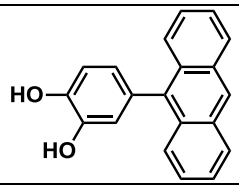			
H_2L^4	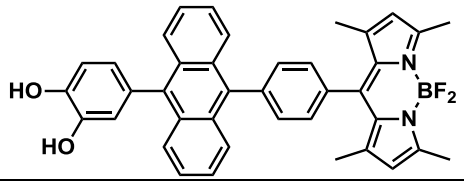			
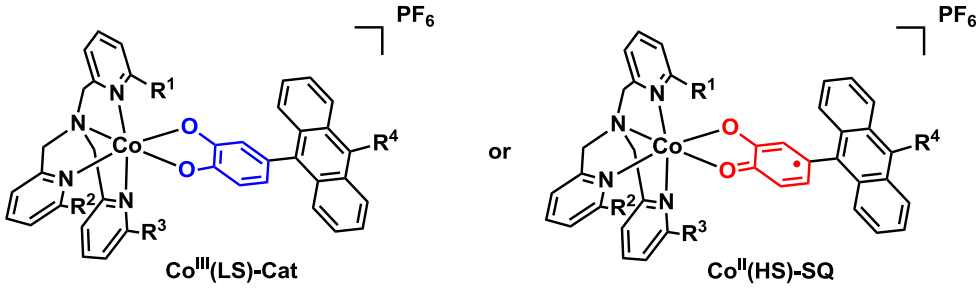				
	R^1	R^2	R^3	R^4
3	H	H	H	H
4	H	H	Me	H
5	H	Me	Me	H
6	Me	Me	Me	H
7	H	H	H	BODIPY
8	H	Me	Me	BODIPY
9	Me	Me	Me	BODIPY

Table of Contents

Chapter 1

General Introduction

1-1. Control of spin states by external stimuli

Spin manipulation by external stimuli is very important in the field of molecular magnetism, because of the potential for future applications in molecular electronics and spintronics.[1] Some metal complexes showing molecular bistability such as spin-crossover (SCO) complexes[2] and valence tautomeric (VT) complexes[3] are candidates for not only these applications but also high-density memory, displays, switching systems, and sensors because of showing a reversible change of color and other physicochemical properties.[4] Light is an especially powerful tool for controlling molecular magnetism because of short response times, low power dissipation and high selectivity. In SCO complexes and VT complexes, the trapping of photo-excited spin states at low temperature are known as LIESST (Light-induced excited spin state trapping) and LIVT (Light-induced valence tautomerism), respectively.[5] On the other hand, Teki and coworkers have studied spin alignment and spin dynamics of π-conjugated organic spin systems in the photo-excited spin states by time-resolved ESR spectroscopy.[6] The switching of magnetic interactions by photo-irradiation was reported. In this context, the author believes a new spin system composed of the bistable complexes and the π-conjugated spin system should contribute to the development of highly functional materials. In the following sections, the SCO complexes, the VT complexes, and the π-radical spin systems relevant to this study are described in detail.

1-2. Spin-crossover (SCO) complexes

SCO phenomenon is a reversible switching process between the low-spin (LS) and high-spin (HS) states by external triggers such as temperature, pressure, or light. The switching of spin

states is accompanied by changes in magnetism, color, and molecular structure. Cambi and Szego observed for the first time the spin transition of iron(III) complexes in 1931.[7] In 1964, the first iron(II) SCO systems were observed by Baker and Bobnich (Figure 1-1).[8] The properties at the molecular level have been described by ligand field theory (Scheme 1-1). The HS or LS spin states of metal complexes depend on the ligand field strength and the spin pairing energy. Some of iron(III) SCO complexes show the spin transition between the intermediate-spin (IS) and HS states.[9] The number of iron SCO compounds and detailed physical studies increased rapidly during the 1970s and the reviews were published.[2,10]

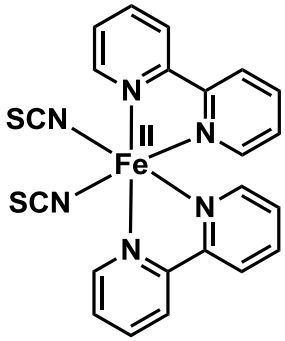

Figure 1-1. Molecular structure of the first iron(II) spin crossover complex

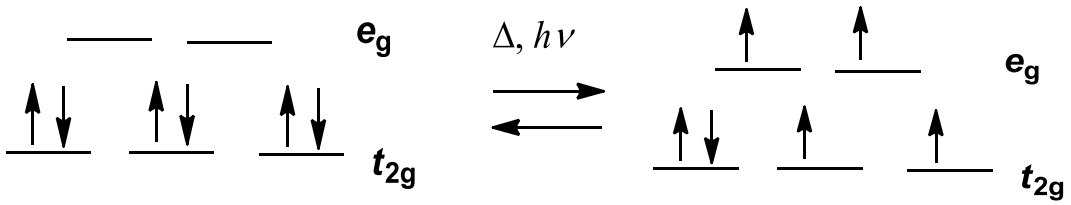

Scheme 1-1. Schematic illustration of spin transition for d^6 metal complexes.

Most iron(II) SCO complexes have an $[FeN_6]$ core. For example, $[Fe\mathbf{L}_2(NCS)_2]$ series (**L**: bpy = 2,2'-bipyridine, phen = 1,10-phenanthroline, btz = 2,2'-bi-4,5-dihydrothiazine, dpp = dipyrido[3,2-a:2'3'-c]phenazine)[8] and $[Fe(Rtz)_6](BF_4)_2$ series (R = Me, Et, Pr, iPr, tz = tetrazole)[2(a)] were reported, while iron(III) SCO complexes have an $[FeN_4O_2]$ core.[11] Cobalt, manganese, and chromium SCO complexes such as $[Co(dmvi)(phen)_2]$ (dmvi = dimethylviolurate anion),[12] [Mn(TRP)] (TRP = tris[1-(2-azolyl)-2-azabuten-4-yl]amine),[13] and $[CrI_2(depe)_2]$ (depe = 1,2-bis-(diethylphosphino)ethane)[14] were also reported. The SCO behavior

is generally observed in $3d^n$ (n = 4-7) transition metal ions with (pseudo) octahedral environments.

In SCO behavior, the macroscopic properties are understood on the basis of electron-phonon coupling and elastic properties of the crystal lattice. In the solid states, the cooperative spin transitions accompanied with hysteresis may be analyzed in the field theory of phase transitions as described by Slichter and Drickamer.[15] The SCO compounds with a polymeric structure show the hysteresis loops, because of the intermolecular interactions such as hydrogen bonds and π-π interactions.[16] For example, the mononuclear iron SCO complex $[Fe^{II}(pmpea)_2(NCS)_2]$ (pmpea = N'-(2'-pyridyl-methylene)-4-(phenylethynyl)-anilino) shows the wide thermal hysteresis loop (37 K).[17] Solvent molecules of crystallization and counter anions play important roles for the spin transition because of the intermolecular interaction.[18]

An important property of SCO complexes is light-induced excited spin state trapping (LIESST),[5(a)] which was first observed by Decurtins and co-workers in 1984.[19] Typical SCO complexes that show LIESST are $[Fe(Rtz)_6](BF_4)_2$ series (R = Me, Et, Pr, iPr; tz = tetrazole).[2(a)] Scheme 1-2 shows the schematic illustration of LIESST of Fe(II) complexes. When the LS sample was irradiated with green light at temperatures below 50 K, the spin allowed $^1A_1 \rightarrow {}^1T_1$ absorption was stimulated. The $^1T_1$ excited state has a short lifetime (~ns). The $^1T_1$ excited state decays via double intersystem crossing (ISC) through the intermediate spin state $^3T_1$ to reach the $^5T_2$ HS state. The $^5T_2$ state has a very long lifetime as the relaxation of $^5T_2 \rightarrow {}^1A_1$ is forbidden. The photo-induced back conversion of $^5T_2$ state known as reverse-LIESST effect was also reported. The SCO complexes are frequently used as building blocks of multifunctional materials by using functionalized ligands having properties such as fluorescence,[20(a),20(b)] conductivity,[20(c),20(d)] liquid-crystal[20(e)] and so on. The SCO complexes with the ligand having a photoisomerizable moiety, such as 4-styrylpyridine and diarylethene, show the ligand-driven

light-induced spin transition at room temperature.[21] The ligand-driven photo-switching may open a new way for future applications.

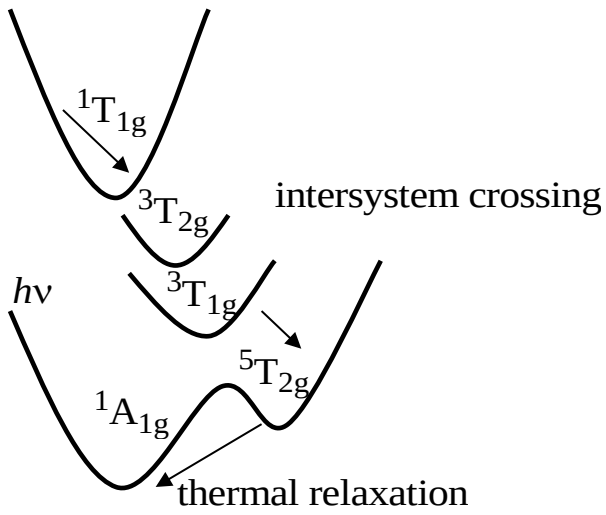

Scheme 1-2. Schematic illustration of LIESST.

1-3. Valence tautomeric (VT) complexes

VT complexes show the interconversion between redox isomers by temperature or pressure applied to the complexes.[3] The interconversion is accomplished by a reversible intramolecular electron transfer involving the metal ion and the redox active ligand. The interconversion is mainly an entropy-driven process. The entropy arises from the electronic entropy due to the higher spin state degeneracy of the high-spin Co^{II} form and the higher density of vibrational states of the high-spin Co^{II} form due to its longer metal-ligand bond lengths. Most of the VT complexes are reported by using dioxolene-type ligands, which are redox-active ligands that exist as neutral quinonate (Q), radical semiquinonate (SQ^-), or dianionic catecholate (Cat^{2-}) (Scheme 1-3).[22]

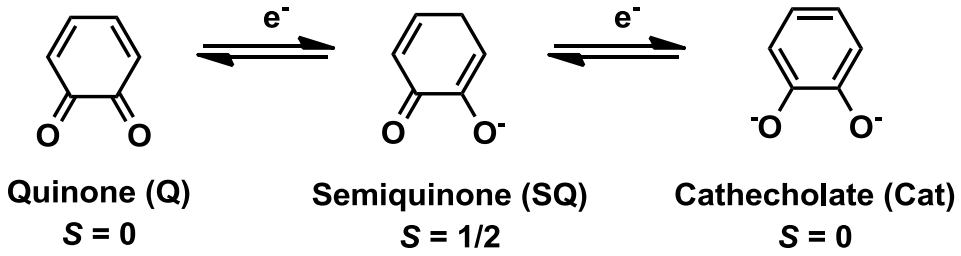

Scheme 1-3. Quinone molecules undergo two-step redox reactions.

The combination of dioxolene-type ligands and nitrogen-based ligands fulfills two conditions for the valence tautomerism: (1) the low covalency between metal ions and redox-active ligands; (2) a small energy difference between the two electronic isomers. In general, the VT complexes possess an $[N_2O_4]$ donor atom set, and the VT behavior is shown by the equilibrium between paramagnetic species in Equation (1).[22(a)]

$$[Co^{III}(bpy)(3,5\text{-DTBCat})(3,5\text{-DTBSQ})] \rightleftharpoons [Co^{II}(bpy)(3,5\text{-DTBSQ})_2] \qquad (1)$$

3,5-DTBCat and 3,5-DTBSQ refer to the catecholate and semiquinonate forms of 3,5-di-*tert*-butyl-*p*-benzoquinone and bpy is 2,2'-bipiridine. On the other hand, VT complexes with another donor atom set, $[N_4O_2]$, show the interconversion between diamagnetic and paramagnetic species in Equation (2).[23]

$$[Co^{III}(Me_2TPA)(3,5\text{-DTBCat})] \rightleftharpoons [Co^{II}(Me_2TPA)(3,5\text{-DTBSQ})] \qquad (2)$$

Me_2TPA is bis(6-methyl-2-pyridylmethyl)(2-pyridylmethyl)amine. In addition, compared with the $[N_2O_4]$-type complexes, $[N_4O_2]$-type complexes show the increase of stability under aerobic conditions.[24] In recent years, new redox-active ligands such as Schiff-bases,[26(a),26(b)] tetraphenylporphyrin[26(c),26(d)] and triphenylmethyl radicals[25(e)] were reported. Compared with SCO complexes, the examples of VT complexes are limited.

The occurrence of VT behavior is strongly affected according to surrounding environments. In particular, solvent molecules in crystals (Sol) play a key role. For example, the VT behavior of $[Co^{III}(phen)(3,5\text{-DTBCat})(3,5\text{-DTBSQ})](Sol)$ (**3**) is dependent on properties of the

solvent.[22(b)] The polycrystalline sample recrystallized from toluene shows the abruptly interconversion within a narrow temperature range of 30 K, while the sample recrystallized from ethanol does not show the VT behavior.

Some VT complexes show light-induced VT behavior (LIVT).[3(a),5(b)] The first LIVT experiments in solution were reported by Adams *et al*.[26] Also VT complexes for [Co^{III}(N-N)(3,5-DTBCat)(3,5-DTBSQ)] (N-N = 1,10-phenanthroline (phen), *N,N,N',N'*-tetramethyl-propylenediamine (tmeda), 2,2'-dipyridylamine (dpa)) series show LIVT in the solid state.[5(b),27] This phenomenon is understood in the following mechanism: (1) formation of LMCT excited state by photo-irradiation to the low-spin state; (2) a rapid intersystem crossing from such excited states to the high-spin state; (3) subsequent electron recombination to finally yield the low-spin isomer (Scheme 1-4). Ligand-driven light-induced VT behavior is also reported by Witt *et al*.[28]

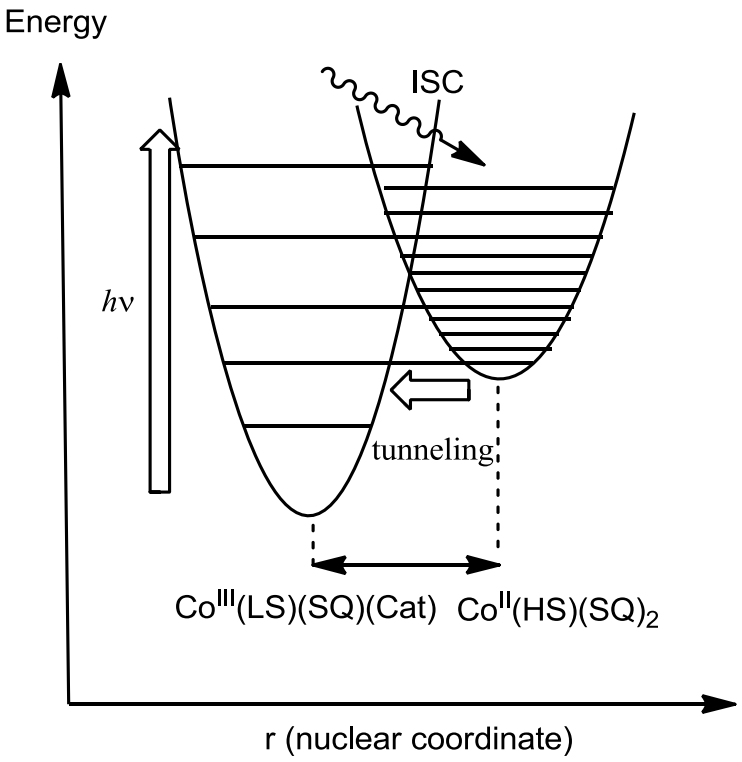

Scheme 1-4. Potential energy diagram for the Co valence tautomeric compounds.

1-4. π-Conjugated Spin System

The transient photo-induced spin alignment in the photo-excited state has been studied by using the organic π-conjugated spin systems, which are constructed from anthracene, a stable radical and functional moiety (Figure 1-2).[6,29,30]

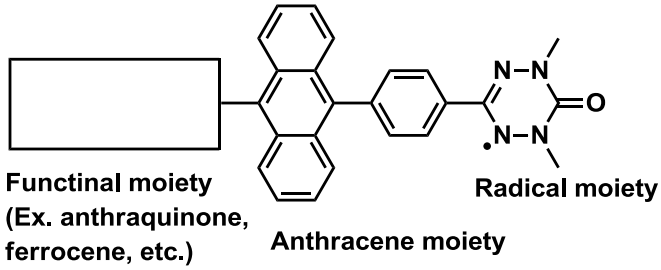

Figure 1-2. Molecular structures of π-conjugated spin systems.

These are ideal model systems to study the spin alignment[6,29,30] on photo-excited states, because they have the following advantages for materials science: (1) A strongly exchange coupled spin alignment is achieved compared to other triplet-radical exchange coupled systems (σ-bonded systems[31] and coordination complexes[32]); (2) The desired spin state can be designed well by taking the topology of the π-electron network (π-topology) into account[6,29]; (3) An enhanced intersystem crossing (EISC) owing to the spin–orbit coupling via π-conjugation to the radical spin is available[6,29] to open a new pathway for future applications. These π-radicals with high-spin photo-excited states are interesting because of fast photo-switching of the spin state and magnetic interactions and are also the prototypes of photomagnetic molecular devices.[33]

Functionalized π-radicals with energy or electron acceptor moieties also show the high-spin states of unique dynamic electron polarization, which are generated through quantum mixed photo-excited states, has been investigated both experimentally[30] and theoretically.[34] For example, when boron dipyrromethene (BODIPY) known as an energy acceptor of anthracene

are chosen as the functional moiety (Figure 1-3),[35] the unique spin dynamics is deduced in the following mechanism: (1) formation of BODIPY in the excited singlet states by photo-irradiation; (2) occurrence of photo-induced electron transfer (PET) from anthracene to BODIPY moieties; (3) generation of charge separated ion pair states; (4) subsequent electron recombination with ISC to anthracene in the excited triplet state (Scheme 1-5). Recently, Teki and coworkers reported that pentacene derivatives with a radical substituent shows the high solubility and remarkable stability to light due to ultrafast singlet–triplet conversion of the pentacene moiety in the photo-excited states.[36]

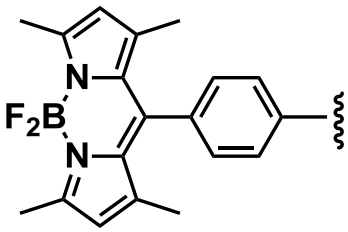

Figure 1-3. Molecular structure of BODIPY used in the π-conjugated spin system.

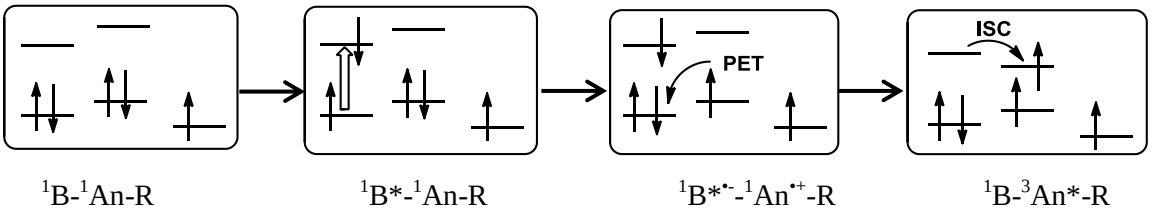

Scheme 1-5. The plausible mechanism of the generation of charge separated states (B = BODIPY, An = anthracene, R = radical).

1-5. This study

In this study, the author designed the following two π-conjugated spin systems: (i) a SCO iron complex containing a π-radical ligand with photo-excited high-spin state (Chapter 2); (ii) a VT cobalt complex with a dioxolene ligand functionalized by anthracene and BODIPY (Chapters 3 and 4).

1-5-1. a SCO iron complex containing a π-radical ligand with photo-excited high-spin state

The aim of the SCO complex with a π-radical ligand is to explore the ability of the π-radical ligand to display the photo-excited high-spin state (photo-excited high-spin π-radical ligand) to the spin-crossover including LIESST phenomenon. Here, the author presents a specific strategy of the photo-induced spin transition. The strategy for spin-crossover compounds exhibiting LIESST via a photo-excited high-spin state of π-radical ligand is shown in Figure 1-4. The author has chosen a Fe(II) spin-crossover complex which has two dihydrobis(1-pyrazolyl)borate ligands as the source of the spin-transition, in which the spin states (S) are 0 and 2 for low-spin (LS) and high-spin (HS) states, respectively (Figure 1-5). To utilize π-radical as a ligand, π-radical containing 2,2'-bipyridine as a coordination moiety was designed (Figure 1-5). When the π-radical ligand (**L**), which has a doublet ground state (S = 1/2) and a quartet lowest photo-excited state (S = 3/2), is used, the total ground state of [Fe(II) + **L**] is a doublet state (S = 1/2) in the LS phase and nearly degenerated quartet (S = 3/2) and sextet (S = 5/2) states in the HS phase (Figure 1-5), because the spin state of Fe(II) with S = 2 is expected to be coupled weakly with the unpaired spin of **L** with S = 1/2. As shown in Figure 1-4, the EISC from the doublet state to the quartet high-spin state occurs in the π-radical ligand by a photo-excitation of the ππ* transition,[6(b)] leading to a total photo-excited quartet state (S = 3/2) of [Fe(II) + **L**] complex. This photo-excited high-spin state is expected to be a spin allowed transition toward

the ground state in the HS phase and forbidden to that in the LS phase. Therefore, the photoinduced LS → HS transition is expected via the photo-excited high-spin quartet state of **L**, which is generated by the EISC.[6(a)] In addition, the antenna effect arising from the excitation of ππ* transitions with strong transition moments would provide efficient LIESST.

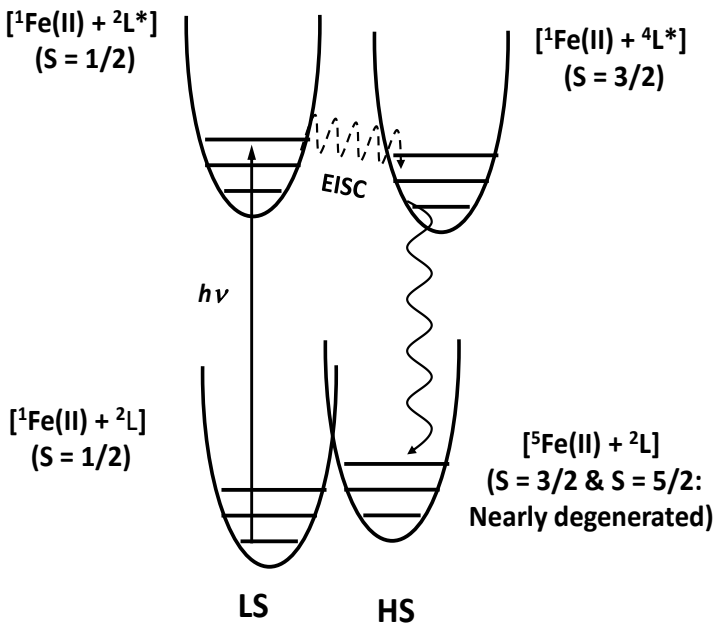

Figure 1-4. New strategy of LIESST via photo-excited high spin state of π-radical.

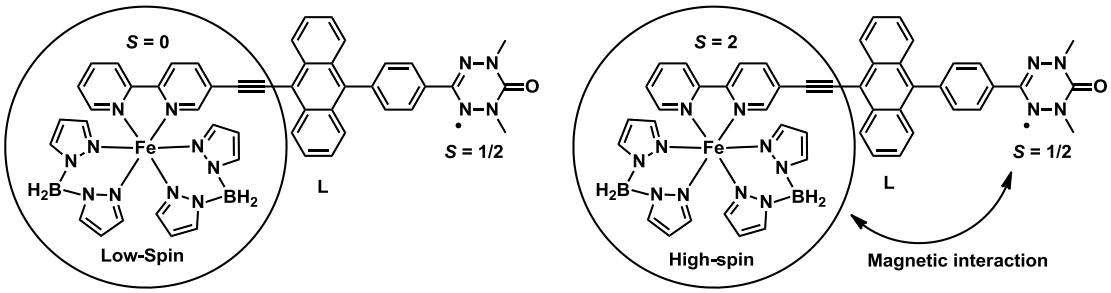

Figure 1-5. Molecular structures of [Fe(II) + **L**] for (left) the LS state and (right) the HS state.

1-5-2. a VT cobalt complex with a dioxolene ligand functionalized by anthracene and BODIPY

In VT complexes, theoretical studies suggest that the electric potential of VT is able to be used to both read and change the electric ground state of a VT system on conductive surfaces in an STM experiment.[37] However, only a few experimental applications of VT complexes have been reported.[38] To develop multifunctional materials, the author designed a π-conjugated spin systems consisting of a catecholate-semiquinonate VT cobalt complex, anthracene, and BODIPY as shown in Figure 1-6. The fluorescence switching is expected to be achieved by controlling the energy transfer from anthracene to BODIPY by the VT behavior of the cobalt complex moiety.

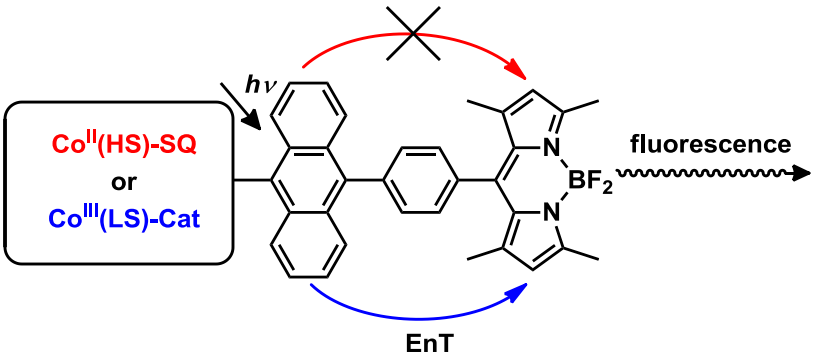

Figure 1-6. The switching of fluorescence by the spin dynamics on the photo-excited states affected by VT behavior.

BODIPY are used as applications in fluorescence indicator, luminescence devices, and photovoltaic devices because of the high fluorescence quantum yield, elevated photostability, sensitively to solvent polarity, and high absorption coefficients.[39,40] Previously, Burgess *et al* reported the energy transfer cassettes based on BODIPY and anthracene as energy acceptor and energy donor moieties, respectively.[35] In the anthracene-BODIPY system, nearly complete energy transfer from anthracene to BODIPY occurs to show the fluorescence from BODIPY.

On the other hand, the BODIPY-anthracene-radical system reported by Teki *et al*. shows a unique spin dynamics, which is the competition of the mechanisms via not only spin-orbit intersystem crossing but also a quantum-mixed charge separated ion-pair state.[30] The energy transfer efficiency from anthracene to BODIPY is suppressed by the existence of a radical moiety. Therefore, in this π-conjugated spin system, the change of the fluorescence intensity is expected from the energy transfer efficiency dependent on the spin states of the cobalt center. If the spin state of Co ion is in HS state, the energy transfer from the photo-excited singlet state of anthracene to BODIPY is inhibited by competitive spin-orbit intersystem crossing. Recently, Plenio *et al*. reported that fluorescence from Rh-BODIPY and Ir-BODIPY systems was strongly dependent on the electron density on the metal center.[41] Garcia *et al*. also reported that the emission wavelength of a SCO complex with a fluorophore depends on the spin state of the iron center in the solid state.[20(a)]

To construct the cobalt complex moiety, the author modified $[Co(dioxolene)(Me_nTPA)]^+$ systems (n = 0, tris(2-pyridylmethyl)amine; n = 1, (6-methyl-2-pyridylmethyl)bis(2-pyridylmethyl)amine; n = 2, bis(6-methyl-2-pyridylmethyl)(2-pyridylmethyl)amine; n = 3, tris(6-methyl-2-pyridylmethyl)amine) reported by Sorace *et al*.[23] The dioxolene moiety is connected to the anthracene-BODIPY system as shown in Figure 1-7.

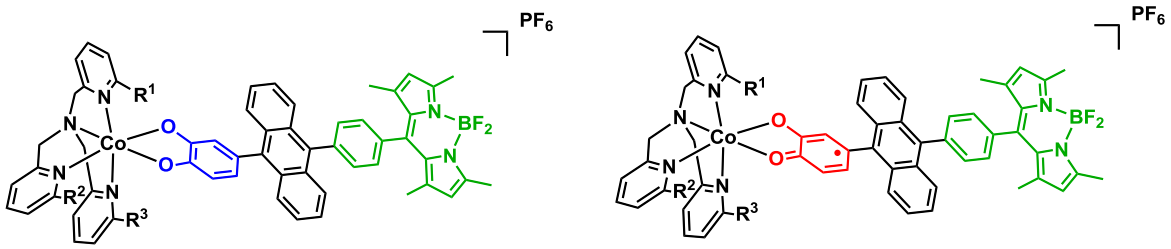

Figure 1-7. Molecular structure of the π-spin system for (left) Co^{III}(LS)-Cat form and (right) Co^{II}(HS)-SQ form (R^1, R^2, R^3 = H or Me).

The states of cobalt center is stepwise controlled by the number of Me group on the pyridine ring, and the Me_2TPA system (n = 2) is expected to show the VT behavior between diamagnetic Co(III)-Cat and paramagnetic Co(II)-SQ species. In Chapter 3, the VT behavior of cobalt complexes with an anthracene-containing dioxolene ligand shown in Figure 1-8 was studied to apply it to the fluorescence switching system.

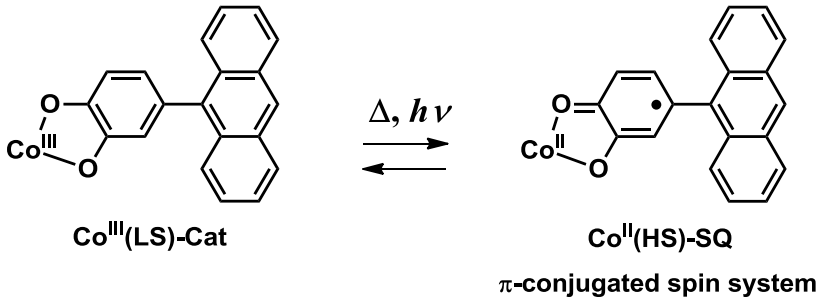

Figure 1-8. The switching of π-conjugated spin system by VT behavior.

Chapter 4 describes the synthesis and characterization of the target compounds consisting of the cobalt complex, anthracene, and BODIPY based on the results in Chapter 3. The influence of the spin states of the cobalt center to the fluorescence of BODIPY was investigated.

Chapter 2

Design, Synthesis, Structure and Properties of a π-Radical Ligand with Photo-Excited High-Spin State and Its Fe(II) complex

2-1. Introduction

It is well known that octahedrally coordinated Fe complexes show spin-crossover phenomenon.[2(a),2(b),5(a),] The phenomena are well investigated among Fe(II) complexes with d^6 electronic configuration, because of the following reasons: (I) they change from the LS state (S = 0) to the HS state (S = 2) by heat or light; (II) some of them show LIESST,[2(a)] (III) iron is the most abundant element. Therefore, in this work according to the strategy described in Section 1-5, the author has chosen the octahedrally coordinated Fe(II) complexes as the spin-crossover moiety and π-radical with the photo-excited high spin state as the ligand. In this system, the spin transition would be induced through the fast photo-switching of the spin state of the organic ligand. A synthetic approach to π-radical ligand includes two factors, the use of organic π-conjugated spin systems and the coordination moiety of N atoms. Octahedral Fe(II) spin-crossover complexes have nitrogen-based ligands (pyridine, NCS^-, bipyridine, etc). 2,2'-Bipyridine is good candidates for the coordination moiety because of the following advantages: (1) a stable N-N bidentate ligand; (2) the ease of modification; (3) utilization for the spin-crossover complexes.[8,18(c),42] Therefore, the author designed a new π-radical ligand, $\mathbf{L^1}$, which is constructed by linking 2,2'-bipyridine (bpy) to anthracene with oxo-verdazyl radical via ethynyl group (**Figure 2-1**).

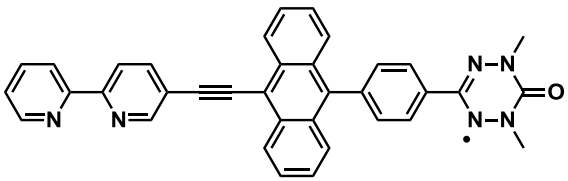

Figure 2-1. Molecular structure of $\mathbf{L^1}$.

The author used an iron complex [Fe(bpy){$H_2B(Pz)_2$}$_2$] {$H_2B(Pz)_2^-$ = dihydrobis(1-pyrazolyl)borate} (Figure 3-1) as a spin-crossover unit in the first model system of our strategy. The complex reported by Real *et al.* has a bipyridine ligand and shows SCO behavior and LIESST.[42] These results are compared with those of the control compound with a non-radical ligand to evaluate the effects of the π-radical moiety.

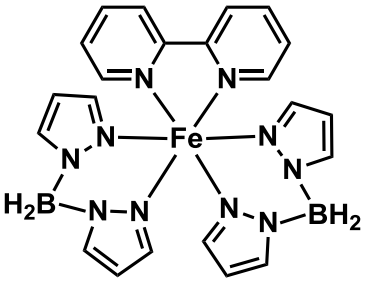

Figure 2-2. Molecular structure of [Fe(bpy){$H_2B(Pz)_2$}$_2$].

2-2. Results and discussion

2-2-1. Synthesis, structure and properties of a π-conjugated stable radical ligand of L^1

Ligand $\mathbf{L^1}$ was synthesized according to Scheme 2-1, and characterized by IR, NMR spectroscopy, and elemental analysis. The oxo-verdazyl radical in $\mathbf{L^1}$ was confirmed by ESR spectroscopy (*vide infra*), and the molecular structure of $\mathbf{L^1}$ was determined by X-ray analysis.

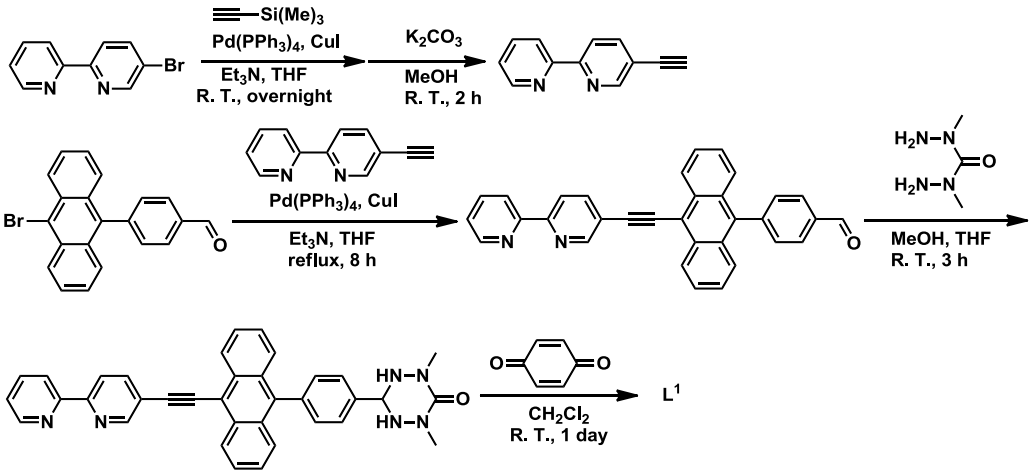

Scheme 2-1. Preparation of $\mathbf{L^1}$.

Figure 2-3 shows ^{1}H NMR spectrum of **L^{1}**. The signals of the bpy moiety were observed in the range of 9.13-7.84 ppm. The signals of phenylanthracene moiety were broadened at 8.5 ppm and 7.6-7.4 ppm. This finding suggests that the oxo-verdazyl radical formed.

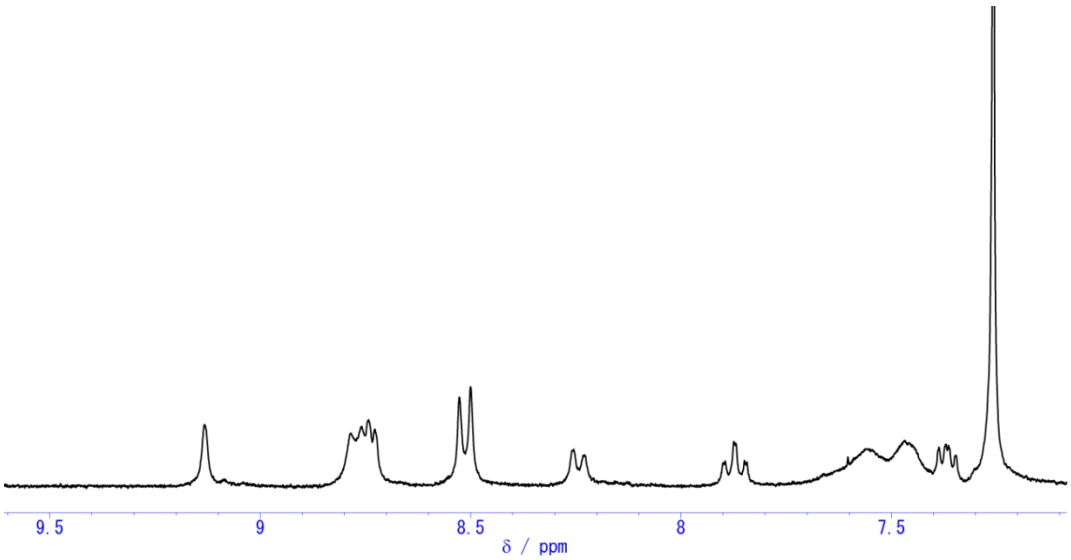

Figure 2-3. ^{1}H NMR spectrum of **L^{1}** in $CDCl_3$.

Figure 2-4 shows an ORTEP drawing of **L^{1}**. Selected bond lengths, angles and dihedral angles are listed in Table 2-1. The **L^{1}** molecule is located on a crystallographic C_2 axis through O1, C1, C3, C4, C7, C8, C15, C16, C17, C18, C21, C22, and C25 atoms. In the bipyridine moiety, N and C atoms adjacent to C21 and C22, and their attached H atoms are disordered over two sites with equal occupancy factors. The planarity of the oxo-verdazyl group is consistent with the formation of radical. The dihedral angle between the planes of anthracene and phenylene moieties in **L^{1}** is 76.03(5)°. The molecular orbital calculation of the ground state shows that the highest molecular orbital (HOMO) is localized within the phenylanthracene moiety and the slight delocalization of π-HOMO occurs in the bipyridyl group.

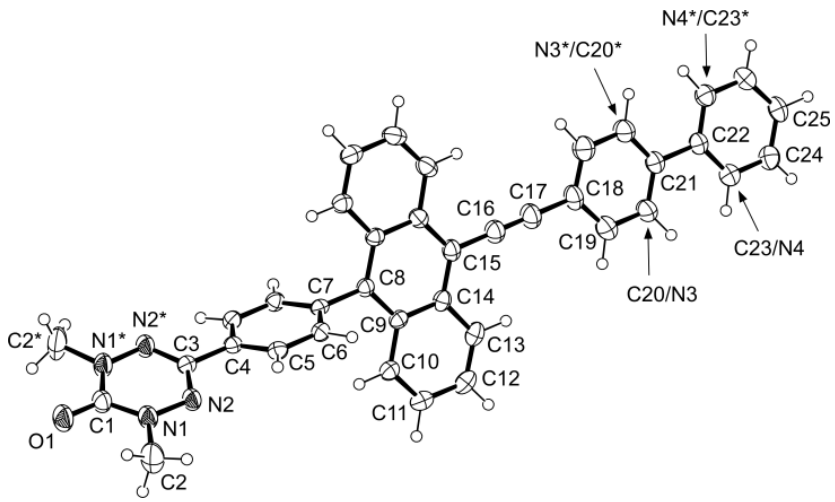

Figure 2-4. ORTEP drawing of the radical ligand **L**[1].

Table 2-1. Selected bond lengths (Å), angles (deg), and dihedral angles (deg) of

C(1)-O(1)	1.224(3)	N(1)-N(2)	1.3675(18)
C(1)-N(1)	1.3690(19)	N(2)-C(3)	1.3273(17)
C(3)-C(4)	1.478(3)	C(16)-C(17)	1.197(3)
N(1)-C(1)-N(1)*	114.4(2)	C(1)-N(1)-N(2)	124.46(15)
N(1)-N(2)-C(3)	114.64(14)	N(2)-C(3)-N(2)*	127.41(19)
plane[a]	plane[a]		
1	2	18.77(6)	
2	3	76.03(5)	
3	4	0.87(6)	

[a]plane 1, oxo-vedazyl moiety; plane 2, phenylene moiety; plane 3, anthracene moiety; plane 4, bipyridine moiety.

2-2-2. Magnetic properties of $\mathbf{L^1}$

The radical character of $\mathbf{L^1}$ in the ground state was confirmed with a solution ESR spectrum at room temperature (Figure 2-5). This spectral pattern is characteristic of oxo-verdazyl radical with the doublet ground state (S = 1/2) showing g = 2.0040 and typical hyperfine splitting arising from four nitrogen atoms (isotropic hyperfine coupling constants with $a_{N(2)} = a_{N(2)}^*$ = 0.65 mT and $a_{N(1)} = a_{N(1)}^*$ = 0.53 mT, N(1), N(1)*, N(2), and N(2)* correspond to those of $\mathbf{L^1}$ in Figure 2-4) and six protons (a_H = 0.53 mT) of methyl groups in the verdazyl radical moiety. These values are the same as those of the phenyl-verdazyl radical reported by Neugenbauer *et al*.[43] This shows that the SOMO of $\mathbf{L^1}$ is localized in the verdazyl moiety, which is consistent with the result of the density functional theory (DFT) calculation shown later (Figure 2-7(a)).

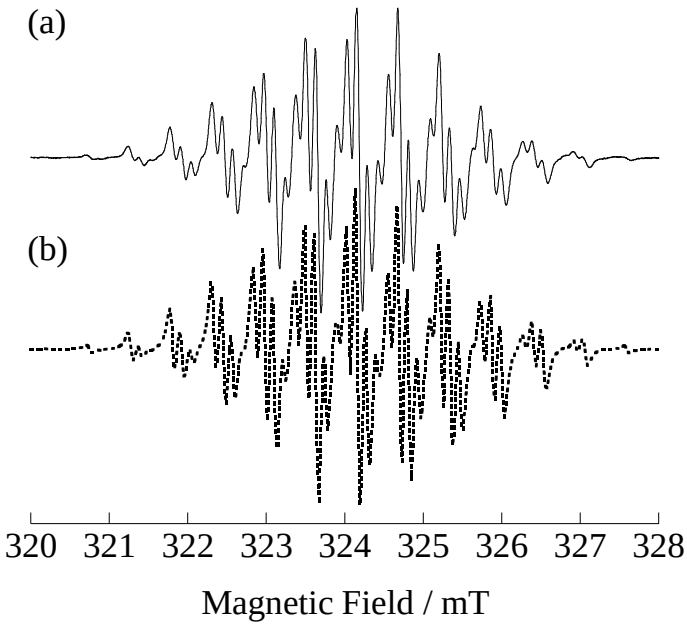

Figure 2-5. Solution ESR spectrum of $\mathbf{L^1}$ in CH_2Cl_2 with the spectral simulation. (a) Observed one, (b) Simulation.

To investigate the excited state of $\mathbf{L^1}$, we measured the timeresolved ESR (TRESR) spectrum using the $\mathbf{L^1}$ diluted in a frozen BuCN matrix. Figure 2-6 shows the observed TRESR spectrum of $\mathbf{L^1}$ together with a spectral simulation, which was observed 0.5 μs after nano-second pulsed

laser excitation by 355 nm light. The spectral simulation of the TRESR was carried out by the eigenfield[44]/exact diagnonalization hybrid method[45] of the spin-Hamiltonian (eqn (1)) taking the dynamic electronpolarization into account reported previously.[6]

$$H = g\beta_{\varepsilon}H\bullet S + S\bullet D\bullet S = g\beta_{\varepsilon}H\bullet S + D[S_Z^2 - S(S+1)/3] + E(S_X^2 - S_Y^2) \qquad (1)$$

From the spectral simulation, spin Hamiltonian parameters of $\mathbf{L^1}$ are determined to be S = 3/2, g = 2.0040, D = 0.0214 cm^{-1}, E = 0.0010 cm^{-1}. The dynamic electron polarization occurs to the Ms′ = ±1/2 sublevels of the zero-field spin-sublevels. This spectral pattern shows that the quartet state was only formed by enhanced spin-orbit intersystem crossing (SO-ISC). Other π-conjugated radicals having anthraquinone (**iv**)[30(b)] or ferrocene (**v**)[29(h)] instead of 2,2′-bipyridine show TRESR spectra similar to that of $\mathbf{L^1}$. Spin Hamiltonian parameters are listed in Table 2-2. The E value of $\mathbf{L^1}$ is lower than that of **iv**, this indicates that the symmetry of $\mathbf{L^1}$ in the lower excited state is slightly higher than that of **iv**.

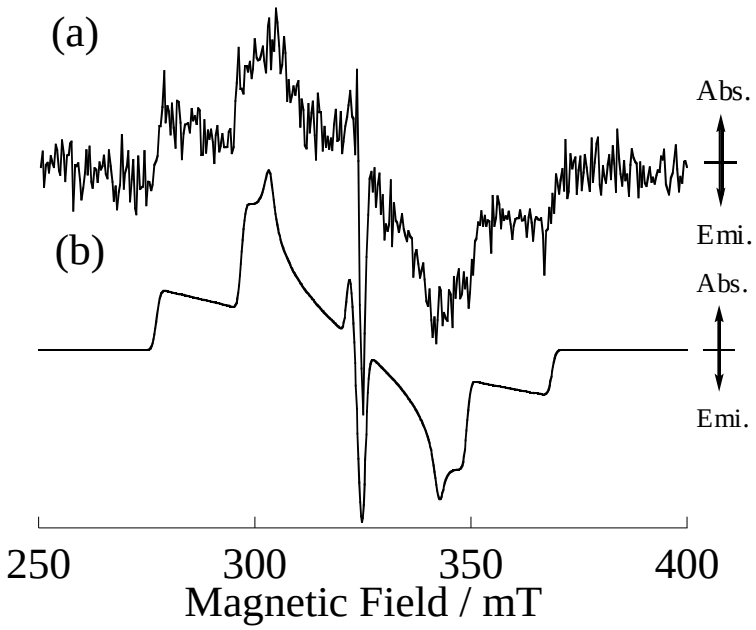

Figure 2-6. Time-resolved ESR spectrum of $\mathbf{L^1}$ at 30 K in BuCN glass matrix. "Abs." and "Emi." denote the absorption and emission of microwave. (a) Observed spectrum at 0.5 μs, (b) the spectral simulation.

Table 2-2. Spin quantum numbers *S*, g values, and zero-field splitting parameters of the lowest photo-excited states of **L**^{1}**, iv** and **v**

	S	*g*	*D* / cm^{-1}	*E* / cm^{-1}
L^1 (bpy)	3/2	2.0040	0.0214	0.0010
iv (anthraquinone)	3/2	2.0035	0.0214	0.0017
v (ferrocene)	3/2	2.0037	0.0240	0.0010

2-2-3. Electronic structures of L^1 by *ab-initio* MO calculations

To elucidate the physical properties of **L**^{1}, DFT calculations were performed at the unrestricted B3LYP/6-31G level. Figure 2-7 shows the spin density of the ground states and the photo-excited states of **L**^{1} obtained by DFT calculations. The calculated total spin density distribution in the doublet ground state shows that the unpaired electron is localized on the phenyl-verdazyl radical moiety (Figure 2-6(a)). This is consistent with the ESR parameters of **L**^{1} being very close to those of the phenylverdazyl radical.[2] In the photo-excited quartet state of **L**^{1}, the calculated spin densities suggest that two unpaired spins are mainly located on the central anthracene unit and the remaining one unpaired electron is located on the verdazyl radical moiety (Figure 2-7(b)). The unpaired electron of the triplet anthracene moiety is slightly delocalized to the bipyridine group and also to the radical moiety.

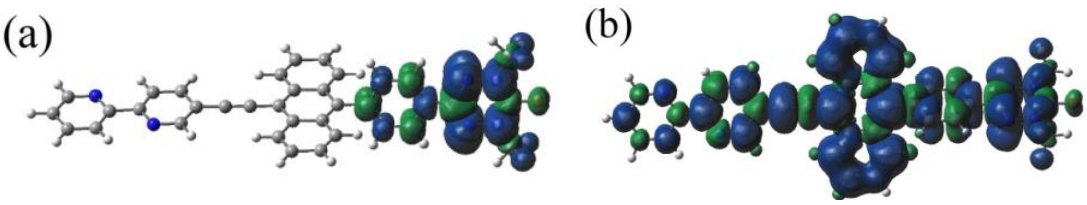

Figure 2-7. Spin densities of **L**^{1} and **1**. (a) The doublet (*S* = 1/2) ground state of **L**^{1}, (b) the quartet (*S* = 3/2) photo-excited state of **L**^{1}.

2-2-4. syntheses of L^2 and complexes 1 and 2

Non-radical ligand $\mathbf{L^2}$ was synthesized as a control compound according to Scheme 2-2, and characterized by IR, NMR spectroscopy and elemental analysis. Complexes $[Fe(\mathbf{L^1})\{H_2B(Pz)_2\}_2]$ (**1**) and $[Fe(\mathbf{L^2})\{H_2B(Pz)_2\}_2]$ (**2**) depicted in Figure 2-8 were synthesized from $\mathbf{L^1}$ and $\mathbf{L^2}$, respectively, by modifying the procedure reported by Real *et al.*[42] Both complexes were characterized by UV/Vis absorption spectroscopy, elemental analysis and magnetic measurements.

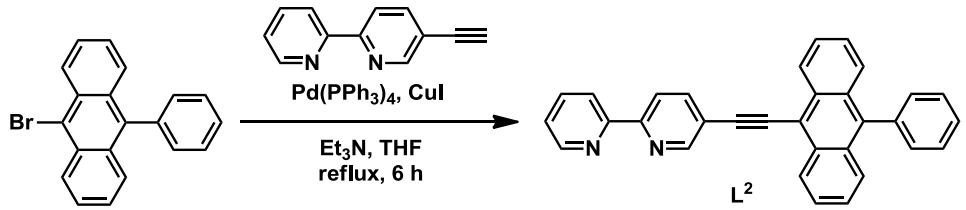

Scheme 2-2. Preparation of $\mathbf{L^2}$.

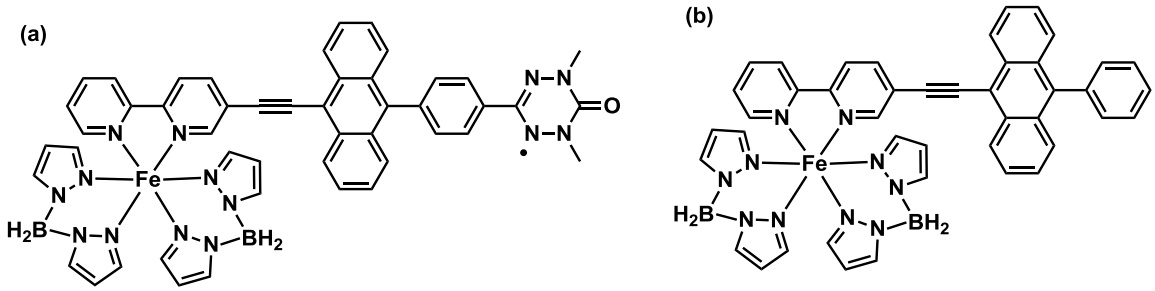

Figure 2-8. Molecular structures of complexes, (a) $[Fe(\mathbf{L^1})\{H_2B(Pz)_2\}_2]$ (**1**) and (b) $[Fe(\mathbf{L^2})\{H_2B(Pz)_2\}_2]$ (**2**).

2-2-5. Optical spectra of L^1 and complexes 1 and 2

UV/vis spectra of $\mathbf{L^1}$, **1** and **2** were measured at room temperature (Figure 2-9). The absorption bands of $\mathbf{L^1}$ at 360–460 nm are characteristic of the $\pi\pi^*$ transitions of an anthracene moiety. The excitation wavelength used in the TRESR shown in Figure 2-9 corresponds to the shoulder

of these ππ* transitions. This is one of the reasons of the weak intensity of the TRESR spectrum of the quartet high-spin state of $\mathbf{L^1}$. In **1** and **2**, the MLCT bands were observed at 600 nm in addition to the ππ* transition bands. The spectrum of $[Fe(bpy)\{H_2B(Pz)_2\}_2]$ contains two MLCT bands at 410 nm and 640 nm, which are assigned to the transitions from the metal dπ orbitals into π* orbitals of the ligands.[46] Therefore the MLCT with higher energy of **1** is overlapped by the ππ* bands of anthracene moiety. We used the wavelengths, 460 nm (ππ* band), 500 nm (the edge of ππ* band), and 600 nm (MLCT band) for LIESST experiments.

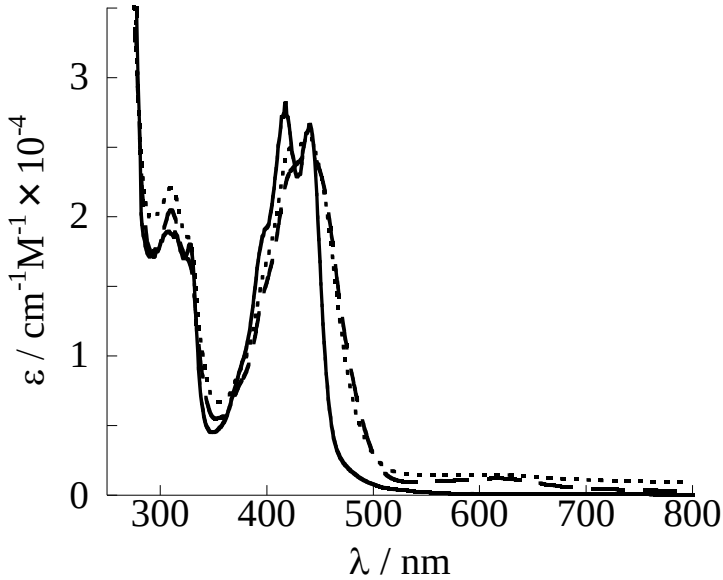

Figure 2-9. UV/Vis absorption spectra of $\mathbf{L^1}$ (−), **1** (…..), and **2** (−−−) at room temperature in dichloromethane.

2-2-6. magnetic properties of complexes 1 and 2

The temperature dependence of $\chi_M T$ (χ_M is molar magnetic susceptibility) for powder samples of **1** and **2** are shown in Figures 2-10(a) and 2-10(b), respectively. At 300 K, $\chi_M T$ for **1** is 3.2 emu K mol^{-1}, which is slightly larger than the spin-only value for high-spin Fe(II). The $\chi_M T$ value decreases gradually to 0.64 emu mol^{-1} K as the temperature is lowered to 30 K, and drops

suddenly below 10 K. This may be due to the intermolecular exchange interaction between the complexes. The value of 0.39 emu mol^{-1} K at 4 K corresponds to that of the radical ligand. The solid-line curve was obtained by the least-square fitting using the equation as follows.

$$\chi_{mol}T = C_0\alpha(\mathrm{Fe(HS)}) + C_1 \qquad (1)$$

where α(Fe(HS)) is the mole ratio of the high-spin Fe(II) ion and C_0 is expected to be ca. 3.4 emu mol^{-1} K from the data of the control compound **2** without radical species as shown in Figure2-10(b). The C_1 term is the paramagnetic contribution arising from the radical moiety and residual component of the high-spin state of Fe(II) (at low-temperature). The ratio is given in the non-interaction condition between the metal complexes by the following equation.[47]

$$\alpha(\mathrm{Fe(HS)}) = 1 / [1 + \exp\{(\Delta H / \mathrm{R})(1 / T - 1/ T_c)\}] \qquad (2)$$

The estimated values from the curve fitting are listed in Table 3-1. The transition entropy ΔS was estimated to be 36.4 J K^{-1} mol^{-1} from the relation of $\Delta S = \Delta H/T_c$. C_1 = 0.686 emu K mol^{-1}, which is slightly larger than the spin-only value of the $\mathbf{L^1}$ radical species and due to the residual component of Fe(II) species in the high-spin state (see Figure2-10(b); similar residual contribution was observed at the low-temperature region of complex **2**). It was unsuccessful because the small magnitude of the exchange coupling J, although we tried to estimate the magnitude of the exchange interaction between the high-spin Fe(II) unit and the radical moiety of $\mathbf{L^1}$ using the analytical formula:

$$\chi_{mol} = (N_A\mu_0\mu_B^2 / k_BT)[\alpha(\mathrm{Fe(HS)}) \times (10 + 10\exp(3J / k_BT)) / (1 + 2\exp(3J / k_BT))$$
$$+ (1 - \alpha(\mathrm{Fe(HS)})] + (\text{residual component of HS}) \qquad (3)$$

As shown in Figure 2-10(a), the gradual spin-transition was observed in **1**. The estimated ΔH and ΔS values are smaller than those reported in [Fe(bpy){$H_2B(Pz)_2$}$_2$], showing that **1** has smaller cooperativity compared with [Fe(bpy){$H_2B(Pz)_2$}$_2$].

On the other hand, abrupt spin conversion was observed in **2**. This behavior is similar to that

found for [Fe(bpy){$H_2B(Pz)_2$}$_2$]. The $\chi_M T$ value of **2** is 3.5 emu mol^{-1} K at 300 K, which is expected for high-spin Fe(II). This value slowly decreases upon cooling. In the temperature range (180 K–130 K), the $\chi_M T$ product for **2** suddenly decreases to 0.50 emu mol^{-1} K, then decreases smoothly from 0.50 emu mol^{-1} K at 150 K to 0.09 emu mol^{-1} K at 4 K, which corresponds to low-spin Fe(II) with S = 0. The non-zero value at 4 K is due to the contamination of the high-spin Fe(II). The solid-line curve was obtained by the least-square fitting using eqn (2). The temperature dependence was well analyzed by eqn (2). The estimated values from the curve fitting are listed in Table 2-3.

Table 2-3. The estimated values from the curve fitting for **1** and **2**.

	C_0	$\Delta H/R$	ΔH	T_c	ΔS	C_1
1	3.18	973 K	8.09 kJmol^{-1}	222 K	36.4 J K^{-1}mol^{-1}	0.686 emu K mol^{-1}
2	3.36	2693 K	22.39 kJ mol^{-1}	162 K	138 J K^{-1} mol^{-1}	0.10 emu K mol^{-1}

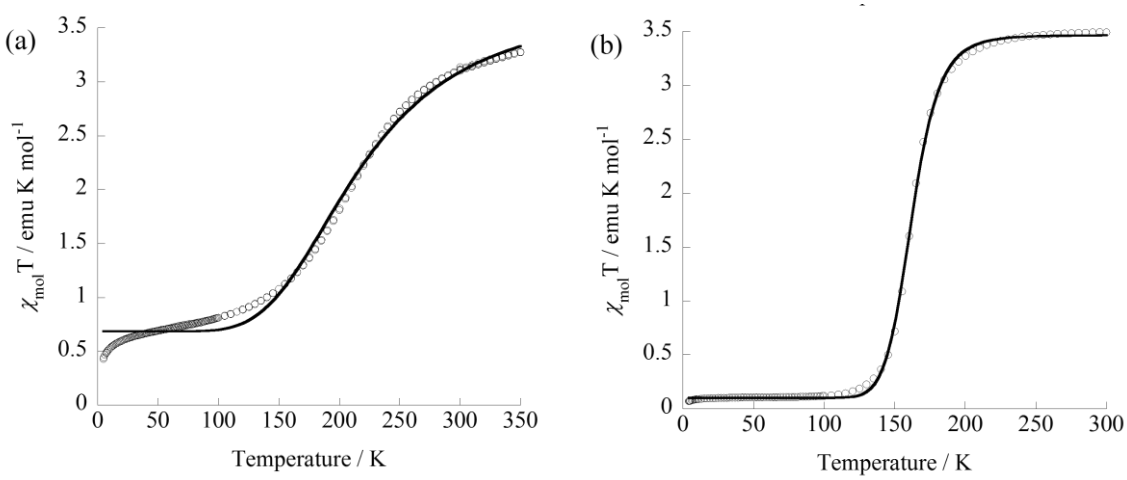

Figure 2-10. Temperature dependence of molar magnetic susceptibilities for (a) **1** and (b) **2**. The solid curves are simulated ones using eqn (2).

2-2-7. Photo-magnetic properties of complexes 1 and 2

The LIESST experiments were performed on **1** and **2** by using pulse laser (OPO + Nd : YAG ns

pulse laser). A similar procedure was used for the two powdered samples of **1** and **2**. The compound was first slowly cooled from room temperature to 5 K and the photo-irradiation was carried out at 5 K. Figures 2-11(a) and 2-11(b) show the temperature dependence of the $\chi_M T$ product recorded for **1** and **2**, respectively. The magnetic moment was immediately increased by the photo-irradiation, reaching almost constant after 20 min irradiation. This LIESST effect was observed below ca. 50 K. The saturated magnitude ($\Delta M_{saturated} = (\chi_M T)_{saturated} - (\chi_M T)_{no\text{-}irradiation}$) of the increase of the $\chi_M T$ value by the irradiation at 5 K were 0.5 emu mol^{-1} K (460 nm), 0.75 emu mol^{-1} K (500 nm), and 1.0 emu mol^{-1} K (600 nm) for **1**. Their wavelengths, 460 nm, 500 nm and 600 nm, correspond to the excitation band of ππ* transition of the anthracene moiety, nπ transition of the verdazyl radical moiety, and MLCT band between pyridinyl group and Fe(II) metal, respectively. Similar LIESST phenomena were observed for the control compound **2** below ca. 50 K. The $\Delta M_{satulated}$ values were 0.7 emu mol^{-1} K (460 nm), 2.2 emu mol^{-1} K (500 nm), and 2.7 emu mol^{-1} K (600 nm) for **2**. The temperature was increased at a rate of 0.4 K min^{-1} after the light irradiation was stopped. The magnetic moments were first slightly increased with increasing temperature and reaching the maximum at 20 K. The maximum values were 1.2 emu mol^{-1} K (600 nm) for **1** and 3.6 emu mol^{-1} K (600 nm) for **2**. For further heating, the magnetic moment dropped quickly in a narrow temperature range.

Complexes **1** and **2** exhibited the LIESST phenomena in a wide range of wavelengths of light irradiation, which includes the ππ* band (400–500 nm) of the π-radical ligand as well as the MLCT transition around 500–680 nm. This means that the aromatic rings of the organic ligand play the role of antenna. However, the efficiency of the photo-conversion decreased in the order of irradiation at 600 nm > 500 nm > 460 nm, which suggests that the MLCT transition from Fe(II) to the bipyridyl group is more effective than the ππ* transition of the anthracene moiety in the LIESST. The LIESST for the π-radical complex **1** was suppressed compared with **2**: the

photo-conversion using 600 nm light was ca. 30% for **1** and almost 100% for **2**. Probably, in **1** an energy transfer from the anthracene moiety to the radical moiety occurs competitively, leading to a non-irradiative relaxation process to the ground state through the radical moiety. In order to investigate the photo-excited states of **1**, [Fe(**L**^{1}){$H_2B(Pz)_2$}$_2$] and the energy transfer to the high-spin photoexcited state, the TRESR experiments were also carried out. We tried to measure the high-spin photo-excited state of **L**^{1} coupled to the Fe(II) high-spin complex. While, TRESR was not observed in **1**, showing the low-efficiency of the intersystem crossing toward the high-spin state, probably because of the rapid energy relaxation to the ground state through the Fe site.

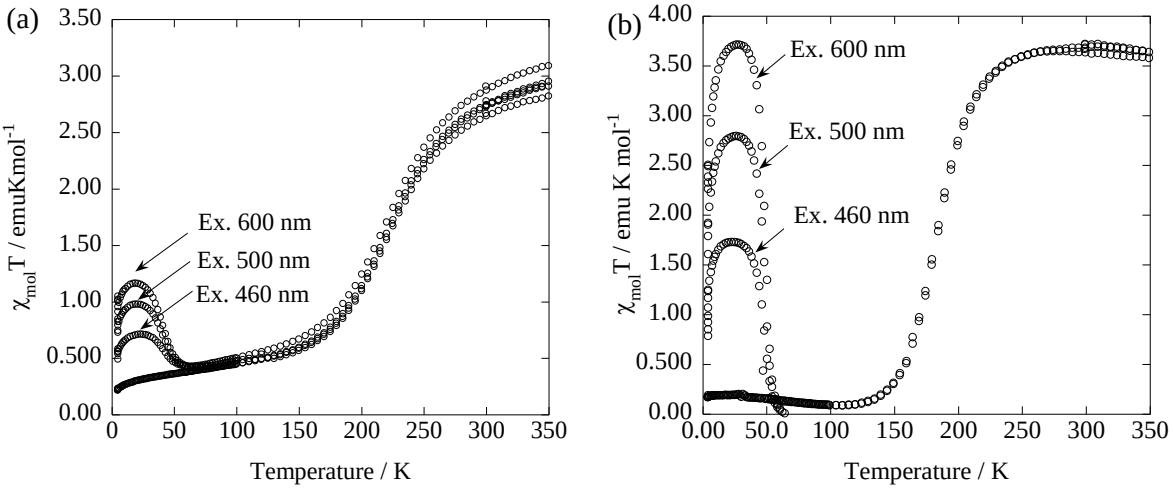

Figure 2-11. Temperature dependence of magnetic susceptibilities and LIESST phenomena for (a) **1** and (b) **2**. The magnitude of the susceptibility was corrected using the data of the bulk powder sample.

2-2-8. Electronic structures of complex 1 by *ab-initio* MO calculations

Structures of **1** in the low-spin state (S = 1/2) and the ferromagnetically coupled high-spin state (S = 5/2) were optimized by the DFT method using the unrestricted B3LYP/LANL2DZ basis sets. Figure 2-12 shows the spin density of the ground states and the photo-excited states of **1**

obtained by DFT calculations. The spin density distribution in the LS state (S = 1/2) of **1** shows that the unpaired electron exists on the phenyl-verdazyl radical moiety (Figure 2-12(a)), which is similar to the ground state of $\mathbf{L^1}$. In the high-spin state (S = 5/2) of **1**, the unpaired electrons are located on the Fe center and the phenylverdazyl radical moiety (Figure 2-12(b)).

According to the spin density of the photo-excited quartet high-spin state of $\mathbf{L^1}$, a weak exchange interaction between the Fe(II) metal and the quartet excited state of $\mathbf{L^1}$ is expected in the excited state of **1**, [^{1}Fe(II) + $^4\mathbf{L^1}$*]. In contrast, in the meta-stable ground state of **1**, [^{5}Fe(II) + $^2\mathbf{L^1}$], almost no exchange-interaction is predicted between the S = 2 high-spin state of Fe(II) and the S = 1/2 state of $\mathbf{L^1}$, giving the quantum-mixed state of S = 3/2 and S = 5/2. The electronic energy difference between the LS and HS states of **1**, E_{HS}(B3LYP) − E_{LS}(B3LYP), was calculated to be 8.81 kJ mol^{-1} from the DFT calculation, in which the LS state has slightly lower energy. The energy difference corrected for zero-point energy by the frequency calculation is −4.051 kJ mol^{-1}, showing the lower energy of the HS state and the inconsistency with the magnetic data below T_c. However, these small energy differences are reasonable because the experimental data contain the intermolecular interactions and cooperative effect in the solid state, which will become more important at low-temperature region. Gibbs free energy correction of **1** at 298.15 K and 1 atm were obtained from harmonic vibrational frequencies without scaling factors. After the thermodynamic correction, the HS state becomes more stable than the LS state: the energy difference is −11.55 kJ mol^{-1}, which is consistent with the magnetic data at room temperature.

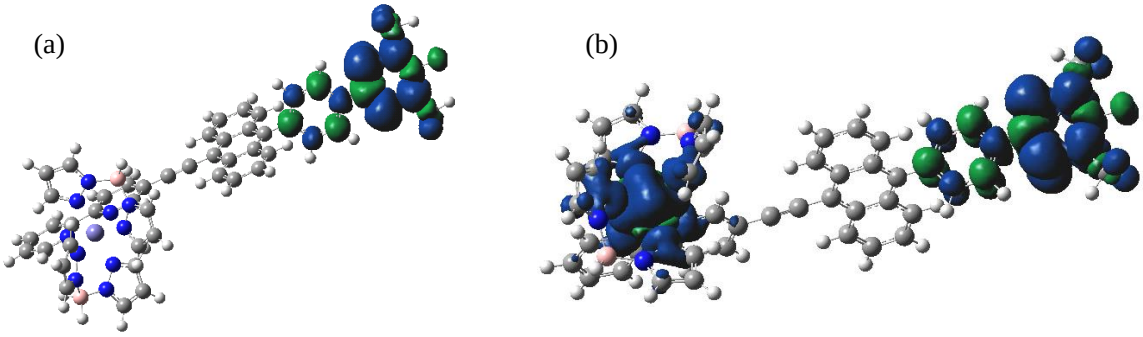

Figure 2-12. Spin densities of **1**. (a) Tthe doublet ground state of **1**, (b) the sextet (*S* = 5/2) meta-stable ground state of **1**.

2-3. Conclusion

Ligand $\mathbf{L^1}$ containing bipyridine, anthracene and verdazyl radical moieties was synthesized by using Pd-catalyzed coupling and oxidation reactions. The characterization was performed by ^{1}H NMR, ESR spectroscopy and X-ray crystal analysis. The π-radical ligand $\mathbf{L^1}$ has a doublet state in the ground state, and the localization of unpaired electron on phenyl-verdazyl radical moiety is indicated by the ESR spectral pattern. The result is supported by DFT calculation. The photo-excited quartet (S = 3/2) state of $\mathbf{L^1}$ was detected by time-resolved ESR. The spin state is constructed by the intramolecular ferromagnetic spin alignment between the doublet spin state of the oxo-verdazyl radical and ππ* excited triplet state of the phenylanthracene moiety. Spin Hamiltonian parameters of $\mathbf{L^1}$ are similar to those of the excited quartet states of other anthracene-π-radical exchange coupled systems. According to the spin density of the photo-excited quartet high-spin state of $\mathbf{L^1}$, a weak exchange interaction between a metal ion and $\mathbf{L^1}$ is expected.

The iron(II) complexes [Fe($\mathbf{L^1}$){$H_2B(Pz)_2$}$_2$] (**1**) and [Fe($\mathbf{L^2}$){$H_2B(Pz)_2$}$_2$] (**2**) were synthesized, where $\mathbf{L^2}$ has no verdazyl radical moiety. Complexes **1** and **2** showed spin conversion between LS and HS: the T_c values are 222 K and 162 K, respectively. The spin transition of **1** occurred gradually compared with that of **2**, indicating the cooperative effect among the complexes in the crystal smaller than that of **2** or [Fe(bpy){$H_2B(Pz)_2$}$_2$] reported in the literature. In both complexes **1** and **2**, LIESST phenomena were observed in a wide range of wavelengths of the excitation light. Their wavelengths, 460 nm, 500 nm and 600 nm, correspond to the excitation band of ππ* transition of the anthracene moiety, the nπ transition of the verdazyl radical moiety, and the MLCT transition from Fe(II) to the bipyridyl group, respectively. Thus, an antenna effect by the π-conjugated ligand was observed. The direct excitation of the MLCT band was the most efficient in LIESST, which suggests that an energy

transfer occurs from the ππ* excited state of the anthracene moiety or nπ state of the radical moiety to the LMCT state. In complex **1**, only 30% of low spin molecules were photoconverted. In contrast, almost 100% photoconversion was achieved in the control complex **2** by excitation on the MLCT band. A possible explanation for these findings is that the rapid energy transfer or the energy relaxation to the LS ground state by the non-irradiative transition through radical moiety, which overcomes the efficiency of the intersystem crossing to the quartet high-spin state of the π-radical ligand confirmed by the time-resolved ESR experiment. In order to make the LIESST effect via the intersystem crossing in the π-ligand more efficiently, an improvement of the system is required, which leads to more efficient intersystem crossing via a charge-separated quantum-mixed state followed by so-called "radical-pair intersystem crossing" arising from the de-coherence (loss of the quantum coherence) during the charge-recombination.

Because SCO and LIESST behavior are affected by the surrounding environments, another approach for improvement of the system is the change of intermolecular interactions, which can be affected by solvent molecules and counter ions. In this study, the obtained iron complexes are neutral, and have low solubility to any organic solvents other than CH_2Cl_2. As a solution of the difficulty, an ionic iron complex by using neutral supporting ligands such as 2,2'-bi-1,4,5,6-tetrahydropyrimidine[18(c)] would be useful. Additionally, counter ions also are helpful for the introduction of functional components.[48]

Chapter 3

Synthesis, Magnetic Properties and Dynamic Behavior of Cobalt Complexes with an Anthracene-Containing Dioxolene Ligand

3-1. Introduction

Some octahedral cobalt complexes with the combination of dioxolene and nitrogen-based ligands show valence tautomerism (VT).[3] This phenomenon is accomplished by a reversible interconversion between electronic isomers by heat or light and so on. As mentioned in section 1-5, the study of VT complex as the building blocks for multifunctional materials is rare,[38] because surrounding conditions such as solvent molecule strongly affect whether VT behavior occurs or not.[22(b)] However, DFT calculation indicated the utility of VT complexes for future applications.[37] As mentioned in chapter 1, the author designed the three-component switching system consisting of the VT complex, anthracene and the fluorescence moiety. In this chapter, the author first investigated the combination of anthracene and VT complexes by using 9-(3,4-dihydroxyphenyl)anthracene (**H_2L^3**) as a ligand, because the $[N_4O_2]$-type dioxolene cobalt complexes, showing VT behavior between diamagnetic and paramagnetic species, have been reported.[23] Magnetic properties in the solid state and dynamic behavior in solution, as well as spectroscopic properties, were investigated for the cobalt complexes $[Co(\mathbf{L^3})(TPA)]PF_6$ (**3**) and $[Co(\mathbf{L^3})(Me_nTPA)]PF_6$ (n = 1, **4**; n = 2, **5**; n = 3, **6**) (Figure 3-1).

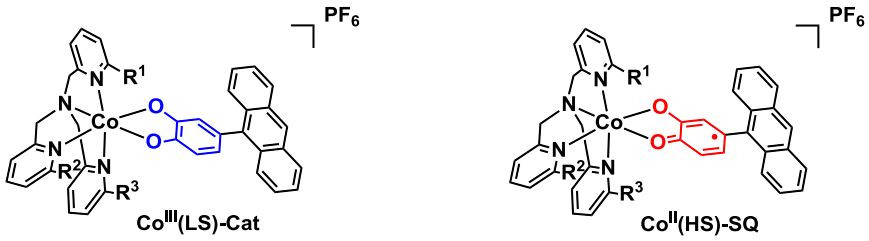

Figure 3-1. Molecular structures of the Co^{III}-Cat form (left) and the Co^{II}(HS)-SQ form (right) (R^1, R^2, R^3 = H or Me).

3-2. Results and discussion

3-2-1. Synthesis and properties of H_2L^3 and cobalt complexes

Anthracene-containing dioxolene, $\mathbf{H_2L^3}$, was synthesized from 9-bromo-anthracene and 3,4-dimethoxyphenylboronic acid according to Scheme 3-1. The characterization was performed by IR, NMR spectroscopy and elemental analysis. Complexes **3**-**6** (Figure 3-1) were obtained by the reaction of cobalt(II) dichloride with $\mathbf{H_2L^3}$ and Me_nTPA followed by aerobic oxidation.

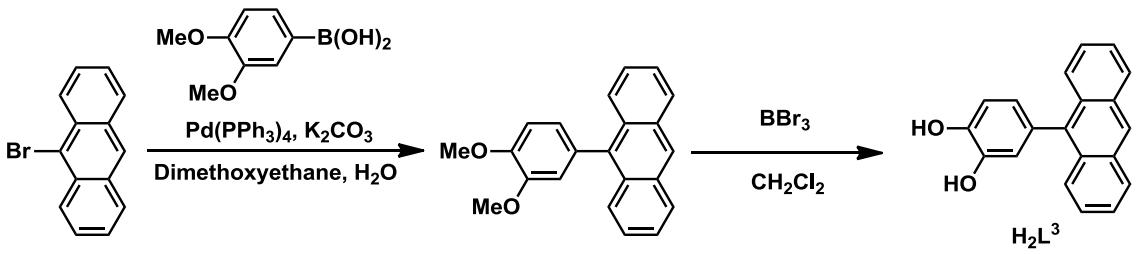

Scheme 3-1. Synthesis of $\mathbf{H_2L^3}$

Infrared spectroscopy contributes to distinguish between catecholate and semiquinonate forms of the coordinated ligand, because of the different frequencies of the C-O and C=C stretching modes.[49] IR spectra of complexes **3**-**6** show the characteristic bands of catecholate complexes assigned to the skeletal dioxolene at 1479 and 1250 cm^{-1} for **3**, 1481 and 1256 cm^{-1} for **4**, and 1491 and 1259 cm^{-1} for **5** (Figure 3-2). In complex **5**, a new band appears at 1577 cm^{-1}, which is attributed to C=C stretches of the semiquinonate moiety. In complex **6**, the catecholate bands disappeared, and semiquinonate bands appeared at 1577 and 1452 cm^{-1}. The IR data suggest that complexes **3** and **4** contain cobalt(III) catecholate species, Co^{III}-Cat, while **6** is a cobalt(II) semiquinonate complex, Co^{II}-SQ. Complex **5** contains both of the Co^{III}-Cat and Co^{II}-SQ forms.

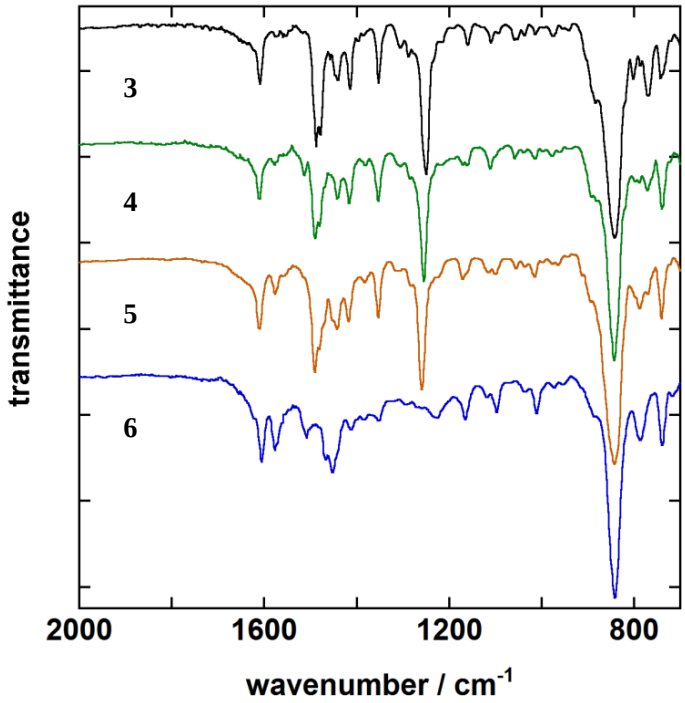

Figure 3-2. IR spectra of complexes **3-6** at room temperature.

UV-vis spectra of complexes **3-6** are shown in Figure 3-3. In all complexes, the characteristic bands of ππ* transitions of an anthracene moiety were observed at around 370 nm. The spectra of **3** and **4** show the absorption band at 420 nm as a shoulder, which is due to the LMCT transitions from the catecholate π* orbital and overlapped by the edge of the ππ* transition band. The broad absorption band at 600-900 nm are assigned to the symmetry-forbidden LMCT transitions.[50] These features are consistent with the low-spin cobalt(III) catecholate complexes, Co^{III}(LS)-Cat.[23] Complex **6** shows the MLCT transition bands at around 550 nm and the broad absorption bands being related to internal ligand transition at 700-900 nm.[51] The spectral pattern is consistent with that of high-spin cobalt(II) semiquinonate complexes, Co^{II}(HS)-SQ.[52] The spectrum of **5** exhibits absorption bands due to LMCT (420 nm) and MLCT (550 nm). This indicates that complex **5** exists as a mixture of Co^{III}(LS)-Cat and Co^{II}(HS)-SQ in solution at room temperature.

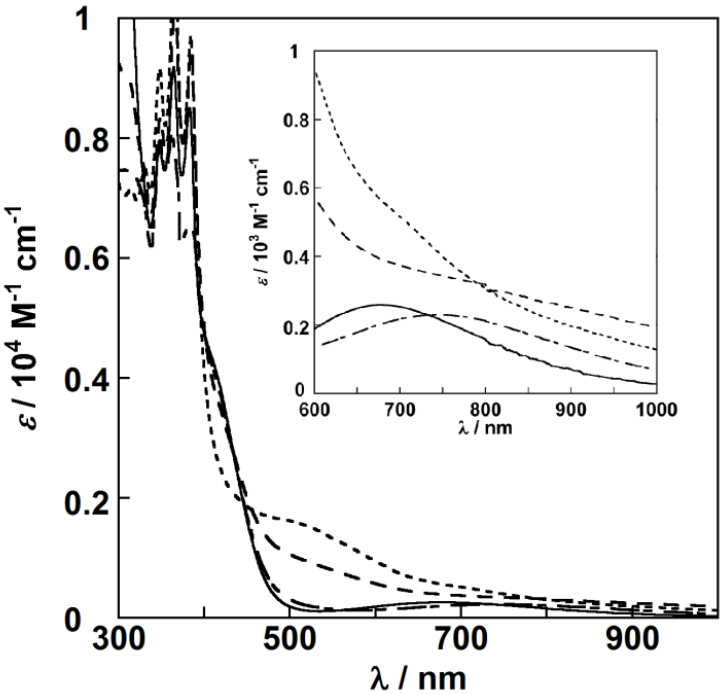

Figure 3-3 UV-vis absorption spectra of complexes **3** (—), **4** (— - —), **5** (– – –), and **6** (---) at room temperature in acetonitrile solutions.

At room temperature, the ^{1}H NMR signals of complexes **3** and **4** showed normal chemical shifts with line broadening (Figure 3-4). This line broadening is related to dynamic behavior of the complexes, which is discussed later. The ^{1}H NMR spectrum of **5** exhibits the considerable broadening, and any signals of **6** were not observed, indicating the presence of **6** as Co^{II} semiquinonate (Figure 3-4). These results are consistent with the solution behavior expected from the absorption spectra.

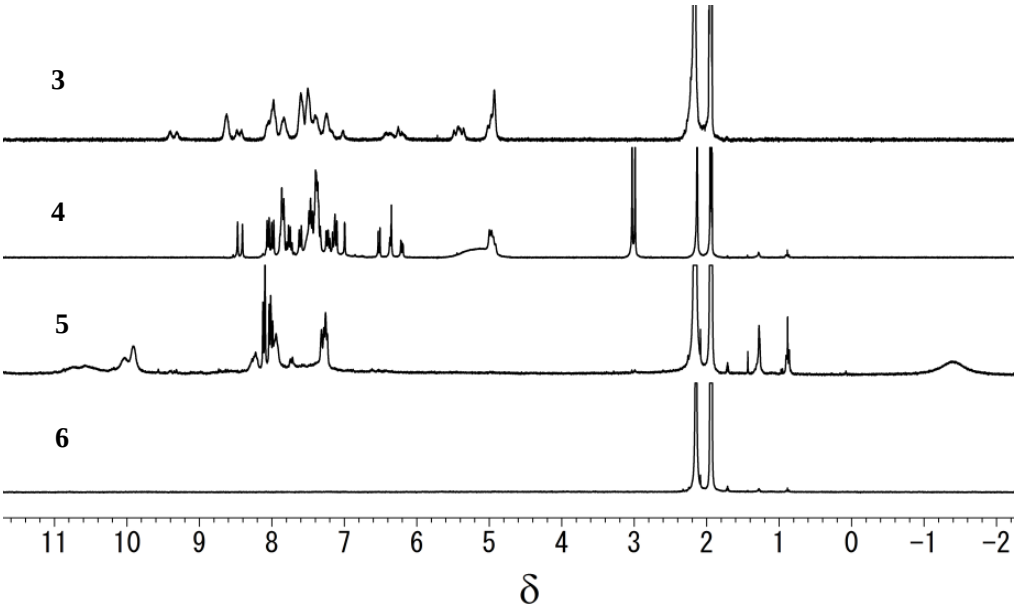

Figure 3-4. ^{1}H NMR spectra (300 MHz) of complexes **3**-**6** at room temperature in acetonitrile-d_3.

Complex **6** was structurally characterized by a single crystal X-ray analysis. Figure 3-5 shows an ORTEP drawing of the cation part of **6**. Selected bond lengths, angles and dihedral angles are listed in Table 3-1. The Co ion is in a six-coordinate distorted octahedral environment consisting of a catecholate ligand and a Me_3TPA ligand. The bond lengths around Co are 2.023(3) and 2.093(3) Å for Co-O, and 2.116(3)-2.300(4) Å for Co-N. The bond lengths are consistent with those of Co^{II} semiquinonate complexes such as $[Co(Me_2TPA)(diox)]PF_6$ (diox = 3,5-di-*tert*-butyl-1,2-dioxolene),[23] $[Co(Me_4cyclam)(diox)]PF_6$ (Me_4cyclam = 1,4,8,11-tetramethyl-1,4,8,11-tetraazacyclotetradecane, diox = 9,10-phenanthrenecatecholato)[52(a)] and $[Co(Pz_3)(diox)]PF_6$ (Pz = tris(3,5dimethyl-1H-pyrazol-1-yl)methyl)amine, diox = 3,5-di-*tert*-butyl-1,2-dioxolene).[52(b)] The dihedral angle between catecholate and anthracene planes is 75.99(12)°.

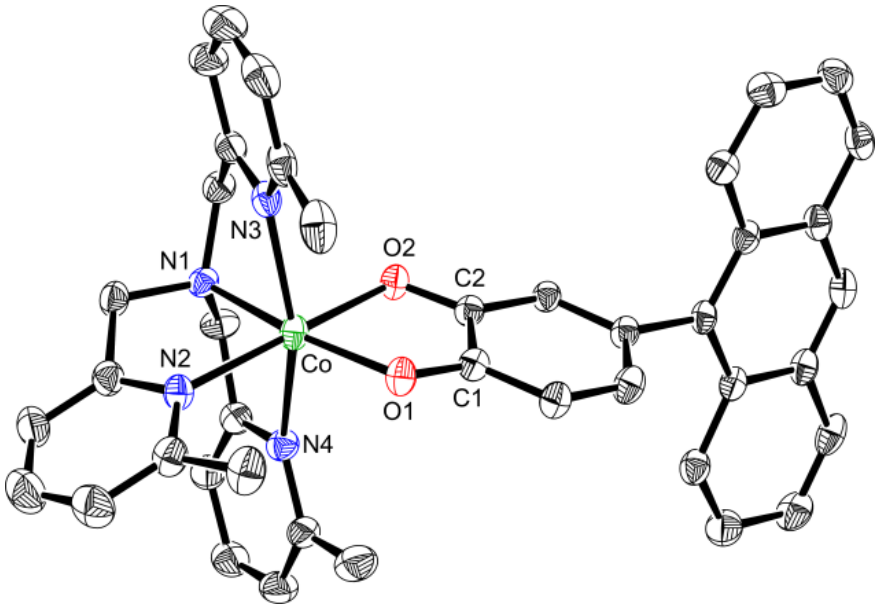

Figure 3-5. ORTEP drawing of the cationic unit of **6** with thermal ellipsoids at the 30% probability level. Hydrogen atoms are omitted for clarity.

Table 3-1. Selected bond lengths (Å), angles (deg) and dihedral angle (deg) of **6**

Co-N(3)	2.209(4)	Co-N(4)	2.300(4)
O(1)-C(1)	1.283(5)	O(2)-C(2)	1.281(5)
C(1)-C(2)	1.469(5)		
O(1)-Co-O(2)	79.54(10)	O(1)-Co-N(1)	168.15(11)
O(1)-Co-N(2)	107.86(12)	O(1)-Co-N(3)	105.27(13)
O(1)-Co-N(4)	98.61(12)	O(2)-Co-N(1)	88.91(12)
O(2)-Co-N(2)	169.57(13)	O(2)-Co-N(3)	90.28(12)
O(2)-Co-N(4)	88.14(12)	N(3)-Co-N(4)	155.37(13)
plane 1[a]	plane 2[a]	75.99(12)	

[a]plane 1, benzene ring of catecholate moiety; plane 2, anthracene moiety.

3-2-2. Magnetic properties of cobalt complexes

The temperature dependence of the $\chi_{mol}T$ product for powder samples of complexes **3-6** are shown in Figure 3-6. Complex **3** is diamagnetic in the entire temperature range (4.5—400 K). The magnetic behavior of complex **4** is similar to that of complex **3**, except for the slight increase of $\chi_{mol}T$ values from 0.06 emu K mol^{-1} at 300 K to 0.09 emu K mol^{-1} at 400 K (Fig. 4,

inset), which is indicative of the valence tautomerism.

In complex **5**, the $\chi_{mol}T$ value is 0.68 emu K mol^{-1} at 50 K and increases gradually to 1.1 emu K mol^{-1} at 400 K. This finding suggests the valence tautomerism from Co^{III}(LS)-Cat to Co^{II}(HS)-SQ species. The $\chi_{mol}T$ value of **5** at 4.5 K (0.40 emu K mol^{-1}) shows that complex **5** is a mixture of the paramagnetic Co^{II}(HS)-SQ and the valence tautomeric Co^{III}(LS)-Cat species, which is consistent with the IR data. This behavior could be caused by the presence of geometrical isomers: four isomers are possible for **4** and **5** as described later. A dinuclear cobalt complex with a bis(dioxolene) ligand and two Me_2TPA ligands shows similar magnetic behavior, which is attributable to the weak intermolecular cooperativity.[53] In complex **6**, the $\chi_{mol}T$ value is 3.0 emu Kmol^{-1} at 400 K, which is expected for typical Co^{II}(HS)-SQ species.[52(a)] The value decreases to 1.7 emu K mol^{-1} due to the depopulation of the excited multiplets that are split by the combination of spin-orbit coupling and low-symmetry distortion.

The effect of Me_nTPA on the magnetic properties of **3**-**6** are similar to that of [Co(Me_nTPA)(diox)]PF_6 (diox = 3,5-di-*tert*-butyl-1,2-dioxolene): Co^{II}(HS)-SQ is preferred with the increase of the methyl group on TPA.[23] However, the $\chi_{mol}T$ value of **5** at low temperature is larger than that of [Co(Me_2TPA)(diox)]PF_6, because the paramagnetic Co^{II}(HS)-SQ species that exhibits no VT exists as a minor component in **5**. Presumably, *n*-hexane molecules as crystal solvents affect the intermolecular interaction. In the case of [Co(Me_2TPA)(diox)]PF_6, higher conversion was found in the toluene solvate compared with the ethanol solvate.[54]

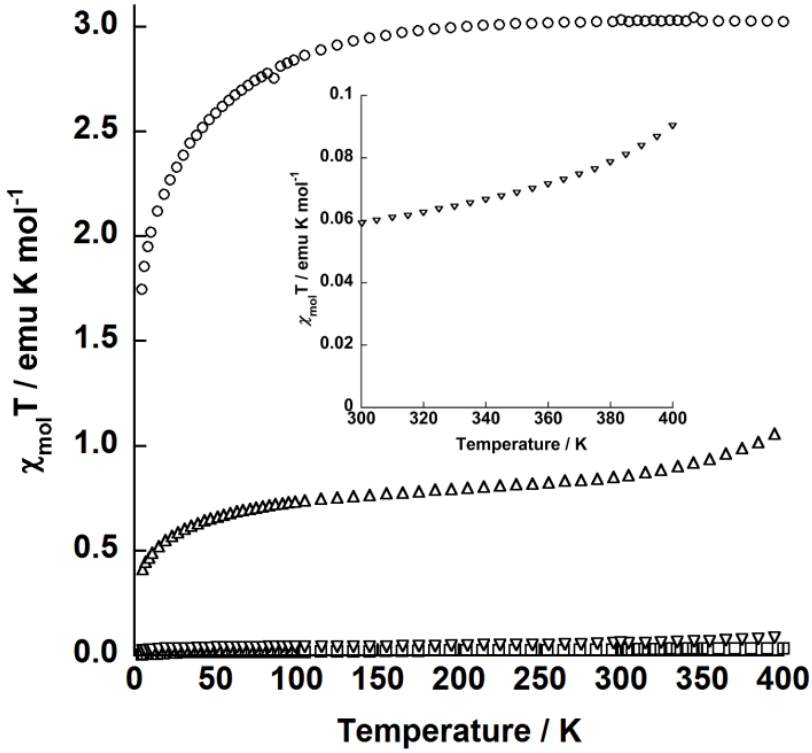

Figure 3-6. Temperature dependence of molar magnetic susceptibilities for complexes **3** (□), **4** (▽), **5** (△), and **6** (○).

The LIVT experiments were performed on powder samples of complexes **3-5** by light irradiation at λ = 355 and 532 nm. The photo-irradiation was carried out at 5 K. The magnetic susceptibility did not change with photo-irradiation of **3**, while slight changes in magnetic susceptibilities were observed in **4** and **5** for both 355 and 532 nm irradiation, which indicates the occurrence of LIVT with low conversion (Figure 3-7). The formation of the Co^{II}(HS)-SQ species by 355 nm light, which is in the anthracene $\pi\pi^*$ transition region, suggests the antenna effect of the anthracene moiety. The excitation by using 532 nm light, which is in the MLCT region, may cause a reverse LIESST effect, leading to low efficiency of LIVT.[23]

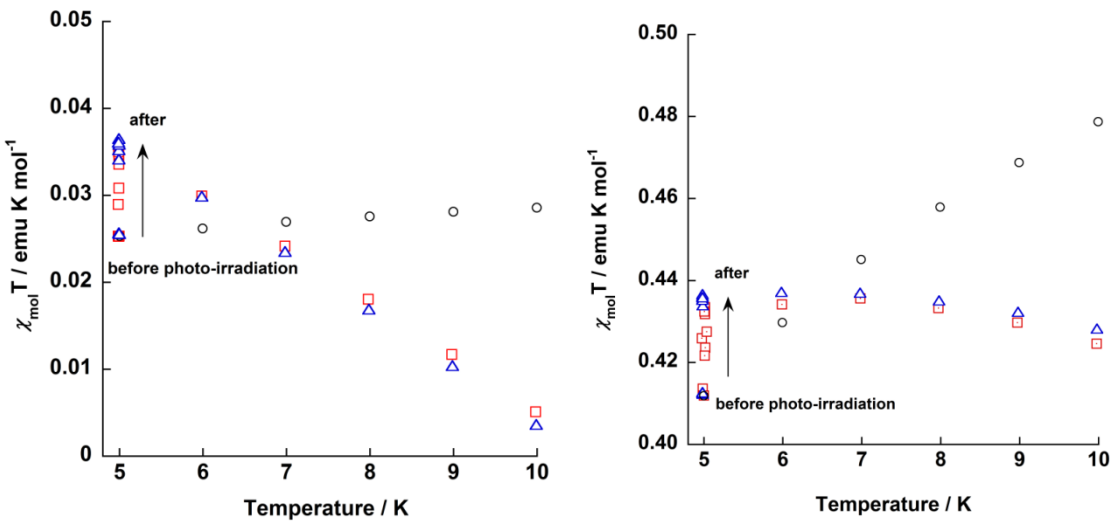

Figure 3-7 Temperature dependence of magnetic susceptibilities of complexes **4** (left) and **5** (right), the bulk powder sample (○), after irradiation with 355 nm light (□) and 532 nm light (△). The χ_MT values of the thin samples at 5 K before photo-irradiation were corrected by using that of the bulk powder sample at 5 K. The values after photo-irradiation are lower than those of the bulk powder sample above 7 K, because the susceptibility data were not corrected for the diamagnetism of the tape.

To investigate the excited states of the anthracene-functionalized cobalt complexes, we attempted TRESR spectroscopy for **3** and **6** diluted in a frozen BuCN matrix using the irradiation of 355 nm ns-pulsed LASER. However, TRESR spectra were not observed. On the other hand, a weak TRESR spectrum of H_2L diluted in a frozen 2-Me-THF matrix was observed 0.5 μs after nano-second pulsed laser excitation by 355 nm light (Figure 3-8). The spectral pattern is coincident with an excited triplet state.[6] Probably, in complexes **3** and **6**, the excited state undergoes rapid energy relaxation to the ground state or spin-lattice relaxation. Sorace *et al.* reported that [Co(TPA)(diox)]PF_6 (diox = 3,5-di-*tert*-butyl-1,2-dioxolene) showed the photoinduction of the Co^{II}(HS)-SQ form and fast relaxation to Co^{III}(LS)-Cat.[23]

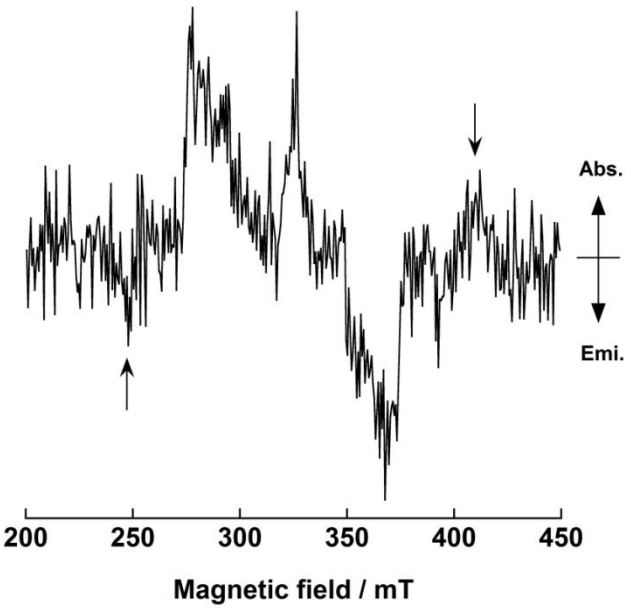

Figure 3-8. TRESR spectrum of H_2L^3 at 30 K in a 2-Me-THF glass matrix at 0.5 μs. "Abs." and "Emi." denote the absorption and emission of microwave. The signals were observed in the range of 250 to 420 mT. The deduced *D* value is about 0.07 cm^{-1}, which is similar to that of anthracene (0.0710 cm^{-1}).

3-2-3. Dynamic behavior of complexes 3 and 4 in CD_3CN solution.

The ^{1}H NMR spectrum of complex **3** in acetonitrile-d_3 at 273 K shows the presence of two geometrical isomers in a 1 : 0.9 ratio (Figure 3-9). As shown in Figure 3-10, the O atom in para-position to the 9-anthracenyl group occupies *trans*-position (**A**) or *cis*-position (**B**) to the central amine nitrogen of TPA. In the crystal structure of **6**, one isomer corresponding to **A** was observed (vide supra). The temperature dependence of ^{1}H NMR spectra of **3** shows an equilibrium between two geometrical isomers **A** and **B**. The signals are significantly broadened above 300 K. Two signals of 10-H proton of the anthracene ring (8.48 and 8.41 ppm) coalesced at 313 K. Four signals due to the 6-positions of pyridyl groups were observed at 9.37, 9.28, 8.62, and 8.58ppm at 253 K. At 313 K, the former two signals disappear, and the latter two signals, corresponding to **A** and **B**, are merged. These four pyridyl signals of 6-positon for the two isomers appeared at 8.88 ppm as a broad signal at 343 K. These results indicate that not only

flipping of the catecholate ligand $\mathbf{L^3}$ but also the interchange between the pyridyl groups of TPA and $\mathbf{L^3}$ occurs in the isomerization. Band-shape analysis of the 10-H proton of the anthracene ring was performed. The activation thermodynamic parameters for the isomerization were determined from an Eyring plot of the best-fit rate constants *versus* $1/T$: $\Delta H^{\ddagger} = 74 \pm 2$ kJ mol^{-1} and $\Delta S^{\ddagger} = 27 \pm 1$ J mol^{-1}K^{-1} (Figure 3-11).

Figure 3-10 shows a plausible mechanism of the isomerization. In isomer **A**, dissociation of one catecholate O atom provides a vacant coordination site. If the other catecholate O atom migrates to the vacant site, isomer **B** is formed by recoordination of the dissociated O atom. An alternative process is migration of the pyridine N atom of TPA to the vacant site *cis* to the central amine nitrogen of TPA, forming **A**. Dissociation of bidentate ligands such as 1-methyl-3-(2-naphthyl)propane-1,3-dinato and hydroxymate was reported for cobalt(III) TPA complexes.[55]

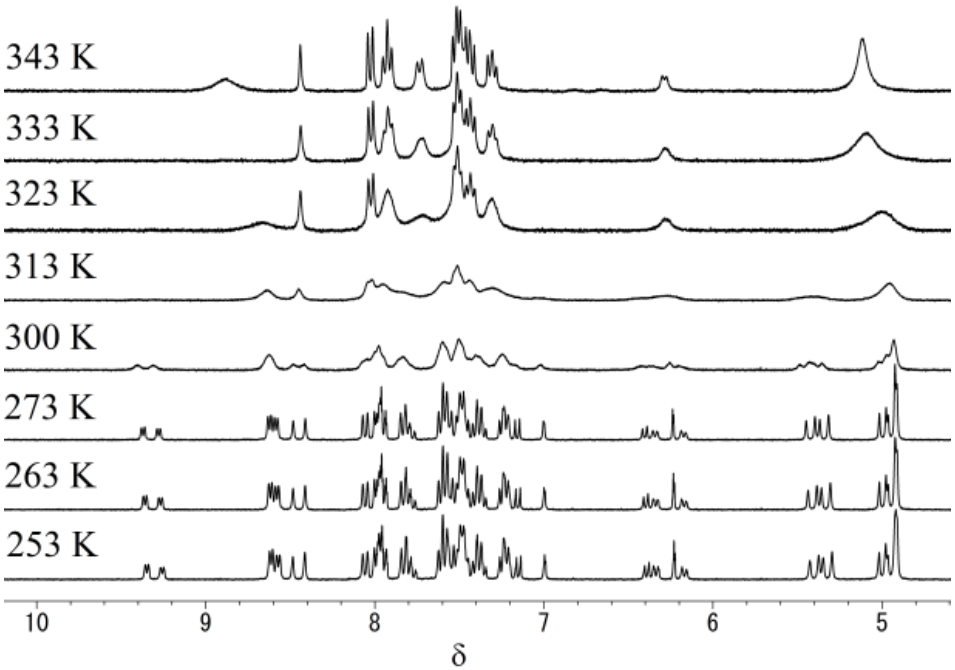

Figure 3-9. Temperature dependence of ^{1}H NMR spectra of complex **3** from 253 to 343 K in acetonitrile-d_3 (300 MHz).

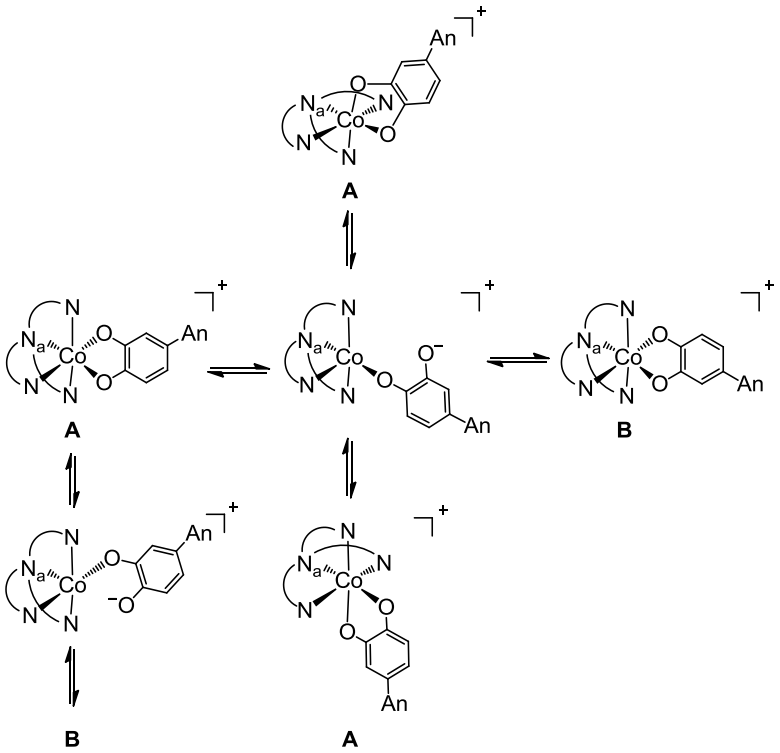

Figure 3-10. Isomerization of complex **3**: N_a = amine nitrogen of TPA, N = pyridine nitrogen of TPA, An = 9-anthracenyl group.

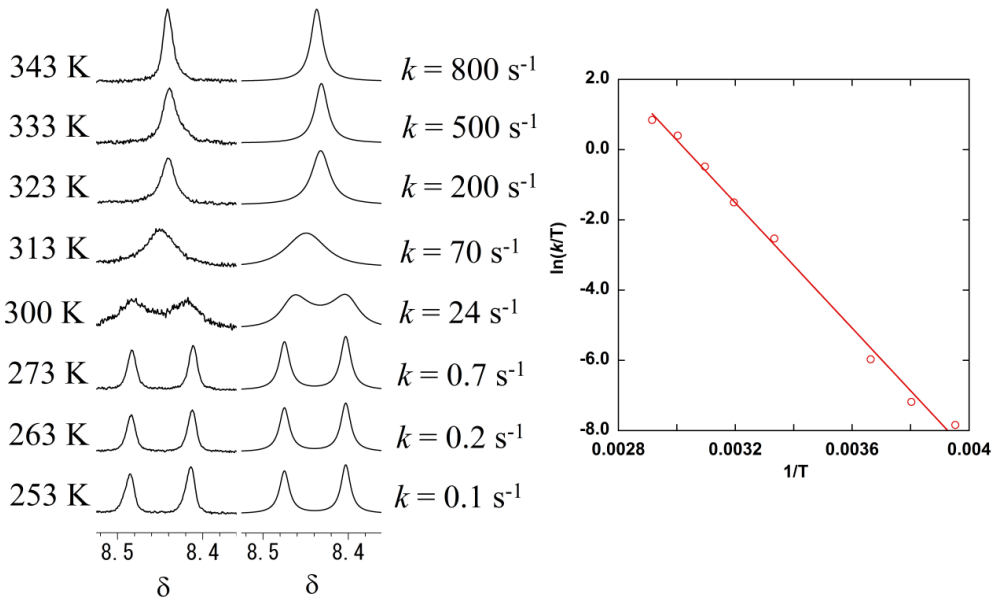

Figure 3-11. Observed (left) and simulated (middle) signals of 10-H proton of the anthracene ring in variable temperature ^{1}H NMR spectra of **1** in acetonitrile-d_3. Eyring plot of complex **1** (right): $\ln(k/T) = -\Delta H^{\ddagger}/(RT) + \ln(k_B/h) + \Delta S^{\ddagger}/R$; k, rate constant; T, temperature; R, gas constant; k_B, Boltzmann constant; h, Planck constant; $\Delta H^{\ddagger}$, activation enthalpy; $\Delta S^{\ddagger}$, activation entropy.

The dynamic behavior of complex **4** in acetonitrile-d_3 was also investigated by variable-temperature ^{1}H NMR spectroscopy (Figure 3-12). In **4**, four geometrical isomers **C**, **C'**, **D**, and **D'** (Figure 3-13) arise from the position of the 6-methyl-2-pyridyl group and the flipping of the catecholate ligand. Two isomers **C** and **D** were observed at 253 K in a 1 : 0.9 ratio, as evidenced by the two sets of two pyridyl 6-H signals at around 9.5 and 8.4 ppm: the latter are superimposed on the anthracene 10-H signals. Signals for MeTPA in **4** are significantly broadened at 300 K, and broad signals appear above 313 K, except for two methyl signals (2.98 and 2.94 ppm at 253 K). Signals for the catecholate ligand are gradually broadened as temperature increases, and the two anthracene 10-H signals coalesce at 333 K, which is higher than the coalescence temperature for **3**. The behavior of the anthracene-catecholate ligand is clearly different from that of the MeTPA ligand. The broadening at 300 K is probably due to the isomerization between **C** and **C'** (**D** and **D'**) without flipping motion of the catecholate ligand. The thermodynamic parameters were determined from the band-shape analysis of the signals of 10-H proton of anthracene ring: $\Delta H^{\ddagger}$ = 94 ± 3 kJ mol^{-1}K^{-1} and $\Delta S^{\ddagger}$ = 72 ± 9 J mol^{-1}K^{-1} (Figure 3-14).

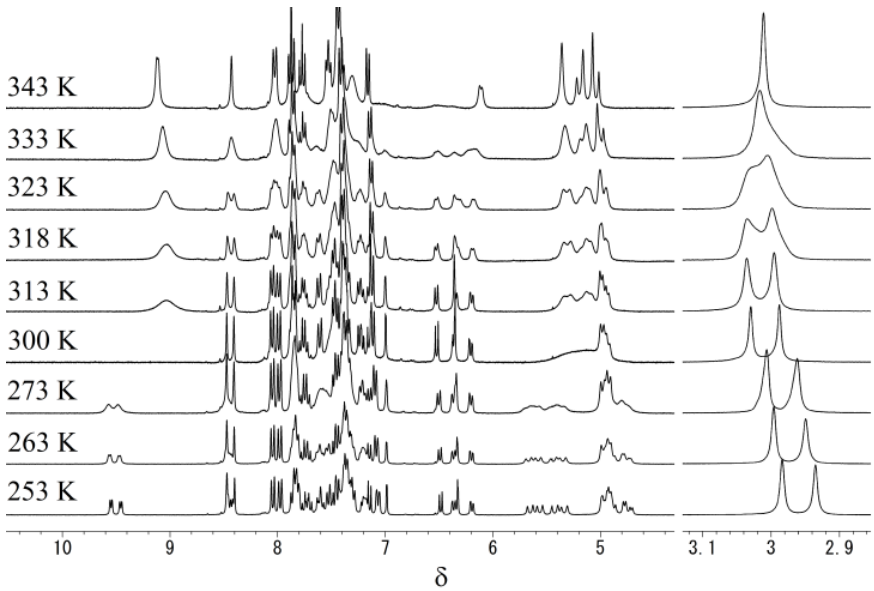

Figure 3-12. Temperature dependence of ^{1}H NMR spectra of complex **4** from 253 to 343 K in acetonitrile-d_3 (300 MHz).

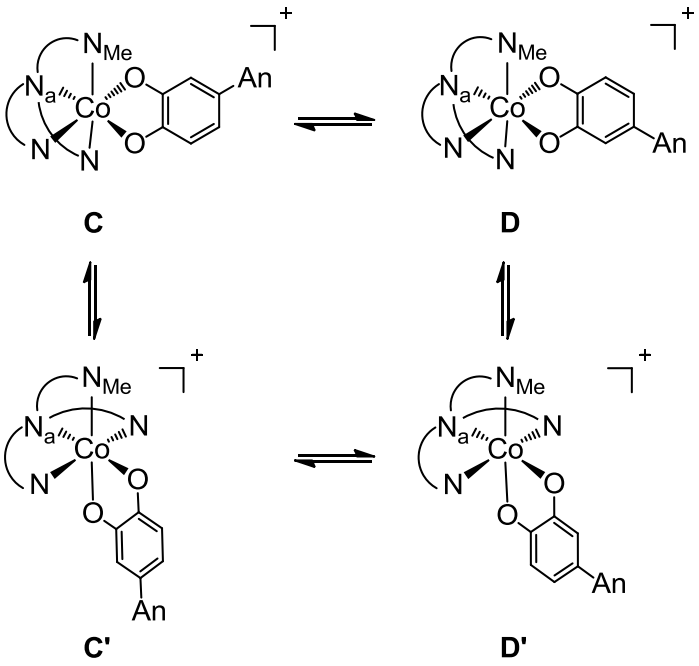

Figure 3-13. Isomerization of complex **4**: (N_a = amine nitrogen of MeTPA, N_{Me} = pyridine nitrogen with a Me group, N = pyridine nitrogen, and An = 9-anthracenyl group).

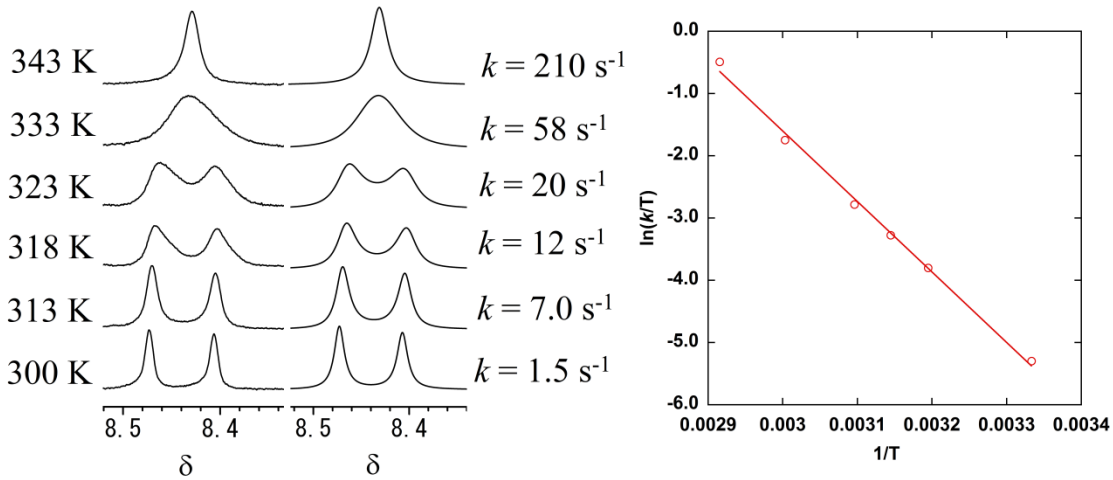

Figure 3-14. Observed (left) and simulated (middle) signals of 10-H proton of the anthracene ring in variable temperature ^{1}H NMR spectra of **4** in acetonitrile-d_3. Eyring plot of complex **4** (right): $\ln(k/T) = -\Delta H^{\ddagger}/(RT) + \ln(k_B/h) + \Delta S^{\ddagger}/R$; k, rate constant; T, temperature; R, gas constant; k_B, Boltzmann constant; h, Planck constant; $\Delta H^{\ddagger}$, activation enthalpy; $\Delta S^{\ddagger}$, activation entropy.

The data obtained from the band-shape analyses in **3** and **4** indicate that the isomers are in equilibrium at room temperature in solution. The energy barrier for the isomerization between **C** and **D** in **4** is larger than that between **A** and **B** in **3**. The large energy barrier in **4** can be attributed to the steric interactions between the methyl group on MeTPA and the catecholate ligand. A larger energy barrier for the flipping motion of the catecholate ligand is expected in **5** and **6**. The variable-temperature ^{1}H NMR spectra of **5**, however, did not show clear signals of the anthracene ring because of the presence of the paramagnetic Co^{II}-SQ form, which can be interconverted to the diamagnetic Co^{III}-Cat form (Figure 3-15). The variable-temperature experiments of **6** suggested that the paramagnetic Co^{II}-SQ form is also dominant in solution (Figure 3-16).

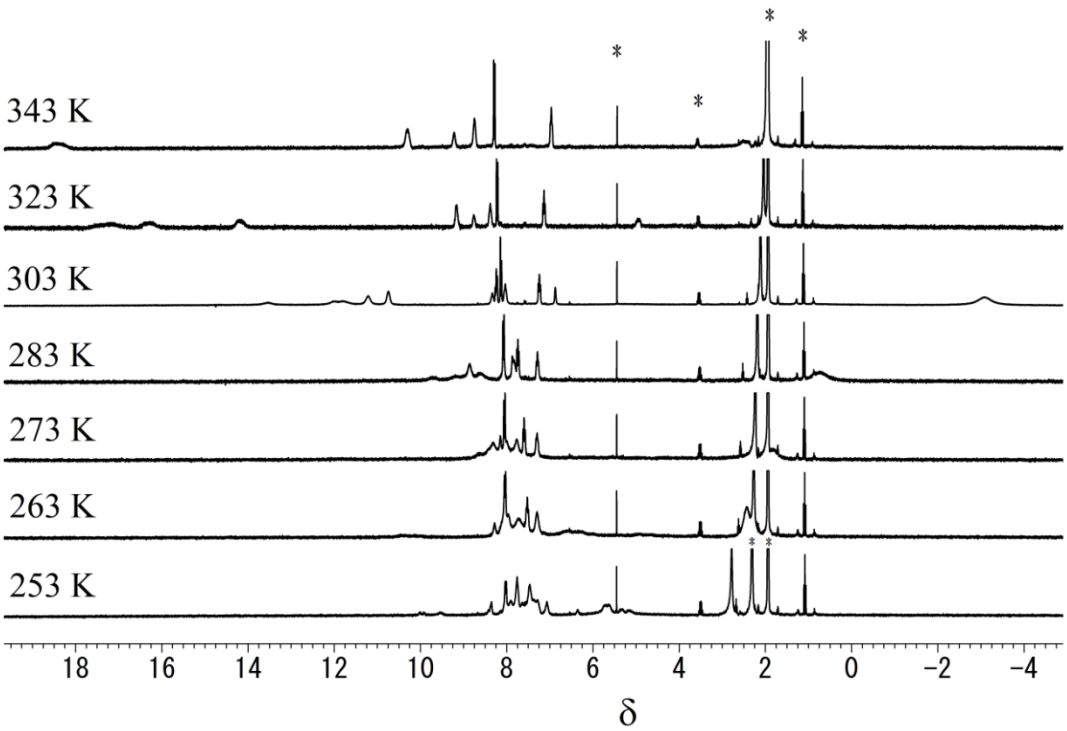

Figure 3-15. Variable temperature ^{1}H NMR spectra (300 MHz) of complex **5** in acetonitrile-d_3. Residual solvent signals are marked with an asterisk.

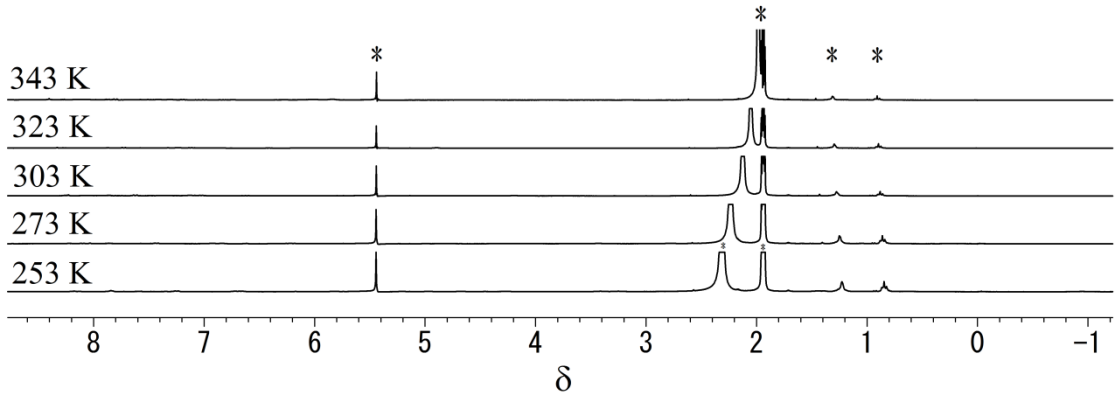

Figure 3-16. Variable temperature ^{1}H NMR spectra (300 MHz) of complex **6** in acetonitrile-d_3. Residual solvent signals are marked with an asterisk.

3-3. Conclusion

The author reported the syntheses and the magnetic behavior of a series of cobalt complexes **3**-**6** with tripodal ligands and the redox-active ligand, which consists of catecholate and anthracene moieties. In the solid state, complex **3** is diamagnetic and complex **6** is paramagnetic in the range 4.5—400 K. In complexes **4** and **5**, increase of the $\chi_M T$ value was observed at the high temperature regions, indicating the occurrence of valence tautomerism. Photo-magnetic measurements and TRESR measurements were conducted to confirm the effect of anthracene moiety. In the photo-magnetic measurements, complexes **4** and **5** showed LIVT with low conversion, and the antenna effect of the anthracene moiety was observed. $\mathbf{H_2L^3}$ showed TRESR signals, while no signal was observed in the TRESR measurements for **3** and **6**. Probably, the Co^{II}(HS)-SQ species formed by photo-irradiation undergo rapid energy relaxation to the ground state or spin-lattice relaxation. In solution, ^{1}H NMR and UV-vis spectra indicate the existence of Co^{III}(LS)-Cat species for **3** and **4**, while Co^{II}(HS)-SQ species for **5** and **6**. In the temperature dependence of ^{1}H NMR spectra of **3** and **4**, the equilibrium between the two or four geometrical isomers was observed. The results indicate that the isomerism of the low-spin

cobalt(III) TPA-catecholate complexes is induced by Co-O (catecholate) bond cleavage. The cobalt complexes with an anthracene-containing dioxolene ligand can be used for the fluorescence switching system. In chapter 4, the author reports the synthesis and fluorescence behavior of the π-spin system composed of cobalt complex, anthracene, and BODIPY moieties.

Chapter 4

Synthesis and Fluorescence Behavior of Cobalt Complexes with a Dioxolene Ligand Containing an Anthracene-BODIPY Unit

4-1. Introduction

In Chapter 3, the author reported the cobalt complexes with an anthracene-functionalized dioxolene ligand [Co(**L**^{3})(Me$_n$TPA)]PF$_6$ (*n*= 0, **3**; *n* = 1, **4**; *n* = 2, **5**; *n* = 3, **6**). The spin states of the cobalt center were successfully controlled by the number of Me groups on the pyridine moiety. In this chapter, the author describes the attempt to develop the fluorescence switching system, where a BODIPY unit is introduced as a florescence moiety to the anthracene moiety of [Co(**L**^{3})(Me$_n$TPA)]PF$_6$ as mentioned in section 1-5-2.

BODIPY derivatives with 9-anthracenyl group exhibit high energy transfer efficiency from the anthracene moiety in the excited singlet state to the BODIPY moiety (Figure 4-1(a)).[35] When a radical moiety is introduced to the anthracene-BODIPY compounds, the decrease of energy transfer efficiency is caused by spin-orbit intersystem crossing (Figure 4-1 (b)).[30(a)] In this chapter, the catechol-anthracene-BODIPY ligand precursor **H$_2$L^4** (Figure 4-1 (c)) was used for the synthesis of cobalt complexes [Co(**L**^{4})(Me$_n$TPA)]PF$_6$ (*n* = 0, **7**; *n* = 2, **8**; *n* = 3, **9**) (Figure 4-2), in which the catecholate cobalt(III) or semiquinonate cobalt(II) center are formed. The decrease of energy transfer from anthracene to BODIPY, which leads to fluorescence quenching, is expected for the Co(II)-SQ form because of the competitive spin-orbit intersystem crossing as reported for the radical-anthracene system.[6,30(a)] In order to confirm the hypothesis, the author synthesized the Co(III)-Cat and Co(II)-SQ complexes containing an anthracene-BODIPY unit, and elucidated their electronic properties and the fluorescence behavior.

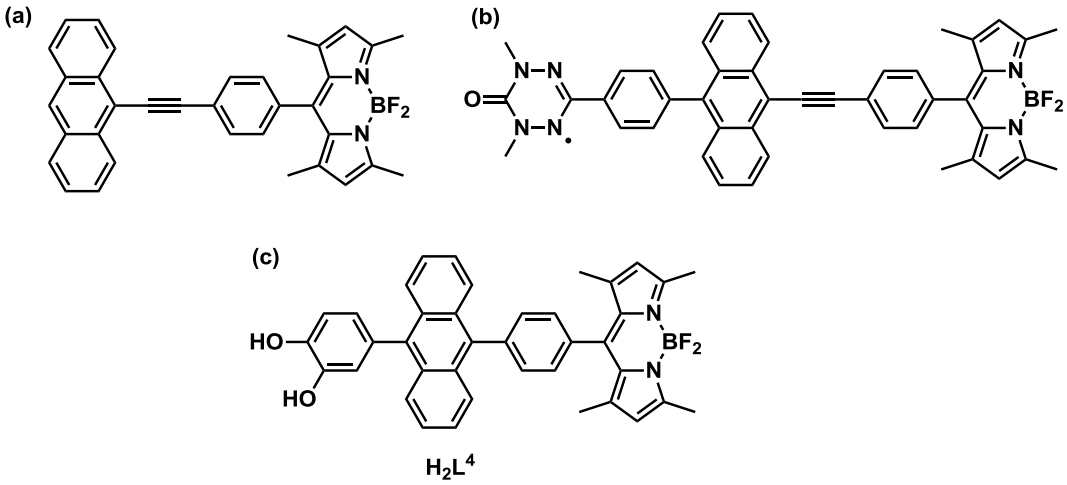

Figure 4-1. Molecular structures of anthracene-BODIPY cassettes; (a) simple cassette, (b) π-radical spin system, (c) $\mathbf{H_2L^4}$

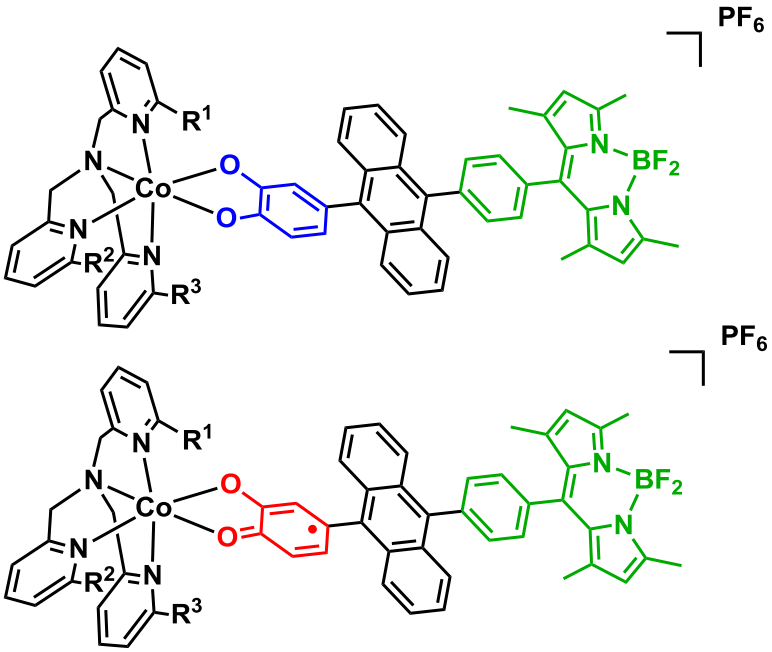

Figure 4-2. Molecular structures of cobalt complexes [Co($\mathbf{L^4}$)(Me$_n$TPA)PF$_6$ (n = 0, **7**; n = **2**, **8**; n = **9**); (top) Co(III)-Cat form, (bottom) Co(II)-SQ form.

4-2. Results and discussion

4-2-1. Synthesis and structure of a BODIPY-anthracene-dioxolene ligand precursor H_2L^4

Ligand precursor $\mathbf{H_2L^4}$ was synthesized according to Scheme 4-1, and characterized by IR, NMR spectroscopy, and elemental analysis.

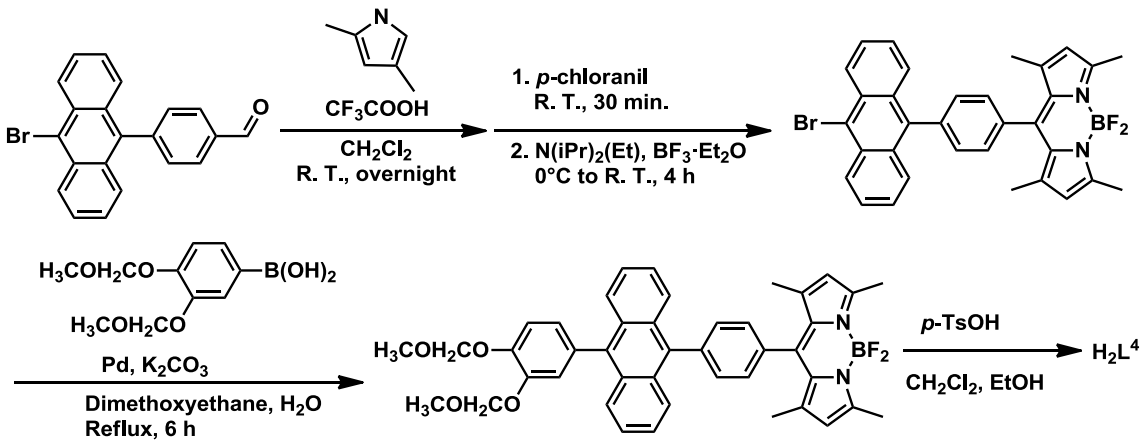

Scheme 4-1. Synthesis of $\mathbf{H_2L^4}$

Figure 4-3 shows ^{1}H and ^{19}F NMR spectra of $\mathbf{H_2L^4}$ in $CDCl_3$. The signals of H atoms at 2,6-positions on the pyrrole rings were observed at 6.08 ppm. The Me protons appeared as two singlets at 2.71 and 1.72 ppm. These features are in agreement with those of other BODIPY derivatives.[56] The broad signals of OH groups were observed around 5.5–5.6 ppm. The signals at 7.11–6.93 ppm were assigned to aryl protons of the catechol moiety. The ^{19}F NMR spectrum of $\mathbf{H_2L^4}$ shows a signal at -146 ppm.

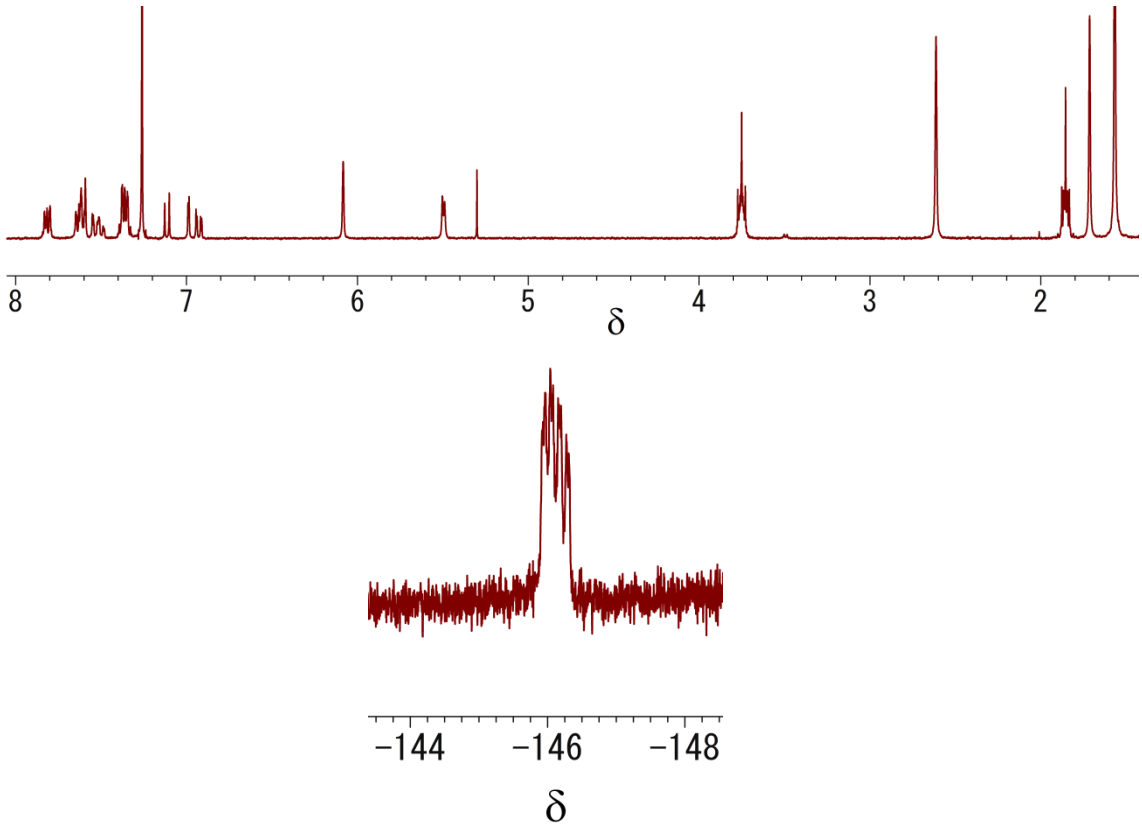

Figure 4-3. (Top) ^{1}H NMR spectrum of $\mathbf{H_2L^4}$ in $CDCl_3$ (300 MHz), (Bottom) ^{19}F NMR spectrum of $\mathbf{H_2L^4}$ (282.4 MHz).

The crystal structure of $\mathbf{H_2L^4}$ was determined by a single crystal X-ray structure analysis. Figure 4-4 shows an ORTEP drawing of $\mathbf{H_2L^4}$. Selected bond lengths, angles and dihedral angles are listed in Table 4-1. One of two hydroxyl groups of the catechol moiety was disordered over two sites and refined with equal occupancy factors of 0.5. The bond lengths and angles are similar to those of other BODIPY derivatives.[57] The four planar moieties are twisted along the pseudo two-fold axis of the molecule: torsion angles; BODIPY and the adjacent phenyl ring, 90.4(4)°; anthracene and the phenyl ring, 67.7(4)°; anthracene and catechol, 75.6(4)°. A similar twisted structure was reported for *p*-phenyl-linked anthracene-BODIPY compound.[58]

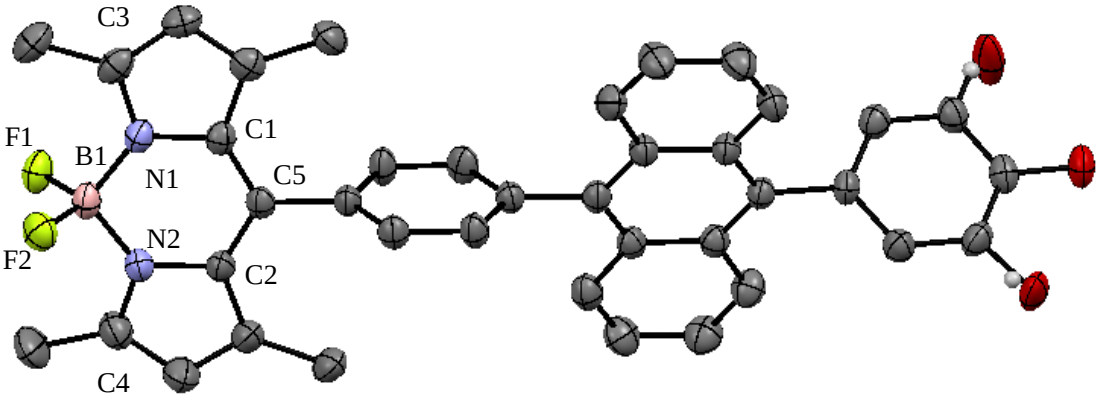

Figure 4-4. ORTEP drawing of the $\mathbf{H_2L^4}$. Hydrogem atoms (except hydrogen atoms of hydroxyl group) are omitted for clarity.

Table 4-1. Selected bond lengths (Å), angles (deg) and dihedral angle (deg) of $\mathbf{H_2L^4}$

B1-F1	1.408(4)	N1-C1	1.401(4)
B1-F2	1.391(5)	N1-C3	1.353(4)
B1-N1	1.532(5)	N2-C2	1.404(4)
B1-N2	1.528(5)	N2-C4	1.354(4)
C5-C1	1.398(4)	C5-C2	1.390(4)
N1-B1-N2	108.0(3)	N2-B1-F1	110.0(3)
N1-B1-F1	109.7(3)	N2-B1-F2	110.5(3)
N1-B1-F2	110.3(3)	F1-B1-F2	108.4(3)
Plane 1[a]	Plane 2[a]	90.4(4)	
Plane 2[a]	Plane 3[a]	67.7(4)	
Plane 3[a]	Plane 4[a]	75.6(4)	

[a]Plane 1, BODIPY moiety; plane 2, phenyl moiety; plane 3, anthracene moiety; plane 4, catecholate moiety.

4-2-2. Synthesis and properties of cobalt complexes

Cobalt complexes **7**–**9** were synthesized according to Scheme 4-2. The reaction of cobalt(II) dichloride with $\mathbf{H_2L^4}$ and TPA or Me_nTPA ligands gave the corresponding complexes by aerobic oxidation.

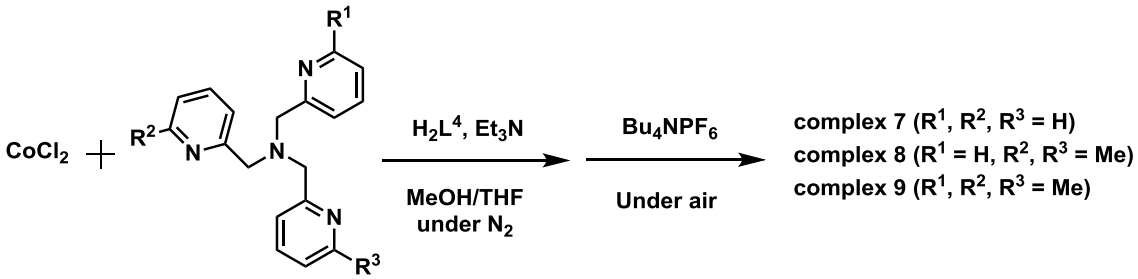

Scheme 4-2. The synthesis of cobalt complexes **7**–**9**.

The charge distributions of the dioxolene ligand were investigated on the basis of the different frequencies of C-O and C=C stretching modes. Figure 4-5 shows the IR spectra of $\mathbf{H_2L^4}$ and complexes **7**–**9**. The IR spectrum of **7** shows the characteristic bands of catecholate form assigned to the skeletal dioxolene at 1255 and 1490 cm^{-1}. In complex **9**, the absence of the signal around 1250 cm^{-1}, and the new bands at 1468 cm^{-1} attributable to the C=C stretching mode of semiquinonate form were observed. Complex **8** shows the characteristic bands of catecholate form at 1258 cm^{-1}, however the intensity of the bands is lower than that of **7** as a standard of the bands derived from BODIPY-dioxolene ligand at 1308 cm^{-1}. In addition, the band derived from semiquinonate form at 1469 cm^{-1} was observed. These data suggest that complex **8** is a mixture of the Co(II) and Co(III) species. The spectral features of complexes **7**–**9** in the solid state are also in accordance with those of complexes **3**, **5**, and **6**, respectively.

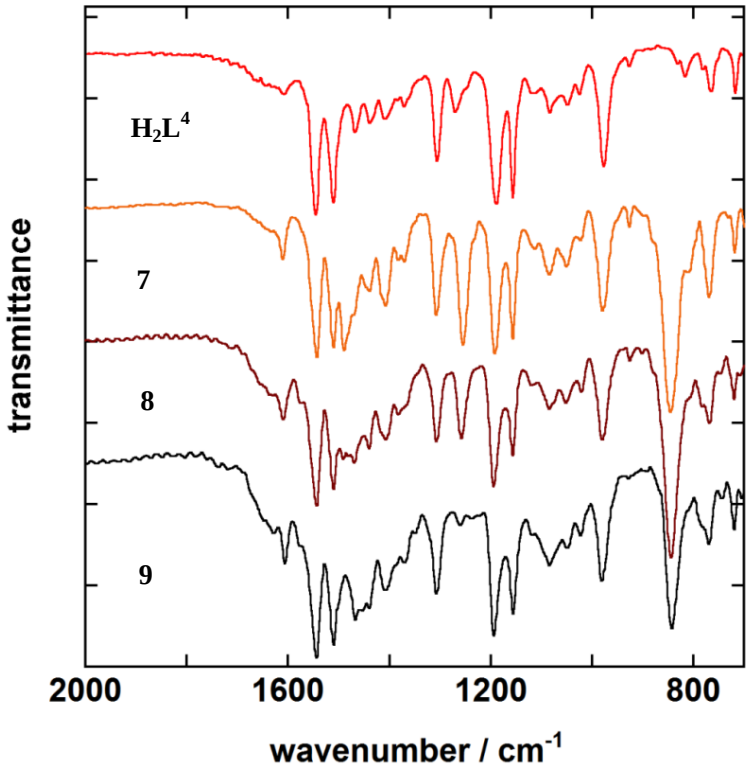

Figure 4-5. IR spectra of $\mathbf{H_2L^4}$ and complexes **7**-**9** at room temperature.

4-2-3. Electrochemistry of $\mathbf{H_2L^4}$ and complexes 3 and 7

To investigate the influence of the introduced BODIPY moiety, cyclic voltammetry was carried out in CH_3CN at room temperature (Figure 4-6). The electrochemical data of $\mathbf{H_2L^4}$ and Co(III) catecholate complexes **3** and **7** are summarized in Table 4-2. $\mathbf{H_2L^4}$ and complex **7** show a reversible redox couple at -1.55 V vs $E°'(Fc^+/Fc)$, which is assigned to $BODIPY^{0/1-}$. Phenyl-BODIPY and dimethyl-phenyl-BODIPY exhibit the redox couples at -1.57[58] and -1.56[56] V vs $E°'(Fc^+/Fc)$ in CH_3CN, respectively. The origin of the cathodic peaks at -1.31 V in $\mathbf{H_2L^4}$ and -1.33 V in **7** is unclear. Complex **7** shows variation in the peak separation with increasing scan rate (Figure 4-7 (left)). The behavior is usually observed in a reduction process from Co^{III} to Co^{II}.[50] In complex **7**, the reduction is assigned to the reduction from Co^{III} to Co^{II}. The analogous behavior is also observed in complex **3** (Figure 4-10 (right)), and the reduction peak

potential of **3** is slightly shifted to a more positive value (0.02 V) compared with **7**. Complexes **3** and **7** show reversible redox couples at 0.092 V and 0.105 V, respectively (Figure 4-8), which are assignable to the oxidation of catecholate moiety. The positive shift of the oxidation potential from 0.092 to 0.105 V is ascribable to the expansion of π-conjugation by the introduction of phenyl-BODIPY moiety. Probable assignment of the anodic wave at around 0.85 V in all compounds is the further oxidation of coordination moiety and/or anthracene moiety.[50,58]

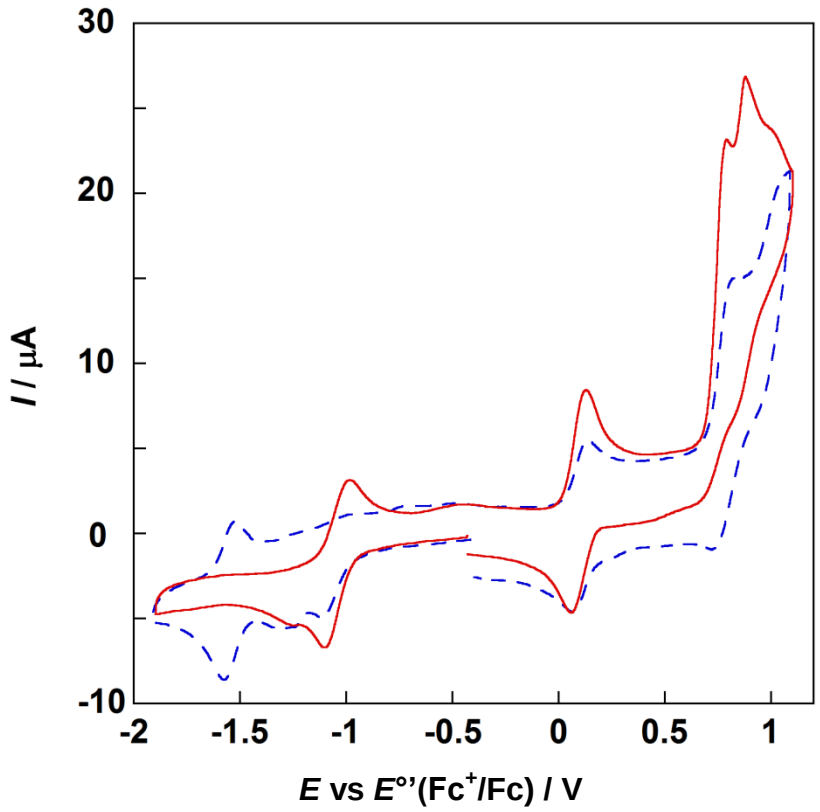

Figure 4-6. Cyclic voltammograms of complexes **7** (– –) and **3** (—) in CH_3CN containing 0.10 M Bu_4NPF_6 recorded at a scan rate of 100 mV s^{-1}: working electrode, glassy carbon; auxiliary electrode, platinum wire; reference electrode, Ag/Ag^+. Potentials are versus ferrocenium/ferrocene (Fc^+/Fc).

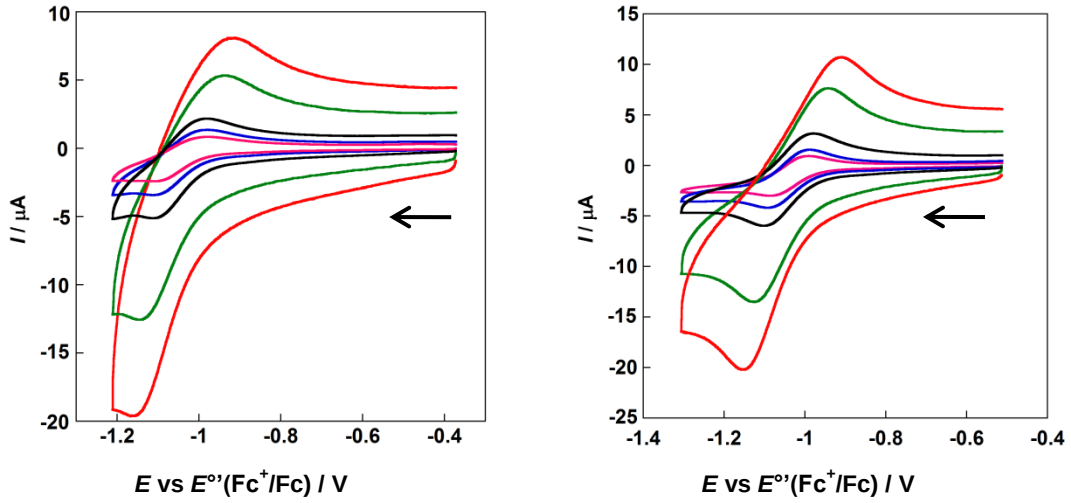

Figure 4-7. The reduction processes of complexes **7** (left) and **3** (right) in CH_3CN containing 0.10 M Bu_4NPF_6 recorded at scan rates of 25 (—), 50 (—), 100 (—), 500 (—), and 1000 (—) mV s^{-1}: working electrode, glassy carbon; auxiliary electrode, platinum wire; reference electrode, Ag/Ag^+. Potentials are versus ferrocenium/ferrocene (Fc^+/Fc).

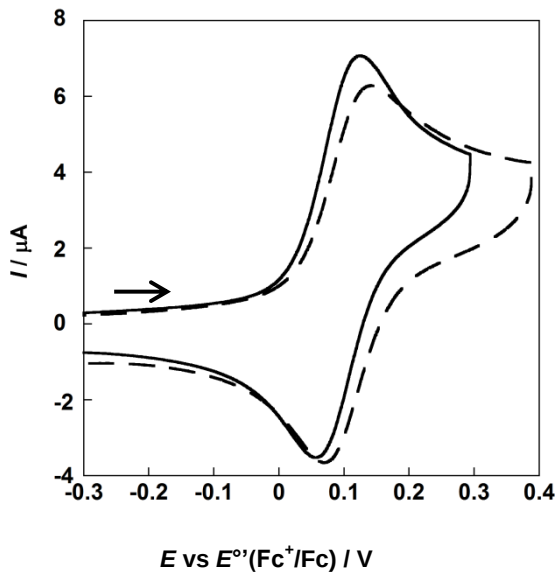

Figure 4-8. The oxidation processes of complexes **7** (– –) and **3** (—) in CH_3CN containing 0.10 M Bu_4NPF_6 recorded at a scan rate of 100 mV s^{-1}: working electrode, glassy carbon; auxiliary electrode, platinum wire; reference electrode, Ag/Ag^+. Potentials are versus ferrocenium/ferrocene (Fc^+/Fc).

Table 4-2. Electrochemical data for CH_3CN (0.1M Bu_4NPF_6) solutions of **H_2L^4**, **3** and **7**.[a]

	Oxidation	Oxidation	Reduction	Reduction	Reduction
	$E_{1/2}$/V(ΔE_p/mV)	E_{pa}/V	E_{pc}(ΔE_p/mV)	E_{pc}/V	$E_{1/2}$(ΔE_p/mV)
Complex **3**	0.092(70)	0.81, 0.88	-1.10(123)	—	—
Complex **7**	0.105(72)	0.82	-1.12(135)	-1.33	-1.55(65)
H_2L^4	—	0.83	—	-1.31	-1.55(63)

[a]All potentials were recorded at a scan rate of 100 mV s^{-1}: working electrode, glassy carbon; auxiliary electrode, platinum wire; reference electrode, Ag/Ag^+. Potentials are versus ferrocenium/ferrocene (Fc^+/Fc)

4-2-4. Spectroscopic properties of H_2L^4 and complexes 7 and 9

4-2-4-1. Spectroscopic properties of H_2L^4

The absorption spectra of **H_2L^4** measured in CH_3CN, CH_2Cl_2, toluene, and THF are shown in Figure 4-9(a). The photophysical data of **H_2L^4** are summarized in Table 4-3. An intense absorption band is centered at around 500 nm (ε = 85000 $M^{-1}cm^{-1}$ in CH_3CN), showing the narrow spectral band widths. Shoulder bands around 480 nm attributed to the 0-1 vibrational mode on the high-energy side. The lowest-lying S_0-S_1 transition is involved in the HOMO to LUMO transition.[56] As increasing solvent polarity from toluene to CH_3CN, the absorption maximum is slightly shifted from 504 to 497 nm, reflecting the ground-state stabilization in polar solvent. These spectral features are in accordance with other BODIPY derivatives.[56] In the emission spectra, **H_2L^4** shows the typical fluorescence behavior of BODIPY (Figure 4-9(b)). The mirror-image spectral shape to the absorption band indicates that the emission band is mainly ascribed to S_1-S_0 transition (Figure 4-10). The shorter-wavelength shift of emission maximum (toluene, λ_{em} = 515 nm; CH_3CN, λ_{em} = 509 nm) and the decrease of emission

quantum yield (Φ from 0.55 in toluene to 0.038 in CH_3CN at excitation wavelength 465 nm) as an increase in the solvent polarity were observed. The decrease of Φ in polar solvents is caused by electron transfer (ET) process from anthracene-catechol to BODIPY, and/or electron-phonon coupling with solvent phonons. These processes are known as the fluorescence quenching mechanism of BODIPY[56,59] and naphthalene-trialkylamine[60] compounds. The efficiency of energy transfer from anthracene to BODIPY in $\mathbf{H_2L^4}$ was estimated by comparison of the Φ values obtained by the exciting anthracene (350 nm) and BODIPY moieties (465 nm). The Φ value of $\mathbf{H_2L^4}$ within experimental error are almost independent of the excitation wavelength, irrespective of the solvent, indicating nearly complete energy transfer from the anthracene to BODIPY moieties. This is also supported by the fact that emission of the anthracene moiety is not observed in CH_2Cl_2 and CH_3CN (slight emission is observed in toluene) although $\mathbf{H_2L^3}$ shows emission (*vide infra*).

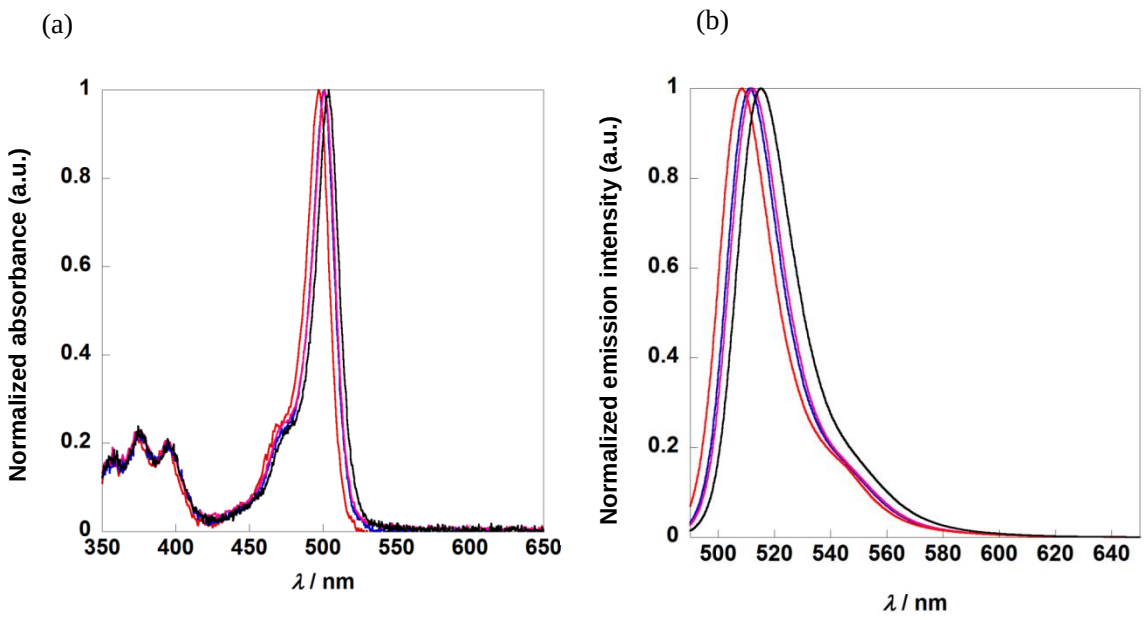

Figure 4-9. (a) Normalized absorption spectra of $\mathbf{H_2L^4}$ in several solutions: CH_3CN, (—); CH_2Cl_2, (—); toluene, (—); THF, (—). (b) Normalized emission spectra of $\mathbf{H_2L^4}$ in several solutions: CH_3CN, (—); CH_2Cl_2, (—); toluene, (—); THF, (—). Excitation wavelength = 470 nm.

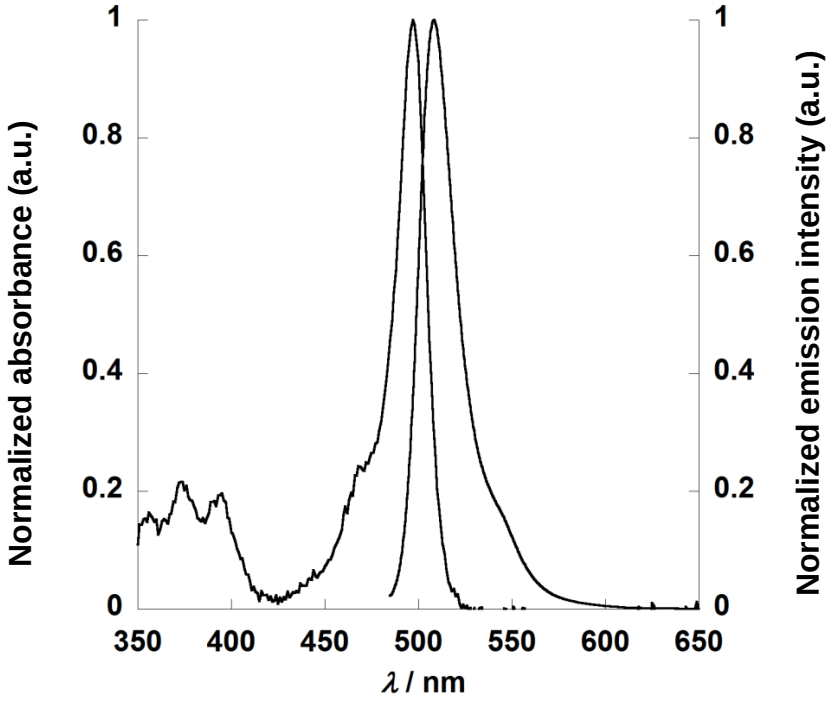

Figure 4-10. Normalized absorption and emission spectra of $\mathbf{H_2L^4}$ in CH_3CN.

Table 4-3. Photophysical properties of $\mathbf{H_2L^4}$, and complexes **7** and **9** in several solvents.

		λ_{abs} (max/nm)[a]	λ_{abs} (max/nm)[b]	λ_{em} (max/nm)	Φ_{ex350}[c]	Φ_{ex465}[c]
$\mathbf{H_2L^4}$	CH_3CN	374	497	509	0.030±0.006	0.038
	CH_2Cl_2	375	501	512	0.42±0.08	0.39
	Toluene	375	504	515 (435)[d]	0.57±0.07	0.55
	THF	375	501	511	—	—
Complex **7**	CH_3CN	373	497	509	0.003	0.005
Complex **9**	CH_3CN	373	497	509	0.020	0.027

[a]The anthracene moiety. [b]The BODIPY moiety. [c]The emission quantum yields were determined using fluorescein as a standard (Φ = 0.85 in carbonate-bicarbonate buffer at a pH of about 9.6)[61]
[d]Emission band was observed in toluene at excitation at 350 nm.

4-2-4-2. Spin states of complexes 7–9 in CH_3CN

Electronic absorption spectra of complexes **7**–**9** are shown in Figure 4-11. Absorption spectra of all complexes show the strong S_0-S_1 transition band of BODIPY at 497 nm with a shoulder band at 480 nm. Compared with complexes **3**, **5**, and **6**, nearly double ε of the ππ* absorption bands of the anthracene moiety are observed around 375 nm. The ππ* absorption bands are likely to be overlapped with the S_0-S_2 transition bands of BODIPY, since other aryl BODIPYs show the S_0-S_2 transition bands in the range of 300–400 nm.[35,59] Complex **7** shows the weak and broad absorption around 550–900 nm. The band is assigned to symmetry-forbidden LMCT transitions.[50] ^{1}H NMR signals of **7** appeared in the normal range, and the spectral patterns are similar to those of **3** except that the signals for BODIPY appeared at around 6.3, 2.3, and 1.8 ppm (Figure 4-12). These results indicate that complex **7** is a low-spin Co(III) catecholate complex. On the other hand, the absorption spectrum of **9** shows the band assigned to MLCT transitions.[52] In addition, the ^{1}H NMR signals of **9** were not observed in CD_3CN. These spectral features are consistent with that of high-spin Co(II) semiquinonate complexes. In complex **8**, LMCT band around 600–900 nm is observed, and the clear evidence for MLCT band is not observed. The ^{1}H NMR spectrum of **8**, however, indicates the existence of paramagnetic species (Figure 4-12). The complexes **7**–**9** show similar spectroscopic properties to those of **3**, **5** and **6**, respectively in solution, because the *p*-phenylene-linked BODIPY is apart from the cobalt center. Therefore, the spin states of **7**–**9** in solution are also controlled by the number of methyl groups on the pyridine.

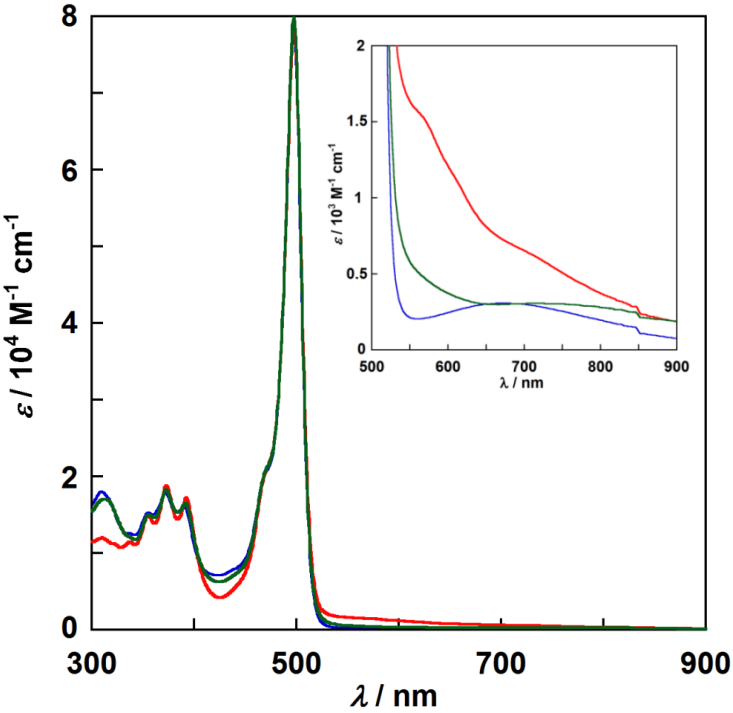

Figure 4-11. UV-vis absorption spectra of complexes **7** (—), **8** (—), and **9** (—) at room temperature in acetonitrile.

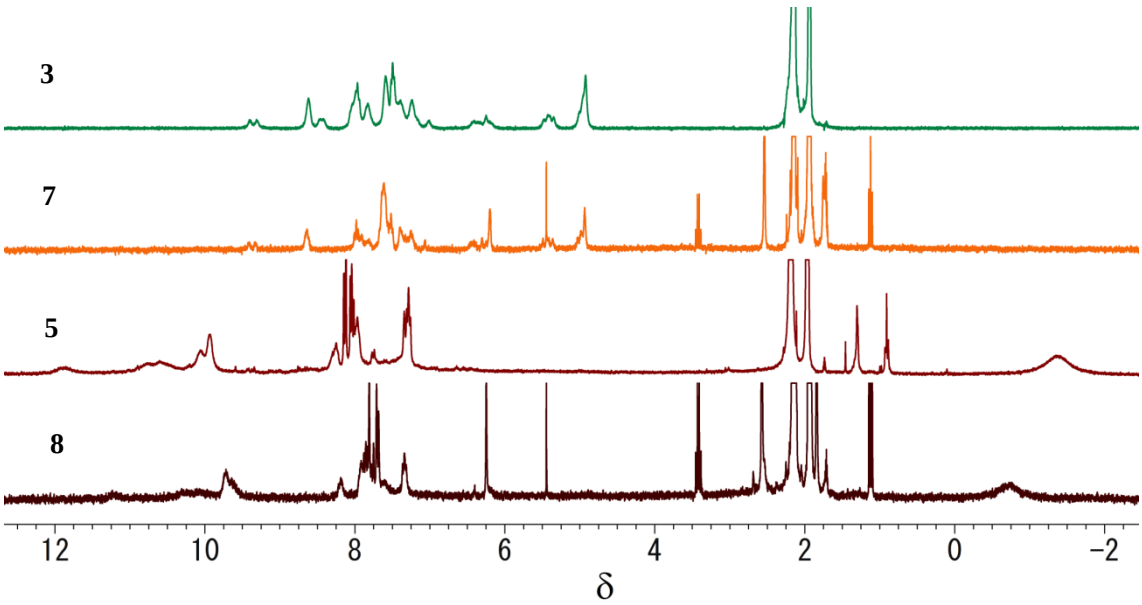

Figure 4-12. ^{1}H NMR spectra (300 MHz) of complexes **3**, **7**, **5** and **8** at room temperature in acetonitrile-d_3.

4-2-4-3. Fluorescence behavior of complexes 7 and 9

To investigate the influence of the spin states on fluorescence, low-spin cobalt(III) complexes **7** and high-spin cobalt(II) complex **9** were used. Figure 4-13 shows the emission spectra of $\mathbf{H_2L^4}$, **7**, and **9** at room temperature in CH_3CN chosen due to the solubility and the stability of these compounds. Light emission from complex **7** is highly quenched in comparison with those from $\mathbf{H_2L^4}$ and **9**. This tendency was also observed in CH_2Cl_2. The selective excitation of the BODIPY in **7** at 465 nm also showed similar fluorescence quenching. These results show divergence from the prediction mentioned in the introduction.

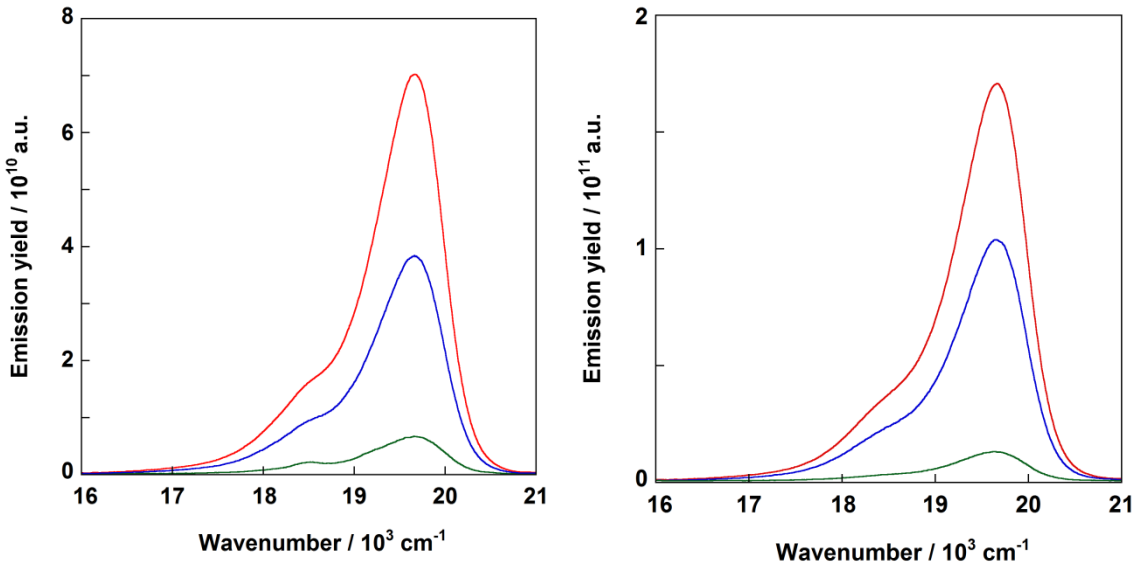

Figure 4-13. Emission spectra of $\mathbf{H_2L^4}$ (—), **7** (—), and **9** (—) in CH_3CN. The excitation wavelengths are (left) 350 nm and (right) 465 nm.

Generally, metal-ion binding to fluorophore results in the fluorescence quenching due to the enhanced nonradiative decay processes.[62] To investigate the effect of the coordination for nonradiative decay processes, the fluorescence measurements of complex **3** and $\mathbf{H_2L^3}$ were also performed (Figure 4-14). Compared with $\mathbf{H_2L^3}$, the fluorescence of **3** is quenched by a factor of 100.

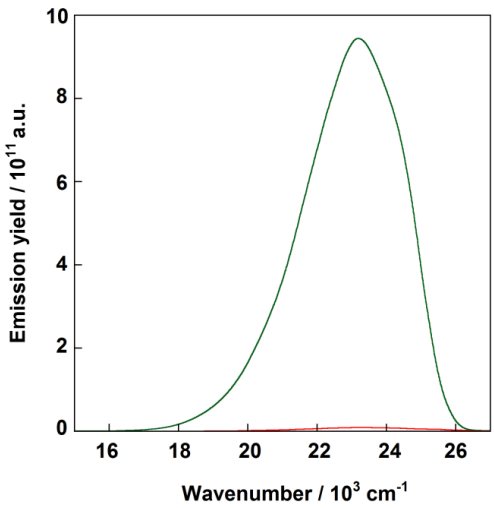

Figure 4-14. Emission spectra of $\mathbf{H_2L^3}$ (—), complex **3** (—) in 350 nm excitation wavelength. Solvent: CH_3CN.

Bartelmess *et al*. reported that *meso*-pyridyl BODIPY-cobaloxime complexes shows the fluorescence quenching, while the quenching is modest, when the binding ability of the ligand is weak.[63] Sorace *et al*. reported that the Co-O bond lengths of [$CoMe_3$TPA(3,5-di-*tert*-butyl-semiquinone)]PF_6 (2.022(7) and 2.075(7) Å) is longer than those of [CoTPA(3,5-di-*tert*-butyl-catecholate)]PF_6 (1.862(4) and 1.881(5) Å).[23] In the Co-dioxolene system studied here, the Co^{II}-semiquinonate bonding is probably weaker than the Co^{III}-catecholate bonding, and the emission from complex **9** is stronger than that from **7**.

Another possible mechanism for emission quenching is an ET process. Because the reduction potential of BODIPY ($E_{1/2}$ = -1.55 V) and the oxidation potential of the donor (E_{pa} = 0.82 V) in complex **7** are located in the possible range of the potentials for the ET process (*e.g.* 1,4-dimethoxybenzene as donor, E_{pa} = 0.88 V; BODIPY, $E_{1/2}$ = -1.56 V).[56] This suggests that the fluorescence quenching of a BODIPY-catechol system is caused by the intramolecular ET process and inhibited by the oxidation of a catechol moiety to quinone, which lowers the orbital energy of the electron donor species below the HOMO level of BODIPY.[64]

Emission intensities of complexes **7** and **9** in CH_3CN at room temperature slightly increased within 3 h (Figure 4-15). Hambley *et al.* reported that TPA-cobalt complexes with a fluorescent ligand exhibit the recovery of the quenched fluorescence in the presence of ascorbic acid or cysteine, arising from the ligand dissociation or exchange.[65] In complexes **7** and **9**, the ligand dissociation would be the dominant mechanism to recover the emission (Scheme 4-3), and the ligand dissociation rates were analyzed by using the following equation (1).

$$[Co(L)] \xrightarrow{k_d} [Co] + L$$

Scheme 4-3. A simple model for ligand dissociation.

$$[Int] = [Int]_0 + C[1-\exp(-k_d t)] \qquad (1)$$

The [Int], $[Int]_0$, C, k_d, and t represent the fluorescence intensity, the deduced stating value, the species dependent value, the dissociation rate constant, and time, respectively (Table 4-3). In complex **9**, the value of k_d is larger than that of complex **7**. These results are consistent with the general properties of Co(II) complexes with a rapid ligand-exchange activity. This finding supports that bond strength of the Co^{II} ion and semiquinonate ligand is weaker than that of the Co^{III} ion and catecholate ligand.

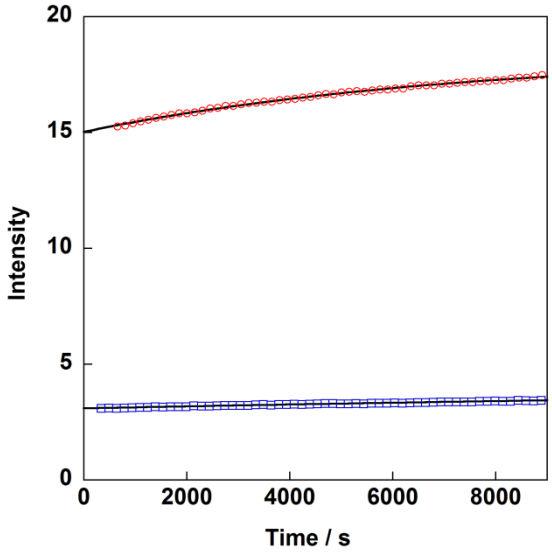

Figure 4-15. Time variations of fluorescence intensity of complexes **7** (□) and **9** (○); λ_{ex} = 470 nm, maximum fluorescence intensity (508 nm monitored) of emission spectra in CH_3CN over 9000 s.

Table 4-3. The obtained values by using equation (1).

	$[Int]_0$	C	k_d	R^2
Complex **7**	3.10	1.49	$2.93 \times 10^{-5}\ s^{-1}$	0.98677
Complex **9**	15.0	3.36	$1.38 \times 10^{-4}\ s^{-1}$	0.99706

4-3. Conclusion

The author reported the synthesis and fluorescence behavior of complexes **7**-**9** with tripodal ligands and the redox-active dioxolene-anthracene-BODIPY ligand. The absorption, IR, and NMR spectra indicated that complexes **7** and **9** are in the Co^{III}(LS)-Cat and Co^{II}(HS)-SQ forms at room temperature, respectively, and **8** is in a mixture of the Co^{III}(LS)-Cat and Co^{II}(HS)-SQ species. The spin states of **7**, **8**, and **9** are consistent with those of the dioxolene-anthracene complexes **3**, **5**, and **6**, respectively. The steric hindrance of the 6-position substitution on the pyridine ring affects the spin states of the cobalt center.[23]

To investigate the effect of the spin states of the cobalt center on the fluorescence of the BODIPY, the fluorescence properties of $\mathbf{H_2L^3}$, $\mathbf{H_2L^4}$, **3**, **7**, and **9** at room temperature in CH_3CN were characterized. Among $\mathbf{H_2L^4}$, the complexes **7**, and **9**, the most effective quench of the light emission was observed for **7**, since the binding strength of catecholate ligand is stronger than that of semiquinonate ligand, causing the enhanced nonradiative processes. In addition, the ET process also may give rise to the fluorescence quenching of BODIPY in complex **7**. In complex **9**, the quenching processes are inhibited to show higher fluorescence of BODIPY. The result is the adverse consequence to the expectation described in section 1-5-2. However, it should be stressed that the apparent modulation of the intensity was achieved by alternating the valence number and spin state of the cobalt center, which affect the binding ability to the BODIPY-ligand. To the best knowledge of the author, in BODIPY system, there are two examples that reports the fluorescence switching depending on the electronic states of a metal ion.[41] These results suggest that VT behavior is a potential method to switch the ligand-base fluorescence for future applications such as molecular-based on sensor, logic gate and so on.[66]

A method to investigate the influence of spin states should be developed. The Co^{III}(LS)-SQ species obtained by the oxidation of complexes **3** and **7** would be a useful platform to develop

the method. The introduction of a BODIPY moiety showing fluorescence in the solid state could provide another approach. Garcia *et al.* reported dependence of emission wavelength of a SCO complex with a fluorophore in the solid state on the spin state of the metal center.[20(a)]

Concluding Remarks

In this thesis, the author reported two π-spin systems; in Chapter 2, iron(II) SCO complex with π-radical ligand composed of 2,2'-bipyridine as a coordination moiety, an anthracene as a photo-sensitive moiety, and a verdazyl radical for efficient LIESST phenomenon; in Chapters 3 and 4, cobalt complexes with a dioxolene ligand containing an anthracene or an anthracene-BODIPY unit for the fluorescence switching system by VT behavior in Chapters 3 and 4.

In Chapter 2, the π-radical ligand showed the spin alignment (S = 3/2) in the photo-excited state, and the DFT calculation indicated the possibility of interaction between iron center and the π-radical ligand in the photo-excited state. The iron(II) SCO complex with π-radical ligand shows SCO and LIESST phenomena in the solid state. Antenna effect by the introduction of anthracene moiety was observed. However, the iron complex showed decrease in the photo-conversion efficiency compared with a control compound. In addition, the evidence of the interaction between iron center and the π-radical ligand in the photo-excited state was not obtained due to the rapid energy relaxation via radical moiety. In order to make the LIESST effect via the intersystem crossing in the π-ligand more efficiently, the improvement of this system is required. An ionic iron complex by using neutral supporting ligands would be one of the useful solutions. The spin transition behavior strongly depends on the intermolecular interaction, and the intermolecular interaction is affected by the counter anions.

Chapter 3 describes cobalt complexes with a dioxolene ligand containing anthracene moiety. The spin states were successfully controlled by the number of methyl groups on the pyridine ring. When Me_2TPA or MeTPA as the supporting ligand were used for synthesis of the cobalt complexes, the cobalt complexes showed VT and LIVT behavior in the solid state. TPA and

Me_3TPA complexes were Co^{III}(LS)-Cat and Co^{II}(HS)-SQ species in the range of 5–400 K, respectively. In CH_3CN at room temperature, the change of the spin states of the cobalt center was not observed in all complexes. TPA and MeTPA complexes also showed an equilibrium between the geometrical isomers in CD_3CN.

In Chapter 4, a BODIPY unit was introduced to the anthracene moiety of the cobalt complexes as a florescence site. The spin states of the cobalt center (TPA-BODIPY complex, Co^{III}(LS)-Cat; Me_3TPA-BODIPY complex, Co^{II}(HS)-SQ; Me_2TPA-BODIPY complex, the mixture of Co^{III}(LS)-Cat and Co^{II}(HS)-SQ) were retained at room temperature, because the *p*-phenylene-linked BODIPY was apart from the cobalt center. Compared with Me_3TPA complex, the fluorescence of the TPA cobalt complex was quenched more effectively by the enhanced non-radiative process due to strong coordination of catecholate ligand to Co ion. Additionally, electron transfer process probably contributes to the fluorescence quenching of BODIPY. The result is inconsistent with the hypothesis described in the introduction, although the significant difference of emission intensity between Co^{III}(LS)-Cat and Co^{II}(HS)-SQ was observed. This result indicates that the VT behavior is usable as a molecular switch of fluorescence.

Experimental Section

Measurements

IR spectra were recorded on a JASCO FT/IR-420 spectrophotometer, a Shimadzu FTIR-8600PC or a JASCO FT/IR-6200 spectrophotometer using KBr disks or in the range of 4000–400 cm^{-1}. UV-vis spectra were recorded on a Multispec-1500 or U-3500 spectrophotometer at room temperature. ^{1}H and ^{19}F NMR spectra were measured on a JEOL Lambda 300 spectrometer at room temperature. ESR and TRESR were measured on an X-band ESR spectrometer JEOL TE300. The temperature was controlled by an Oxford ESR910 cold He gas-flow system. TRESR experiments were carried out using BuCN glass matrix. Samples were degassed by repeated freeze-pump-thaw cycles. Excitations of $\mathbf{L^1}$, $\mathbf{H_2L^3}$, complexes **1**, **3** and **6** were carried out with 355 nm light from a YAG laser (Continuum Surelite II-10). Magnetic susceptibility data were measured by a SQUID magnetometer (Quantum Design MPMS2). LIESST and LIVT experiments were carried out with the SQUID magnetometer. The excitation light from the pulse laser (Continuum Surelite II connected to Continuum Surelite OPO) was introduced in the sample chamber using the quartz fiber. In the LIESST experiments, the powder samples thinly smeared on the tape were used and the magnitude of the susceptibility of the thin sample was corrected using the values of the bulk powder sample at 350 K for **1** and at 300 K for **2**. In the LIVT experiments, the powder samples thinly smeared on a tape were used. Correction for the diamagnetic contribution of the tape was not carried out.

Fluorescence properties and relative quantum yield of fluorescence

Emission spectra were recorded on a Hitachi F-7000 spectrophotometer at room temperature. All solvents for HPLC are used. The absorbance of BODIPY was set < 0.05 to avoid self-absorption and inner filter effect. The photon multiplier voltage was 400 V. In excitation at

350 and 465 nm, the slit widths were 10 and 5 nm for excitation, and both 2.5 nm for emission, respectively. Fluorescein, twice recrystallized from 6% HCl, in carbonate-bicarbonate buffer at a pH of about 9.6 was used as a standard ($\Phi = 0.85$)[61] for determination of relative fluorescence quantum yield. The fluorescence quantum yield were obtained following equation, $\Phi^{sample} = \Phi^{standard} \times (F^{sample}/F^{standard}) \times (n^{sample}/n^{standard})^2 \times (Abs^{standard}/Abs^{sample})$, where the subscripts of sample and standard represent a sample and standard, respectively. *F* and *Abs* were the area of a fluorescence spectrum in a wavenumber scale, and the absorbance at an excitation wavelength. The emission intensity at each wavelength (I(λ)) was converted into the photon number in a wavenumber scale ($n(\tilde{\upsilon})$) by using an equation, $n(\tilde{\upsilon}) = I(\lambda) \times \lambda^3$.[67] In excitation wavelength at 350 nm, the value is used as the average of absorbance at 350 ± 5 nm. *n* denotes the refractive index of the solvent.

X-ray crystallography

Diffraction data were collected on a Rigaku AFC-7/Mercury CCD area-detector diffractometer for $\mathbf{L^1}$ and a Rigaku AFC11/Saturn 724+ CCD diffractometer for **6** and $\mathbf{H_2L^4}$ with graphite monochromated Mo-Kα radiation (λ = 0.7107 Å). The CrystalClear software was used for the collection, processing and correction for Lorentzian and polarization effects. Absorption corrections were applied on comparison of multiple symmetry equivalent measurements. The structure was solved by the SIR2004 direct method[68] for $\mathbf{L^1}$, SIR97 direct method for **6** and $\mathbf{H_2L^4}$ expanded using Fourier techniques and refined by full matrix least-squares against F^2 using SHELXL-97 for $\mathbf{L^1}$ and **6**, SHELXL-2013 for $\mathbf{H_2L^4}$.[69] All non-hydrogen atoms were refined anisotropically. In complex **6**, the structure contained disordered *n*-hexane, methanol, and water molecules, and the occupancy factors of these molecules were 0.5, 0.3, and 0.5, respectively. Hydrogen atoms of the complex cation and the *n*-hexane were located at calculated positions with C–H(aromatic) = 0.95 Å, C–H(methyl) = 0.98 Å, and C–H(methylene) = 0.99 Å,

and included in the refinements using a riding model with U_{iso}(H) = 1.5U_{eq}(C) for methyl groups and 1.2U_{eq}(C) for other H atoms. Hydrogen atoms of the methanol and water molecules were not included in the model. In **H_2L^4**, the structure contained $CDCl_3$ molecules. Crystal data for **L^1**: $C_{36}H_{25}N_6O$, M = 557.62, monoclinic, space group $C2/c$ (no. 15); a = 9.454(3), b = 35.516(9), c = 8.983(3) Å, β = 113.403(3)°, V = 2768.0(13) Å^3, T = 153 K, Z = 4, D_c = 1.338 g cm^{-3}, μ = 0.084 mm^{-1}; 10630 reflections collected and 3103 independent reflections (R_{int} = 0.0272), final R indices [$I > 2\sigma(I)$] R_1 = 0.0570, wR_2 = 0.1394; R indices (all data) R_1 = 0.0770, wR_2 = 0.1570, GOF = 1.069. CCDC 894428. Crystal data for **6**: $C_{42.8}H_{41.7}CoF_6N_4O_{2.8}P$, M = 860.80, triclinic, space group $P\overline{1}$, a = 8.755(3), b = 14.874(4), c = 17.153(5) Å, α = 65.548(13)º, β = 82.182(18)º, γ = 77.872(17)º, V = 1989.5(10) Å^3, T = 153 K, Z = 2, Dc = 1.437 g/cm^3, μ = 0.545 mm^{-1}; 16431 reflections collected and 8729 independents reflections (R_{int} = 0.057), final R indices [$I > 2.0\ \sigma(I)$] R_1 = 0.0698, wR_2 = 0.1848; R indices (all data) R_1 = 0.1234, wR_2 = 0.2148, GOF = 0.960. CCDC 1004505. Crystal data for **H_2L^4**: $C_{41}H_{29}BCl_6D_2F_2N_2O_2$, M = 847.20, monoclinic, space group P_{21}/c, a = 14.772(2), b = 13.618(2), c = 19.448(3) Å, β = 90.523(3)º, V = 3912.1(10) Å^3, T = 153 K, Z = 4, Dc = 1.438 g/cm^3, μ = 0.488 mm^{-1}; 8827 reflections collected and 5743 independents reflections (R_{int} = 0.0431), final R indices [$I > 2.0\ \sigma\ (I)$] R_1 = 0.0774, wR_2 = 0.2034; R indices (all data) R_1 = 0.1130, wR_2 = 0.2314, GOF = 1.098.

Molecular orbital calculations

Molecular orbital calculations of **L^1**, complexes **1** were performed using the Gaussian 03 program package.[70] The unrestricted B3LYP density functional method was used for the calculations. The 6-31G and LANL2DZ basis sets were used for **L^1**, and for **1,** respectively. The DFT calculations of **L^1** were performed for the ground and photo-excited states. In complex **1** the low-spin state (S = 1/2) and the ferromagnetically coupled high spin state (S = 5/2) were investigated.

Materials

N,*N*′-Dimethylcarbonohydrazide,[71(a)] 5-bromo-2,2′-bipyridine,[71(b)] 9-(*p*-formylphenyl)-10-bromoanthracene,[29(f)] TPA and Me$_n$TPA ligands,[23] and (3,4-Bis(methoxymethoxy)phenyl)boronic acid[71(c)] were prepared according to literature procedures. Modification of the procedure using 9-phenylanthracene instead of 9-(*p*-formyl-phenyl)anthracene gave 9-phenyl-10-bromoanthracene. Other reagents were used as purchased. Silica gel (Merk silica 60) or alumina (Merk Alum. Ox. 60) was used for column chromatography.

5-Ethynyl-2,2′-bipyridine (i).

A solution of 5-bromo-2,2′-bipyridine (0.24 g, 1 mmol), [Pd(PPh$_3$)$_4$] (58 mg), CuI (19 mg), and trimethylsilylacetylene (0.20 g, 2 mmol) in THF (20 mL) and Et$_3$N (4 mL) was stirred at room temperature for 1 day under nitrogen. Activated carbon (0.10 g) was added, and the reaction mixture was stirred for 30 min, and filtered. The solvent of the filtrate was removed under reduced pressure. The residue was added to a solution of K$_2$CO$_3$ (0.15 g, 1.1 mmol) in MeOH (10 mL), and filtered. The solvent of the filtrate was removed under reduced pressure. The crude product was purified by silica gel column chromatography (ethyl acetate–*n*-hexane = 1 : 1) to give (**i**) in 61% yield (0.11 g). ^{1}H NMR (300 MHz, CDCl$_3$): δ 8.78 (dd, *J* = 2.1, 0.75 Hz, bpy, 1H), 8.69 (ddd, *J* = 4.8, 1.8, 1.1 Hz, bpy, 1H) 8.41 (dt, *J* = 7.6, 1.1 Hz, bpy, 1H), 8.40 (dd, *J* = 8.2, 0.75 Hz, bpy, 1H), 7.90 (dd, *J* = 8.2, 2.1 Hz, bpy, 1H), 7.84 (td, *J* = 7.6, 1.8 Hz, bpy, 1H), 7.33 (ddd, *J* = 7.5, 4.8, 1.1 Hz, bpy, 1H), 3.29 (s, CH, 1H).

9-(*p*-Formylphenyl)-10-[5-(2,2′-bipyridyl)ethynyl]anthracene (ii).

A mixture of 5-ethynyl-2,2′-bipyridine (i) (55 mg, 0.3 mmol), 9-(*p*-formylphenyl)-10-bromoanthracene (0.11 g, 0.3 mmol), [Pd(PPh$_3$)$_4$] (17 mg), CuI (5.7 mg) in Et$_3$N (10 mL) and THF (5 mL) was refluxed for 8 h under nitrogen. The solvent was removed

under reduced pressure. The crude product was purified by silica gel column chromatography (ethyl acetate–*n*-hexane = 1 : 4) to give (ii) in 66% yield (91 mg). ^{1}H NMR (300 MHz, $CDCl_3$): δ 10.2 (s, CHO, 1H), 9.08 (d, *J* = 2.1 Hz, bpy, 1H), 8.77–8.74 (m, an, 2H), 8.73 (d, *J* = 1.7 Hz, bpy, 1H), 8.54(d, *J* = 7.8 Hz, bpy, 1H), 8.50 (dd, *J* = 8.0, 1.0 Hz, bpy, 1H), 8.20 (dd, *J* = 7.8, 2.1 Hz, bpy, 1H), 8.14 (d, *J* = 7.7 Hz, ph, 2H), 7.9 (td, *J* = 8.0, 1.7 Hz, bpy, 1H), 7.68–7.59 (m, ArH, 6H), 7.47–7.36 (m, ArH, 3H). Anal. Calcd for $C_{33}H_{20}N_2O{\cdot}0.2CH_2Cl_2$: C, 83.51; H, 4.31; N, 5.87. Found: C83.46; H, 4.53; N, 5.76. IR (cm^{-1}): 1704, 1602, 1586, 1541, 1457, 1374, 1206.

9-[4-(6-Oxo-1,5-dimethyl-1,2,4,5-tetrazinan-3-yl)phenyl]-10-[5-(2,2′-bipyridyl)ethynyl]anthracene (iii).

To a solution of carbonic acid bis(1-methylhydrazide) (39 mg, 0.33 mmol) in MeOH (5 mL) and THF (5 mL), was added dropwise a solution of (ii) (50 mg, 0.11 mmol) in MeOH (5 mL) and THF (5 mL), and the mixture was stirred at room temperature for 3 h. The reaction mixture was evaporated under reduced pressure and the crude residue was washed by MeOH to give (iii) in 57% yield (35 mg) as a crude product. ^{1}H NMR (300 MHz, $CDCl_3$): δ 9.08 (d, *J* = 1.34 Hz, bpy, 1H), 8.75–8.72 (m, ArH, 3H), 8.55–8.49 (m, bpy, 2H), 8.19 (dd, *J* = 8.3, 1.6 Hz, bpy, 1H), 7.87 (td, *J* = 8.0, 1.8 Hz, bpy, 1H), 7.77 (d, *J* = 8.3 Hz, ph, 2H), 7.66–7.61 (m, an, 4H), 7.48 (d, *J* = 8.3 Hz, ph, 2H), 7.45–7.26 (m, ArH, 3H), 5.24 (t, *J* = 9.9 Hz, CH, 1H), 4.55 (d, *J* = 9.9 Hz, NH, 2H), 3.25(s, CH_3, 6H).

9-[4-(6-Oxo-1,5-dimethylverdazyl)phenyl]-10-[5-(2,2′-bipyridyl)-ethynyl]anthracene (L^1).

Solvents were purified by passage through a column of activated alumina. A mixture of (**iii**) (61 mg, 0.11 mmol) and *p*-benzoquinone (37 mg, 0.34 mmol) in CH_2Cl_2 (20 mL) was stirred at room temperature for 1 day. The reaction mixture was concentrated under reduced pressure. The residue was chromatographed on alumina with CH_2Cl_2, and recrystallized from *n*-hexane–CH_2Cl_2 to give **L^1** in 27% yield (16 mg). Crystals of **L^1** appropriate for single crystal X-ray

analysis were obtained by diffusion of *n*-hexane into a CH_2Cl_2 solution of **L**^{1}. ^{1}H NMR (300 MHz, $CDCl_3$): δ 9.13 (s, bpy, 1H), 8.79–8.73 (br, ArH, 4H), 8.55–8.50 (br, ArH, 3H), 8.24 (d, *J* = 8.4 Hz, bpy, 1H), 7.87 (t, *J* = 8.4 Hz, bpy, 1H), 7.77-7.48 (br, ArH, 6H), 7.36 (dd, *J* = 7.5, 4.8 Hz, bpy, 1H). Anal. Calcd for $C_{36}H_{25}N_6O$: C, 77.54; H, 4.52; N, 15.07. Found: C, 76.89; H, 4.66; N, 14.60. IR (cm^{-1}): 1690, 1540, 1507, 1457, 1395, 1295, 1249.

9-Phenyl-10-[5-(2,2′-bipyridyl)ethynyl]anthracene (**L**^{2}).

Amixture of 5-ethynyl-2,2′-bipyridine (**i**) (54 mg, 0.3 mmol), 9-phenyl-10-bromoanthracene (0.10 g, 0.3 mmol), $[Pd(PPh_3)_4]$ (17 mg), CuI (5.7 mg) in Et_3N (10 mL) and THF (5 mL) was refluxed for 6 h under nitrogen. The solvent was removed under reduced pressure. The crude product was purified by silica gel column chromatography (ethyl acetate–*n*-hexane = 1 : 2) to give **L**^{2} in 53% yield (68 mg). ^{1}H NMR (300 MHz, $CDCl_3$): δ 9.81 (d, *J* = 2.2 Hz, bpy, 1H), 8.75–8.73 (m, an, 2H), 8.74 (d, *J* = 1.8 Hz, 1H), 8.52 (m, bpy, 2H), 8.19 (dd, *J* = 8.1, 2.2 Hz, bpy, 1H), 7.87 (td, *J* = 7.8, 1.8 Hz, bpy, 1H), 7.71–7.56 (m, ArH, 8H), 7.46–7.34 (m, ArH, 4H). IR (cm^{-1}): 1651, 1587, 1541, 1458, 1432, 1396.

[Fe(L^1){H$_2$B(Pz)$_2$}$_2$] (**1**).

All the manipulations were carried out under N_2 atmosphere. To a solution of $KH_2B(Pz)_2$ (20 mg, 0.11 mmol) in MeOH (3 mL) was added a solution of $Fe(ClO_4)_2{\cdot}6H_2O$ (20 mg, 0.054 mmol) in MeOH (2 mL). The mixture was stirred for 10 min and filtered. The solvent of filtrate was removed under reduced pressure. To the residue dissolved in CH_2Cl_2 (10 mL) was added a solution of **L**^{1} (30 mg, 0.054 mmol) in CH_2Cl_2 (15 mL), and the solution was stirred for 20 min. *n*-Hexane was added to the solution to give a dark green precipitate, which was filtered, washed with *n*-hexane, and dried under reduced pressure. Yield: 19 mg (38%). Anal. Calcd for $C_{48}H_{41}B_2FeN_{14}O{\cdot}0.5CH_2Cl_2$: C, 61.33; H, 4.46; N, 20.64. Found: C, 61.99; H, 4.78; N, 20.36.

[Fe(L^2){H$_2$B(Pz)$_2$}$_2$] (**2**).

All the manipulations were carried out under N_2 atmosphere. To a solution of $KH_2B(Pz)_2$ (46 mg, 0.25 mmol) in MeOH (10 mL) was added a solution of $Fe(ClO_4)_2 \cdot 6H_2O$ (45 mg, 0.12 mmol) in MeOH (5 mL). The mixture was stirred for 10 min and filtered. To the filtrate was added a solution of $\mathbf{L^2}$ (54 mg, 0.12 mmol) in CH_2Cl_2 (20 mL), and the solution was stirred for 20 min. The solution was concentrated to remove CH_2Cl_2. A greenish yellow solid was precipitated, filtered, washed with MeOH, and dried under reduced pressure. Yield: 42 mg (43%). Anal. Calcd for $C_{44}H_{36}B_2FeN_{10} \cdot 0.7CH_2Cl_2$: C, 63.78; H4.48; N, 16.64. (Anal. Calcd for $C_{44}H_{36}B_2FeN_{10} \cdot 0.5CH_2Cl_2 \cdot 0.5CH_3OH$: C, 64.28; H4.68; N, 16.66.) Found: C, 63.59; H, 4.46; N, 17.27.

9-(3,4-Dimethoxyphenyl)anthracene (vi)

A solution of 9-bromoanthracene (3.5 g, 14 mmol), 3,4-dimethoxyphenylboronic acid (2.5 g, 14 mmol), $Pd(PPh_3)_4$ (0.16 g), K_2CO_3 (3.8 g, 27 mmol) in 1,2-dimethoxyethane (DME) (180 mL) and H_2O (60 mL) was refluxed under nitrogen. After 6 h, DME was removed under reduced pressure. The residue was filtered and washed by EtOH to give (**i**) in 89% yield (3.8 g). ^{1}H NMR ($CDCl_3$): δ 8.49 (s, an, 1H), 8.05 (d, *J* = 8.4 Hz, an, 2H), 7.74 (d, *J* = 8.4 Hz, an 2H), 7.46 (ddd, *J* = 8.4, 6.3, 1.2 Hz, an, 3H), 7.36 (ddd, *J* = 8.4, 6.3, 1.2 Hz, an, 2H), 7.09 (d, *J* = 8.4 Hz, 1H), 6.99 (dd, *J* = 8.4, 1.8 Hz, 1H), 6.95 (d, *J* = 1.8 Hz, 1H), 4.02 (s, Me, 3H), 3.86 (s, Me, 3H). Anal. Calcd for $C_{22}H_{18}O_2$: C, 84.05; H, 5.77; N, 0.00. Found: C, 83.91; H, 5.83; N, 0.00. IR (cm^{-1}): 1510, 1459, 1414, 1358, 1252, 1232, 1133, 1126.

9-(3,4-Dihydroxyphenyl)anthracene (H_2L^3)

Under nitrogen atmosphere, a solution of compound (**vi**) (1.7 g, 5.3 mmol) in CH_2Cl_2 (60 mL) was cooled to −78 ºC in a dry ice/acetone bath. Boron tribromide solution (1.0 M in CH_2Cl_2, 11 mL, 11 mmol) was added slowly over 10 min, after which the bath was removed. The reaction was stirred for 2 h at room temperature, and then ice-cold H_2O was added and stirred for an

additional 20 min. The reaction mixture was extracted by EtOAc, washed with brine, and dried with $MgSO_4$. The solvent was removed under reduced pressure and the crude product was purified by silica gel chromatography (CH_2Cl_2) to give **H_2L^3** in 65% yield (0.99 g). ^{1}H NMR ($CDCl_3$): δ 8.47 (s, an, 1H), 8.03 (d, *J* = 8.4 Hz, an, 2H), 7.73 (d, *J* = 8.4 Hz, an, 2H), 7.45 (ddd, *J* = 8.4, 6.3, 1.2 Hz, an, 2H), 7.34 (ddd, *J* = 8.4, 6.3, 1.2 Hz, an, 2H), 7.07 (d, *J* = 8.0 Hz, 1H), 6.94 (d, *J* = 2.0 Hz, 1H), 6.87 (dd, *J* = 8.0, 2.0 Hz, 1H), 5.33 (s, OH, 1H), 5.26 (s, OH, 1H). Anal. Calcd for $C_{20}H_{14}O_2 \cdot 0.7H_2O$: C, 80.36; H, 5.19. Found: C, 80.20; H, 5.28. IR (cm^{-1}): 3467, 1608, 1527, 1427, 1250, 1200, 1105.

[Co(TPA)(L^3)]PF_6 (3)

A solution of cobalt(II) chloride (19 mg, 0.15 mmol) and TPA ligand (44 mg, 0.15 mmol) in MeOH (20 mL) were mixed with a solution of **H_2L^3** (43 mg, 0.15 mmol) and Et_3N (0.3 mmol) in MeOH (15 mL) under nitrogen atmosphere. The reaction mixture was oxidized with atmospheric O_2, The resulting product was precipitated by adding an aqueous solution of KPF_6. Complex **3** was obtained by recrystallization from MeOH/H_2O as a green powder. **3**·H_2O: yield 67% (81 mg). Anal. Calcd for $C_{38}H_{30}CoN_4O_2PF_6 \cdot H_2O$: C, 57.30; H, 4.05; N, 7.03. Found: C, 57.29; H, 4.00; N, 7.06.

[Co(MeTPA)(L^3)]PF_6 (4)

A solution of cobalt(II) chloride (19 mg, 0.15 mmol) and MeTPA ligand (46 mg, 0.15 mmol) in MeOH (20 mL) were mixed with a solution of **H_2L^3** (43 mg, 0.15 mmol) and Et_3N (0.3 mmol) in MeOH (15 mL) under nitrogen atmosphere. The reaction mixture was oxidized with atmospheric O_2. The resulting product was precipitated by adding an aqueous solution of KPF_6. Complex **4** was obtained by recrystallization from CH_2Cl_2/*n*-hexane as a dark green powder. **4**: yield 59% (70 mg). Anal. Calcd for $C_{39}H_{32}CoN_4O_2PF_6$: C, 59.10; H, 4.07; N, 7.07. Found: C, 59.12; H, 4.29; N, 6.81.

[Co(Me$_2$TPA)(L^3)]PF$_6$ (5)

A solution of cobalt(II) chloride (19 mg, 0.15 mmol) and Me$_2$TPA ligand (48 mg, 0.15 mmol) in MeOH (20 mL) were mixed with a solution of **H$_2$L^3** (43 mg, 0.15 mmol) and Et$_3$N (0.3 mmol) in MeOH (15 mL) under nitrogen atmosphere. The reaction mixture was oxidized with atmospheric O_2. The resulting product was precipitated by adding an aqueous solution of KPF_6. Complex **5** was obtained by recrystallization from CH_2Cl_2/*n*-hexane as a yellow-brown powder. **5**·0.5*n*-hexane: yield 65% (78 mg). Anal. Calcd for $C_{40}H_{34}CoN_4O_2PF_6$·0.5*n*-hexane: C, 60.78; H, 4.86; N, 6.59. Found: C, 60.80; H, 4.39; N, 6.19.

[Co(Me$_2$TPA)(L^3)]PF$_6$ (6)

A solution of cobalt(II) chloride (19 mg, 0.15 mmol) and Me$_3$TPA ligand (50 mg, 0.15 mmol) in MeOH (20 mL) were mixed with a solution of **H$_2$L^3** (43 mg, 0.15 mmol) and Et$_3$N (0.3 mmol) in MeOH (15 mL) under nitrogen atmosphere. The reaction mixture was oxidized with atmospheric O_2. The resulting product was precipitated by adding an aqueous solution of KPF_6. Complex **6** was obtained by recrystallization from CH_2Cl_2/*n*-hexane as blue-black crystals. **6**·0.8*n*-hexane: yield 63% (77 mg). Anal. Calcd for $C_{41}H_{36}CoN_4O_2PF_6$·0.8*n*-hexane: C, 61.84; H, 5.35; N, 6.30. Found: C, 62.32; H, 4.70; N, 6.00.

9-bromo-10-[4,4-difluoro-1,3,5,7-tetramethyl-8-(phenyl)-4-bora-3a,4a-diaza-s-indacence]anthracene, (vii)

9-(*p*-formylphenyl)-10-bromoanthracene (1.7 g, 4.8 mmol), 2,4-dimethylpyrrole (1.1 mL, 11 mmol) and 3 drops of trifluoroacetic acid were dissolved in absolute CH_2Cl_2 (60 mL) under N_2 atmosphere, and the solution was stirred for overnight. A solution of *p*-chloranil (1.0 g, 4.8 mmol) in CH_2Cl_2 (20 mL) was added to the solution and stirred for 30 min. To a reaction mixture was added *N*,*N*-diisopropylethylamine (16 mL, 12 mmol), stirred for 10 min under N_2 atmosphere, and then added BF_3OEt_2 (11 mL, 12 mmol) at 0 °C and stirred for 3 h. The reaction

mixture was washed with water, extracted with CH_2Cl_2 and dried with $MgSO_4$. The crude product was preadsorbed onto a minimal amount of silica and dried under vacuum. Flash column chromatography provided a dark purple solution. The solution was concentrated, filtered and washed with a minimal amount of cold CH_2Cl_2 to give the precipitate of compound as orange powder in 19% yield (522 mg). ^{1}H NMR ($CDCl_3$): δ 8.65 (d, J = 8.7 Hz, An, 2H), 7.65-7.55 (m, ArH, 8H), 7.41 (ddd, J = 8.7, 6.5, 1.2 Hz, An, 2H), 6.09 (s, Py, 2H), 2.61 (s, Me, 6H), 1.71 (s, Me, 6H). Anal. Calcd for $C_{33}H_{26}N_2BrBF_2$: C, 68.42; H, 4.52; N, 4.84. Found: C, 68.19; H, 4.67; N, 4.87. IR (cm^{-1}): 2926, 1546, 1510, 1467, 1408, 1308, 1251, 1193, 1157, 1075, 978.

9-(3,4-Bis(methoxymethoxy)phenyl)-10-[4,4-difluoro-1,3,5,7-tetramethyl-8-(phenyl)-4-bora-3a,4a-diaza-s-indacence]anthracene, (viii)

A solution of Br-An-BODIPY (0.20 g, 0.35 mmol), 3,4-Bis(methoxymethoxy)phenyl boronic acid (0.11 g, 0.44 mmol), $Pd(PPh_3)_4$ (0.040 g), K_2CO_3 (0.10 g, 0.70 mmol) in 1,2-dimethoxyethane (DME) (40 mL) and H_2O (20 mL) was refluxed under nitrogen. After 6 h, DME was removed under reduced pressure and the residue was filtered. The precipitate was purified by silica column chromatography (CH_2Cl_2) and recrystallized from CH_2Cl_2-MeOH to give compound as orange powder in 68% yield (166 mg). ^{1}H NMR ($CDCl_3$): δ 7.86-7.79 (m, ArH, 2H), 7.66-7.53 (m, ArH, 6H), 7.42-7.32 (m, ArH, 5H), 7.29 (d, J = 2.1 Hz, $(MOMO)_2$-PhH, 1H), 7.10 (dd, J = 8.2, 2.0 Hz, $(MOMO)_2$-PhH, 1H), 6.09 (s, Py, 2H), 5.40 (s, $-OCH_2O-$, 2H), 5.27 (s, $-OCH_2O-$, 2H), 3.66 (s, $-OCH_3$, 3H), 3.52 (s, $-OCH_3$, 3H), 2.61 (s, Me, 6H), 1.74 (s, Me, 6H). Anal. Calcd for $C_{43}H_{39}N_2O_4BF_2$: C, 74.14; H, 5.64; N, 4.02. Found: C, 73.91; H, 5.78; N, 4.05. IR (cm^{-1}): 2926, 1546, 1510, 1467, 1408, 1308, 1251, 1193, 1157, 1075, 978.

9-(3,4-dihydroxyphenyl)-10-[4,4-difluoro-1,3,5,7-tetramethyl-8-(phenyl)-4-bora-3a,4a-diaz

a-s-indacence]anthracene, H_2L^4

To a solution of (i) (0.40 g, 0.57 mmol) in CH_2Cl_2 (20 mL) was added a solution of TsOH•H_2O (0.54 g, 2.8 mmol) in EtOH (10 mL) and stirred for overnight. The solvent was removed under vacuum. The crude product was purified by silica column chromatography (THF-CH_2Cl_2 (1:6)) and recrystallized from THF-Et_2O to give red crystals in 88% yield (307 mg). ^{1}H NMR ($CDCl_3$): δ 7.83-7.80 (m, ArH, 2H), 7.66-7.59 (m, ArH, 4H), 7.52 (td, *J* = 8.3, 1.5Hz, An, 2H), 7.40-7.31 (m, ArH, 4H), 7.11 (d, *J* = 8.0 Hz, $(HO)_2$-PhH, 1H), 6.99 (d, *J* = 1.7 Hz, $(HO)_2$-PhH, 1H), 6.93 (dd, *J* = 8.0, 1.7 Hz, $(HO)_2$-PhH, 1H), 6.08 (s, Py, 2H), 5.57 (br, OH, 2H), 2.61 (s, Me, 6H), 1.72 (s, Me, 6H) Anal. Calcd for $C_{39}H_{31}N_2O_2BF_2$•1.5THF: C, 75.58; H, 5.85; N, 3.92. Found: C,75.27; H, 5.82; N, 4.19. IR (cm^{-1}): 2925, 1546, 1511, 1469, 1440, 1409, 1372, 1307, 1271, 1190, 1157, 1089, 1045, 1026, 978.

[Co(TPA)(L^4)]PF_6 (7)

Under nitrogen atmosphere, a solution of $CoCl_2$ (9.8 mg, 0.075 mmol), TPA (0.075 mmol) and Et_3N in MeOH (15 mL) was mixed with a solution **H_2L^4** (46 mg, 0.075 mmol) in THF (15 mL). The reaction mixture was stirred for 1 h, and then oxidized with atmospheric O_2. *n*-Bu_4NPF_6 (excess) was added to the solution and stirred for 1 h. The solvent was removed under reduced pressure. The crude product was washed with MeOH and recrystallized from CH_2Cl_2-Et_2O to give the complex. **7**: yield 60% (49 mg). Anal. Calcd for $C_{57}H_{47}N_6O_2PCoBF_8$•0.3$CH_2Cl_2$: C, 61.11; H, 4.26; N, 7.46. Found: C, 61.08; H, 4.49; N, 7.36.

[Co(Me_2TPA)(L^4)]PF_6 (8)

Under nitrogen atmosphere, a solution of $CoCl_2$ (9.8 mg, 0.075 mmol), Me_2TPA (0.075 mmol) and Et_3N in MeOH (15 mL) was mixed with a solution **H_2L^4** (46 mg, 0.075 mmol) in THF (15 mL). The reaction mixture was stirred for 1 h, and then oxidized with atmospheric O_2. *n*-Bu_4NPF_6 (excess) was added to the solution and stirred for 1 h. The solvent was removed

under reduced pressure. The crude product was washed with MeOH and recrystallized from CH_2Cl_2-Et_2O to give the complex. **8**: yield 17% (14 mg). Anal. Calcd for $C_{59}H_{51}N_6O_2PCoBF_8$•0.1$CH_2Cl_2$: C, 62.42; H, 4.54; N, 7.39. Found: C, 62.59; H, 4.71; N, 7.14.

[Co(Me$_3$TPA)(L^4)]PF$_6$ (9)

Under nitrogen atmosphere, a solution of $CoCl_2$ (9.8 mg, 0.075 mmol), Me_3TPA (0.075 mmol) and Et_3N in MeOH (15 mL) was mixed with a solution **H$_2$L^4** (46 mg, 0.075 mmol) in THF (15 mL). The reaction mixture was stirred for 1 h, and then oxidized with atmospheric O_2. *n*-Bu_4NPF_6 (excess) was added to the solution and stirred for 1 h. The solvent was removed under reduced pressure. The crude product was washed with MeOH and recrystallized from CH_2Cl_2-Et_2O to give the complex **9**: yield 14% (12 mg). Anal. Calcd for $C_{60}H_{53}N_6O_2PCoBF_8$•0.4$CH_2Cl_2$: C, 61.65; H, 4.61; N, 7.14. Found: C, 61.53; H, 4.72; N, 7.29.

References

1. (a) A. Aviram, M. A. Ratner, *Chem. Phys. Lett*., 1974, **29**, 277. (b) A. R. Rocha, V. M. Garcia-suárez, S. W. Bailey, C. J. Lambert, J. Ferrer, S. Sanvito, *Nat. Mater*., 2005, **4**, 335. (c) O. Sato, J. Tao and Y.-Z. Zhang, *Angew. Chem., Int. Ed.*, 2007, **46**, 2152. (d) S. Sanvito, *Chem. Soc. Rev*., 2011, **40**, 3336. (e) A. Coskun, J. M. Spruell, G. Barin, W. R. Dichel, A. H. Flood, Y. Y. Botros, J. F. Stoddart, *Chem. Soc. Rev*., 2012, **41**, 4827. (f) S. V. Aradhya, L. Venkataraman, *Nat. Nanotechnol*., 2013, **8**, 399. (g) T. Zelovich, L. Kronik, O. Hod, *J. Chem. Theory Comput.*, 2015, **11**, 4861.
2. (a) P. Gütlich, A. Hauser, H. Spiering, *Angew. Chem. Int. Ed. Engl*. 1994, **33**, 2024. (b) J. A. Real, A. B. Gaspar, M. C. Muñoz, *Dalton Trans*, 2005, 2062. (c) A. Bousseksou, G. Molnár, L. Salmon, W. Nicolazzi, *Chem. Soc. Rev*. 2011, **40**, 3313. (d) P. Gütlich, A. B. Gaspar, Y. Garcia, *Beilstein J. Org. Chem*., 2013, **9**, 342. (e) G. Molnár, L. Salmon, W. Nicolazzi, F. Terki, A. Bousseksou, *J. Mater. Chem*. C, 2014, **2**, 1360.
3. (a) E. Evangelio, D. Ruiz-Molina, *Eur. J. Inorg. Chem*., **2005**, 2957. (b) A. Dei, D. Gatteschi, C. Sangregorio, L. Sorace, *Acc. Chem. Res*., 2004, **37**, 827. (c) T. Tezgerevska, K. G. Alley, C. Boskovic, *Coord. Chem. Rev*., 2014, **268**, 23.
4. (a) O. Kahn, C. J. Martinez, *Science*, 1998, **279**, 44. (b) C. Edder, C. Piguet, J.-C. G. Bünzli, G. Hopfgartner, *Chem. Eur. J*., 2001, **7**, 3014. (c) Special Issue: "Spin-Crossover Complexes" (Eds.: K. S. Murray, H. Oshio, J. A. Real), *Eur. J. Inorg. Chem*., 2013, 574.
5. (a) J.-F. Létard, P. Guinneau, o. Nguyen, J. S. Costa, S. Marcén, G. Chastanet, M. Marchivie, L. Goux-Capes, *Chem. Eur. J*., 2005, **11**, 4582. (b) O. Sato, A. Cui, R. Matsuda, J. Tao, S. Hayami, *Acc. Chem. Res.*, 2007, **40**, 361.
6. (a) Y. Teki, S. Miyamoto, K. Iimura, M. Nakatsuji, Y. Miura, *J. Am. Chem. Soc*., 2000, **122**,

984. (b) Y. Teki, S. Miyamoto, M. Nakatsuji, Y. Miura, *J. Am. Chem. Soc*., 2001, **123**, 294.

7. L. Cambi, L. Szego, *Chem. Ber. Dtsch. Ges*., 1931, **64**, 2591.
8. W. A. Baker, H. M. bobonich, Jr., *Inorg. Chem*., 1964, **3**, 1184.
9. (a) S. Mossin, B. L. Tran, D. Adhikari, M. Pink, F. W. Heinemann, J. Sutter, R. K. Szilagyi, K. Meyer, D. J. Mindiola, *J. Am. Chem. Soc*., 2012, **134**, 13651. (b) Y. Ohgo, Y. Chiba, D. Hashizume, H. Uekusa, T. Ozeki, M. Nakamura, *Chem. Commun*., 2006, 1935. (c) P. J. Alonso, A. B. Arauzo, J. Forniés, M. A. García-Monforte, A. Martín, J. I. Martínez, B. Menjón, C. Rillo, J. J. Sáiz-Gartiaonandia, *Angew. Chem. Int. Ed.*, 2006, **45**, 6707. (d) R. Weiss, A. Gold, J. Terner, *Chem. Rev*., 2006, **106**, 2550.
10. (a) H. A. Goodwin, *Coord. Chem. Rev*., 1976, **18**, 293. (b) E. König, G. Ritter, S. K. Kulshreshtha, *Chem. Rev*., 1985, **85**, 219. (c) O. Kahn, *Molecular Magnetism*, VCH, New York, 1993.
11. (a) S. Hayashi, Z.-Z. Gu, H. Yoshiki, A. Fujishima, O. Sato, *J. Am. Chem. Soc*., 2001, **123**, 11644. (b) A. Tissot, H. J. Shepherd, L. Toupet, E. Collet, J. Sainton, G. Molnár, P. Guionneau, M.-L. Boillot, *Eur. J. Inorg. Chem*., 2013, 1001.
12. (a) J. Faus, M. Julve, F. Lloret, J. A. Real, J. Sletten, *Inorg. Chem*. 1994, **33**, 5535. (b) J. Zarembowitch, O. Kahn, *Inorg. Chem*., 1984, **23**, 589.
13. P. G. Sim, E. Sinn, *J. Am. Chem. Soc*., 1981, **103**, 241.
14. D. M. Halepoto, D. G. L. Holt, L.F. Larkwoerthy, G. J. Leigh, D. C. Povey, G. W. Smith, *J. Chem. Soc., Chem. Commun.*, 1989, 1322.
15. C. P. Slichter, H. G. Drickmer, *J. Chem. Phys*., 1972, **56**, 2142.
16. (a) J. A. Real, A. B. Gaspar, V. Niel, M. C. Muñoz, *Coord. Chem. Rev*., 2003, **236**, 121. (b) S. Brooker, *Chem. Soc. Rev*., 2015, **44**, 2880.
17. J. F. Létard, P. Guionneau, E. Codjovi, O. Lavastre, G. Bravic, D. Chasseau, O. Kahn, *J.*

Am. Chem. Soc., 1997, **119**, 10861.

18. (a) M. Sorai, J. Ensling, K. M. Hasselbach, P. Gütlich, *Chem. Phys*., 1977, **20**, 197. (b) A. M. Greenaway, C. J. O'Connor, A. Schrock, E. Sinn, *Inorg. Chem*., 1979, **18**, 2692. (c) Z. Ni, S. R. Fiedler, M. P. Shores, *Dalton Trans*. 2011, **40**, 944.
19. (a) S. Decurtins, P. Gütlich, C. P. Kohler, H. Spiering, A. Hauser, *Chem. Phys. Lett*., 1984, **105**, 1. (b) S. Decurtins, P. Gütlich, K. M. Hasselbach, H. Spiering, A. Hauser, *Inorg. Chem*., 1985, **24**, 2174.
20. (a) Y. Garcia, F. Robert, A. D. Naik, G. Zhou, B. Tinant, K. Robeyns, S. Michotte, L. Piraux, *J. Am. Chem. Soc*., 2011, **133**, 15850. (b) C.-F. Wang, R.-F. Li, X.-Y. Chen, R.-J. Wei, L.-S. Zheng, J. Tao, *Angew. Chem. Int. Ed.*, 2015, **54**, 1574. (c) K. Takahashi, H.-B. Cui, Y. Okano, H. Kobayashi, Y. Einaga, O. Sato, *Inorg. Chem.*, 2006, **45**, 5739. (d) K. Takahashi, H.-B. Cui, Y. Okano, H. Kobayashi, H. Mori, H. Tajima, Y. Einaga, O. Sato, *J. Am. Chem. Soc*., 2008, **130**, 6688. (e) A. B. Gaspar, M. Seredyuk, P. Gütlich, *J. Mol. Struct*., 2009, 924.
21. (a) C. Roux, J. Zarembowitch, B. Gallois, T. Granier, R. Claude, *Inorg. Chem.*, 1994, **33**, 2273. (b) S. Venkataramani, U. Jana, M. Dommaschk, F. D. Sonnichsen, F. Tuczek, R. Herges, *Science*, 2011, **331**, 445. (c) B. Rosner, M. Milek, A. witt, B. Gobaut, P. Torelli, R. H. Fink, M. Khusniyarov, *Angew. Chem. Int. Ed*., 2015, **54**, 1.
22. (a) R. M. Buchanan, C. G. Pierpont, *J. Am. Chem. Soc*., 1980, **102**, 4951. (b) D. M. Adams, A. Dei, A. L. Rheingold, D. N. Hendrickson, *J. Am. Chem. Soc*., 1993, **115**, 8221.
23. A. Beni, A. Dei, S. Laschi, M. Rizzitano, L. Sorace, *Chem. Eur. J*., 2008, **14**, 1804.
24. S. Goswami, A. Panja, R. J. Butcher, N. Shaikh, P. Banerjee, *Inorg. Chim. Acta*, 2011, **370**, 311.
25. (a) S. K. Larsen, C. G. Pierpont, *J. Am. Chem. Soc*., 1988, **110**, 1827. (b) K.S. Min, T.

Weyhermüller, K. Wieghardt, *Dalton Trans*., 2004, 178. (c) D. Chang, T. Malinski, A. Ulman, K. M. Kadish, *Inorg. Chem*., 1984, **23**, 817. (d) J. Seth, V. Palaniappan, D. F. Bocian, *Inorg. Chem*., 1995, **34**, 2201. (e) I. Ratera, D. Ruiz-Molina, F. Renz, J. Ensling, K. Wurst, C. Rovira, P. Gütlich, J. Veciana, *J. Am. Chem. Soc*., 2003, **125**, 1462.

26. (a) D. M. Adams, B. Li, D. Simon, D. N. Hendrickson, *Angew. Chem. Int. Ed. Engl*., 1995, **34**, 1481. (b) D. M. Adams, D. N. Hendrickson, *J. Am. Chem. Soc*., 1996, **118**, 11515.
27. O. Sato, S. Hayashi, Z.-Z. Gu, R. Saki, R. Nakajima, A. Fujishima, *Chem, Lett.*, 2001, 874.
28. A. Witt, F. W. Heinemann, M. Khusniyarov, *Chem. Sci*., 2015, **6**, 4599.
29. (a) Y. Teki, M. Nakatsuji and Y. Miura, *Mol. Phys*., 2002, **100**, 1385. (b) Y. Teki, *Polyhedron*, 2001, **20**, 1163. (c) Y. Teki, M. Kimura, S. Narimatsu, K. Ohara and K. Mukai, *Bull. Chem. Soc. Jpn*., 2004, **77**, 95. (d) Y. Teki and S. Nakajima, *Chem. Lett*., 2004, **33**, 1500. (e) Y. Teki, T. Toichi and S. Nakajima, *Chem. Eur. J*., 2006, **12**, 2329. (f) . Teki and S. Nakajima, *Polyhedron*, 2005, **24**, 2185. (g) T. Toichi and Y. Teki, *Polyhedron*, 2005, **24**, 2337. (h) N. Mihara and Y. Teki, *Inorg. Chim. Acta*, 2008, **361**, 3891.
30. (a) Y. Teki, H. Tamekuni, J. Takeuchi and Y. Miura, *Angew. Chem., Int. Ed*., 2006, **45**, 4666. (b) Y. Teki, H. Tamekuni, K. Haruta, J. Takeuchi and Y. Miura, *J. Mater. Chem*., 2008, **18**, 381. (c) Y. Takemoto and Y. Teki, *ChemPhysChem*, 2011, **12**, 104.
31. (a) C. Corvaja, M. Maggini, M. Prato, G. Scorrano, M. Venzin, *J. Am. Chem. Soc.*, 1995, **117**, 8857. (b) J. Fujiwara, Y. Iwasaki, Y. Ohba, S. Yamauchi, N. Koga, S. Karasawa, M. Fuhs, K. Möbius, S. Weber, *Appl. Magn. Reson*., 2001, **21**, 483. (c) M. T. Colvin, E. M. Giacobbe, B. Cohen, T. Miura, A. M. Scott, M. R. Wasielewski, *J. Phys. Chem. A.*, 2010, **114**, 1741.
32. (a) K. Ishii, J. Fujiwara, Y. Ohba, S. Yamauchi, *J. Am. Chem. Soc*., 1996, **118**, 13079. (b) K. Ishii, Y. Hirose, N. Kobayashi, *J. Phys. Chem. A.*, 1999, **103**, 1986.

33. I. Ciofini, C. Adamo, Y. Teki, F. Tuyèras, P. P. Lainē, *Chem.–Eur. J*., 2008, **14**, 11385.

34. (a) Y. Teki, T. Matsumoto, *Phys. Chem. Chem. Phys*., 2011, **13**, 5728. (b) T. Matsumoto, Y. Teki, Phys. *Chem. Chem. Phys*. 2012, **14**, 10178.

35. C.-W. wan, A. Burghart, J. Chen, F. Bergström, L. B.-Å. Johansson, M. F. Wolford, T. G. kim, M. R. Topp, R. M. Hochstrasser, K. Burgess, *Chem. Eur. J*., 2003, **9**, 4430.

36. (a) Y. Kawanaka, A. Shimizu, T. shinada, R. Tanaka, Y. Teki, *Angew. Chem. Int. Ed*., 2013, **52**, 6643. (b) A. Ito, A. Shimizu, N. Kishida, Y. Kawanaka, D. Kosumi, H. Hashimoto, Y. Teki, *Angew. Chem. Int. Ed*., 2014, **53**, 6715.

37. A. Droghetti, S. Sanvito, *Phys. Rev. Lett*., 2011, **107**, 047201.

38. (a) S. Bin-Salamon, S. Brewer, S. Franzen, D. L. Feldheim, S. Lappi, D. A. Shultz, *J. Am. Chem. Soc.*, 2005, **127**, 5328. (b) D. A. Shultz, R. K. Kumar, S. Bin-Salamon, M. L. Kirk, *Polyhedron*, 2005, **24**, 2876. (c) M. M. Paquette, R. A. Kopelman, E. Beitler, N.L. Frank, *Chem. Commun*., 2009, 5424. (d) S. Kanegawa, S. Kang, O. Sato, *Chem. Lett*., 2013, **42**, 700.

39. (a) A. Loudet, K. Burgess, *Chem. Rev*., 2007, **107**, 4891. (b) G. Ulrich, R. Ziessel, A. Harriman, *Angew. Chem. Int. Ed*., 2008, **47**, 1184. (c) H. Lu, J. Mack, Y. Yang, Z. Shen, *Chem. Soc. Rev*., 2014, **43**, 4778.

40. (a) N. Boens, V. Leen, W. Dehaen, *Chem. Soc. Rev*., 2012, **41**, 1130. (b) A. Kamkaew, S. H. Lim, H. B. Lee, L. V. Kiew, L. Y. Chung, K. Burgess., *Chem. Soc. Rev.*, 2013, **42**, 77. (c) A. Bessette, G. S. Hanan, *Chem. Soc. Rev*., 2014, **43**, 3342. (d) S. P. Singh, T. Gayathri, *Eur. J. Org. Chem.*, 2014, 4689.

41. (a) P. Kos, H. Plenio, *Chem. Eur. J*. 2015, **21**, 1088. (b) A. M. Lifschitz, R. M. Young, J. Mendez-Arroyo, V. V. Roznyatovskiy, C. M. Mcguirk, M. R. Wasielewski, C. A. Mirkin, *Chem. Commun*., 2014, **50**, 6850.

42. (a) J. A. Real, M. C. Muñoz, J. Faus, X. Solans, *Inorg. Chem.*, 1997, **36**, 3008. (b) N. Moliner, L. Salmon, L. Capes, M. C. Muñoz, J.-F. Létard, A. Bousseksou, J.-P. Tuchagues, J. J. McGarvey, A. C. Dennis, M. Castro, R. Burriel, J. A. Real, *J. Phys. Chem. B*, 2002, **106**, 4276.

43. F. Neugenbauer, H. Fisher, *Angew. Chem., Int. Ed*., 1980, **19**, 724.

44. G. G. Belford, R. L. Belford and J. F. Bukhalter, *J. Magn. Reson*., 1973, **11**, 251.

45. Y. Teki, I. Fujita, T. Takui, T. Kinoshita and K. Itoh, *J. Am. Chem. Soc*., 1994, **116**, 11499.

46. H. Naggert, A. Bannwarth, S. Chemnitz, T. V. Hofe, E. Quandt, F. Tuczek, *Dalton Trans*., 2011, **40**, 6364

47. See: R. Boča, Theoretical Fundations of Moleculer Magnetism, Elsevier, 1999, ch. 9, pp. 541–578.

48. H. Matsukizono, K. Kuroiwa, N. Kimizuka, *Chem. Lett.*, 2008, **37**, 446.

49. P. T. Tourón, S. V. Mosquera, M. Lima, A. Lapini, P. Fohhi, A. Dei, R. Righini, *Phys. Chem. Chem. Phys*., 2012, **14**, 1038.

50. K. G. Alley, G. Poneti, P. S. D. Robinson, A. Nafady, B. Moubaraki, J. B. Aitken, S. C. Drew, C. Ritchie, B. F. Abrahams, R. K. Hocking, K. S. Murray, A. M. Bond, H. H. Harris, L. Sorace, C. Boskovic, *J. Am. Chem. Soc*., 2013, **135**, 8304.

51. M. D. Stallings, M. M. Morrison, D. T. Sawyer, *Inorg. Chem*., 1981, **20**, 2655.

52. (a) A. Caneschi, A. Dei, D. Gatteschi, V. Tangoulis, *Inorg. Chem*., 2002, **41**, 3508. (b) F. Yu, B. Li, *Inorg. Chim. Acta*, 2012, 199.

53. G. Poneti, M. Mannini, B. Cortigiani, L. Poggini, L. Sorance, E. Otero, P. Sainctavit, R. Sessoli, , A. Dei, *Inorg. Chem*., 2013, **52**, 11798.

54. P. Dapporto, A. Dei, G. Poneti, L. Sorace, *Chem. Eur. J*., 2008, **14**, 10915

55. (a) P. D. Bonnitcha, B. J. Kim, R. K. Hocking, J. K. Clegg, P. Turner, S. M. Neville, T. W.

Hambley, *Dalton Trans*., 2012, **41**, 11293. (b) M. Alimi, A. Allam, M. Selkti, A. Tomas, P. Roussel, E. Galardon, I. Artaud, *Inorg. Chem*., 2012, **51**, 9350.

56. H. Sunahara, Y. Urano, H. Kojima, T. Nagano, *J. Am. Chem. Soc*., 2007, **129**, 5597.
57. (a) B. Umasekhar, E. Ganapathi, T. Chatterjee, M. Ravikanth, *Dalton Trans*., 2015, **44**, 16516. (b) B. Dhokale, P. Gautam, S. M. Movin, R. Misra, *Dalton Trans*., 2013, **42**, 1512.
58. M. Kollmannsberger, T. Gareis, S. Heinl, J. Breu, J. Daub, *Angew. Chem. Int. Ed. Engl.*, 1997, **36**, 1333.
59. W. Qin, M. Baruah, M. V. D. Auweraer, F. C. D. Schryver, N. Boens, *J. Phys. Chem. A*, 2005, **109**, 7371-7384.
60. A. M. Brun, A. Harriman, Y. Tsuboi, T. Okada, N. Mataga, *J. Chem. Soc. Faraday Trans*., 1995, **91**, 4047.
61. C. A. Parker, W. T. Rees, *Analyst*, 1960, **85**, 587.
62. (a) S. Banthia, A. Samanta, *J. Phys. Chem. B*., 2006, **110**, 6437. (b) Z. Li, X. Lou, H. Yu, Z. Li, J. Qin, *Macromolecules*, 2008, **41**, 7433.
63. J. Bartelmess, W. W. Weare, R. D. Sommer, *Dalton Trans*., 2013, **42**, 14883.
64. D. P. Kennedy, C. M. Kormos, S. C. Burdette, *J. Am. Chem. Soc*., 2009, **131**, 8578.
65. (a) N. Yamamoto, S. Danos, P. D. Bonnitcha, T. W. Failes, E. J. New, T. W. Hambley, *J. Biol. Inorg. Chem*., 2008, **13**, 861. (b) N. Yamamoto, A. K. Renfrew, B. J. Kim, N. S. Bryce, T. W. Hambley, *J. Med. Chem*., 2012, **55**, 11013.
66. (a) A. P. de Silva, H. Q. N. Gunaratone, C. P. Mccoy, *Nature*, 1993, **364**, 42. (b) O. A. Bozdemir, R. Guliyev, O. Buyukcakir, S. Selcuk, S. Kolemen, G. Gulseren, T. Nalbantoglu, H. Boyaci, E. U. Akkaya, *J. Am. Chem. Soc*., 2010, **132**, 8029.
67. B. Valeur, *Molecular Fluorescence: Principles and Applications*, 3rd ed., Wiley-VCH, Weinheim: New York, 2006

68. M. C. Burla, R. Caliandro, M. Camalli, B. Carrozzini, G. L. Cascarano, L. De Caro, C. Giacovazzo, G. Polidori, R. Spagna, *J. Appl. Crystallogr*., 2005, **38**, 381.

69. G. M. Sheldrick, *Acta Crystallogr., Sect. A: Fundam. Crystallogr*., 2008, **A64**, 112.

70. M. J. Frisch, G. W. Trucks, H. B. Schlegel, G. E. Scuseria, M. A. Robb, J. R. Cheeseman, J. A. Montgomery, Jr., T. Vreven, K. N. Kudin, J. C. Burant, J. M. Millam, S. S. Iyengar, J. Tomasi, V. Barone, B. Mennucci, M. Cossi, G. Scalmani, N. Rega, G. A. Petersson, H. Nakatsuji, M. Hada, M. Ehara, K. Toyota, R. Fukuda, J. Hasegawa, M. Ishida, T. Nakajima, Y. Honda, O. Kitao, H. Nakai, M. Klene, X. Li, J. E. Knox, H. P. Hratchian, J. B. Cross, V. Bakken, C. Adamo, J. Jaramillo, R. Gomperts, R. E. Stratmann, O. Yazyev, A. J. Austin, R. Cammi, C. Pomelli, J. W. Ochterski, P. Y. Ayala, K. Morokuma, G. A. Voth, P. Salvador, J. J. Dannenberg, V. G. Zakrzewski, S. Dapprich, A. D. Daniels, M. C. Strain, O. Farkas, D. K. Malick, A. D. Rabuck, K. Raghavachari, J. B. Foresman, J. V. Ortiz, Q. Cui, A. G. Baboul, S. Clifford, J. Cioslowski, B. B. Stefanov, G. Liu, A. Liashenko, P. Piskorz, I. Komaromi, R. L. Martin, D. J. Fox, T. Keith, M. A. Al-Laham, C. Y. Peng, A. Nanayakkara, M. Challacombe, P. M. W. Gill, B. Johnson, W. Chen, M. W. Wong, C. Gonzalez, J. A. Pople, *Gaussian 03, Revision E.01*, Gaussian, Inc., Wallingford CT, 2004.

71. (a) C. L. Barr, P. A. Chase, R. G. Hicks, M. T. Lemaire, S.-B. Stevens, *J. Org. Chem*., 1999, **64**, 8893. (b) Y.-Q. Fang, G. S. Hanan, *Synlett*., 2003, 852. (c) D. W. Lin, T. Masuda, M. B. Biskup, J. D. Nelson, P. S. Baran, *J. Org. Chem*. 2011, **76**, 1013.

Acknowledgements

本研究を進めるにあたり、生体分子設計学研究室およびその前身である分子設計学研究室に在籍した 6 年間、私は多くの方々に支えられてきました。6 年間最もお世話になり、副査を務めていただいた廣津昌和准教授、アメリカ留学の機会をいただいた木下勇名誉教授、主査をお引き受けいただいた量子機能物質学研究室の手木芳男教授、副査をお引き受けいただき、研究に対しても様々なアドバイスをいただいた中島洋教授、研究を含め様々なことで、ためになるお話をいただき、さらに阪神タイガースの良さを伝えていただいた西岡孝訓准教授には、大変お世話になりましたこと深く感謝いたします。また実験やデータの解釈の議論にお付き合いいただいた量子機能物質学研究室の伊藤亮孝博士、アメリカでの２か月間お世話になった Lawrence R. Sita 教授に深く感謝いたします。ならびに、物質分子系専攻および旧物質科学科の先生方にお世話になり、本当にありがとうございました。

研究生活において、先輩である桑村直人さん、柴田鉄平さん、杉村欣則さん、壷井千秋さん、加藤学さん、竹口勝也さん、山東磨司さん、池中俊哉さん、中藤彩美さん、清水優さん、川本圭祐さんに様々な指導をいただき、大変お世話になりました。同期である、植田真菜さん、増田裕さん、前田友梨さん、竹本祐唯さん、他研究室の物質科学科同期たち、特に前田健太郎さんとは楽しい学生生活を送らせていただき感謝しています。指導が至らぬ点もあったと思いますが、後輩である小林恭平さん、今仲庸介さん、吉野誠人さん、武田臣祐さん、中江豊崇さん、西紀透さん、中尾圭太さん、長谷川智之さん、小田祥也さん、松永拓海さん、塩本直俊さん、内田勇太さん、久島健人さん、田中優衣さん、村田千智さん、文珠良侑さん、佐納惇平さん、濵村菜摘さん、久保田真史さん、南健太郎さん、驚きのある研究生活を送れて感謝しています。

留学生活では、Kaitlyn E. Crawford さん、Wonseok Hwang さん、Andrew Keane さん、Wesley Farrell さん、Gail Blakley さんに大変お世話になり、本当に感謝しています。

後期博士課程における三年間は、日本化学工業協会の人材育成プログラムからの支援をいただき、深く感謝しています。

最後に博士課程進学の私を温かく見守っていただいた両親に、深く感謝の意を表して謝辞といたします。

大阪市立大学　理学研究科

片山晃一

2015 年 3 月

List of Achievements

Articles

1. K. Katayama, M. Hirotsu, I. Kinoshita, Y. Teki, *Dalton Trans*., **2012**, *41*, 13465.
2. K. Katayama, M. Hirotsu, I. Kinoshita, Y. Teki, *Dalton Trans*., **2014**, *43*, 13384.

Oral Presentation

1. K. Katayama, M. Hirotsu, I. Kinoshita, H. Nakajima, Y. Teki 「Luminescence behavior and magnetic properties of cobalt complexes with a dioxolene ligand containing an anthracene-BODIPY unit」Annual Meeting on Photochemistry 2015, 2D01, September, 2015 (Osaka)
2. 片山晃一・廣津昌和・木下勇・手木芳男「発光部位を有するカテコール誘導体を用いたコバルト錯体の合成と性質」錯体化学会第64回討論会、1B-06、2014年9月、東京
3. 片山晃一・廣津昌和・木下勇・手木芳男「π共役安定有機ラジカルを配位子とする錯体の合成と磁気的性質」第51回電子スピンサイエンス学会、3B-05、2012年11月、北海道

Poster Presentation

1. K. Katayama, M. Hirotsu, I. Kinoshita, Y. Teki「Synthesis and valence tautomerism of cobalt complexes with a dioxolene ligand containing a π-conjugated system」Pacifichem 2015, December, 2015 (Hawaii)
2. K. Katayama, M. Hirotsu, I. Kinoshita, H. Nakajima, Y. Teki「Synthesis and fluorescence behavior of cobalt complexes with a dioxolene ligand linked to an anthracene-BODIPY

moiety」 The 19th Osaka City University International Symposium, P-20, November (2015).

3. 片山晃一・廣津昌和・木下勇・中島洋・手木芳男「機能性部位連結ジオキソレン配位子を有するコバルト錯体の合成と性質」第5回CSJ化学フェスタ2015、P2-071、2015年10月、東京
4. 片山晃一・廣津昌和・木下勇・中島洋・手木芳男「BODIPY-アントラセンを連結したジオキソレンコバルト錯体の合成と発光挙動」錯体化学会第65回討論会、2PB-19、2015年9月、奈良
5. K. Katayama, M. Hirotsu, I. Kinoshita, Y. Teki「Magnetic properties of Co Complexes with Anthracene Moiety」5th International Meeting on Spin in Organic Semiconductor 2014, PB-17, October, 2014 (Hyogo)
6. 片山晃一・廣津昌和・木下勇・手木芳男「アントラセン連結カテコール配位子を有するコバルト錯体の合成と性質」錯体化学会第63回討論会、1PB-011、2013年11月、沖縄
7. 片山晃一・廣津昌和・木下勇・手木芳男「π共役安定有機ラジカルを配位子とするコバルト錯体の合成と磁気的性質」第 6 回分子科学討論会、3P-038、2012 年 9 月、東京
8. 片山晃一・廣津昌和・木下勇・手木芳男「π共役安定有機ラジカルを配位子に用いた錯体の合成と電子状態」錯体化学会第61回討論会、1PB-016、2011年9月、岡山